2008-12-22

On the Variability of the Wind Stress at the Air-Sea Interface

Fei Zhang
University of Miami, fzhang@rsmas.miami.edu

UNIVERSITY OF MIAMI

ON THE VARIABILITY OF THE WIND STRESS AT THE AIR-SEA INTERFACE

By

Fei Zhang

A DISSERTATION

Submitted to the Faculty
of the University of Miami
in partial fulfillment of the requirements for
the degree of Doctor of Philosophy

Coral Gables, Florida

December 2008

UNIVERSITY OF MIAMI

A dissertation submitted in partial fulfillment of
the requirements for the degree of
Doctor of Philosophy

ON THE VARIABILITY OF THE WIND STRESS AT THE AIR-SEA INTERFACE

Fei Zhang

Approved:

_____	_____
William M. Drennan, Ph.D. Associate Professor of Applied Marine Physics	Terri A. Scandura, Ph.D. Dean of Graduate School
_____	_____
Hans C. Graber, Ph.D. Professor of Applied Marine Physics	Brian K. Haus, Ph.D. Associate Professor of Applied Marine Physics
_____	_____
Peter J. Minnett**,** Ph.D. Professor of Meteorology and Physical Oceanography	Kimmo K. Kahma, Ph.D. Research Professor Finnish Institute for Marine Research

ZHANG, FEI (Ph.D. Applied Marine Physics)
On the Variability of the (December 2008)
Wind Stress at the Air-Sea Interface

Abstract of a dissertation at the University of Miami.

Dissertation supervised by Professor William M. Drennan
No. of pages in text. (130)

This dissertation investigates wind-wave-current interaction, wave breaking detection and the analysis of breaking characteristics at the air-sea interface. In-situ data measured during the Shoaling Waves Experiment (SHOWEX) and Baltic Sea Swell Experiment (BASE) are applied in the studies and analysis. Wind, wind stress and wave data were obtained from several Air Sea Interaction Spar (ASIS) buoys. Surface currents were measured by a High-Frequency Ocean Surface Current Radar.

Two distinct types of wave-current-wind interaction were observed in the presence of a strong along-coast current. First, the horizontal current shear resulted in wind-sea waves shifting away from the wind direction. This motion resulted in a steering of the stress away from the mean wind direction. Second, short wind waves on a uniform current are shifted to the current direction, and the wind stress is steered toward the current direction by the short waves. The wind stress veering has been confirmed by data from the SeaWind scatterometer on board the QuikSCAT satellite. This finding is in agreement with the results from some recent studies.

The present study also describes an experimental investigation of breaking wave detection by ASIS buoys. A method, developed from the laboratory, and using local wave parameters to provide a detailed description of breaking, is applied to wave data from ASIS buoys. One the basis of these data, the relation between breaking probability and wind speed shows characteristics similar to those from several field experiments with different conditions. Furthermore, additional parameters, wave age and wave steepness, are also shown to affect the breaking probability during our in-situ measurements. Upper ocean shear, which can modulate wave breaking as predicted by both theory and laboratory work, are also observed to change the breaking properties. This characteristic is rarely reported by in-situ experiment.

Table of Contents

Chapter 1

Introduction

Atmosphere-ocean interaction has an important influence on global weather and climate, since the ocean absorbs more solar radiation than land does. With the influence of earth's rotation, zonal differences in heating drive global atmospheric circulation, which in return has significant effects on the oceanic system. The interface between the atmosphere and ocean becomes an active place for momentum and energy exchange. As part of a coupled system exchanging momentum and energy, waves and currents in the ocean inevitably influence the marine atmospheric boundary layer (MABL), so the MABL has different characteristics from the atmosphere boundary layer over the land.

Winds near the sea surface are highly variable in space and time, and this intermittency and associated air-sea fluxes are not well studied. The air-sea exchange of momentum (wind stress) is neither fully understood nor well parameterized. We are not only concerned with how wind energy is transferred into waves and currents, but also how the ocean waves and currents feed back to the atmosphere. Idealized simulations have indicated that the ocean wave feed-back has an important input on mesoscale or even larger scale atmospheric circulations (Chen et al., 2008). Moreover, laboratory and field observations have shown that dominant wave breaking and currents could be second-order effects on the wind stress at air-sea interface (Banner et al., 2000; Babanin et al.,

2001). Because of the complexity in air-sea interactions in the ocean and the potential changes due to coastal currents, propagating swell and dominant wave breaking, the associated mixing and transport properties should be considered in the context of the current-wave-wind interactions.

Current-wave and wind-wave interactions have been popular topics for several decades (Phillips, 1957; Miles, 1957; Huang et al., 1972; Kitaigorodskii et al., 1975). Detailed investigations have illuminated some of the mechanisms by which currents, waves and winds exchange momentum and energy. However, the lack of simultaneous direct measurements of currents, waves, wind and wind stress has limited progress on the study of current-wave-wind interaction. Until now, no comprehensive investigations of this problem have been made. With the recent efforts to couple ocean, wave and atmosphere models (Moon et al. 2007; Chen et al. 2008), accurate knowledge of these interactions is increasingly important.

In order to improve the understanding of the complex situation, we need to measure the air-sea momentum flux along with wind, waves and surface currents. The Air Sea Interaction Spar buoy (ASIS) is a new-generation buoy platform (Graber et al., 2000) designed for air-sea interaction studies. It can measure accurate air-sea fluxes coincident with high-resolution directional wave information. High quality data from ASIS buoys have been collected during more than 12 field experiments [e.g. The “flux, etat de la mer, et télédétection en conditions de fetch variable” (FETCH) experiment, 1998, Drennan et al, (2003); Adverse Weather Experiment (AWE), 2000, Drennan and Shay (2006) and Deep Ocean Gas Transfer Experiment (DOGEE), 2006]. During several experiments, one or more ASIS buoys were deployed in the domain of the University of Miami’s

Ocean Surface Current Radar (OSCR) (Shay et al., 2002). With the analysis of the data from ASIS buoys and OSCR radar, we have the opportunity to investigate the fully coupled interaction between current, wave and wind. In particular, we will focus on the following topics:

Air-Sea Exchange Processes

- Investigating the feedback of wave-induced stress to the atmospheric boundary layer
- Studying the effects of current on the wind stress vectors through surface waves.

Wave-Breaking

- Quantifying the breaking of dominant waves in the field
- Determining the roles of wind forcing, surface current and upper ocean shear on wave breaking.

Remote Sensing

- Studying co-located satellite data (QuikSCAT) and in-situ measurements to determine the possible surface current feedback on mesoscale or even larger scale atmospheric circulation.

The above studies will not answer all the questions remaining in current-wave-wind interaction, but they will contribute to a greater understanding of the complex problem and increase the accuracy of modeling the wind stress and wind waves under the effect of ocean currents. In addition, the research on the effect of ocean currents on wind retrieved from radar backscatter may lead to a method of removing the ocean current from satellite

wind fields. In this dissertation, the principles, theories and definitions related to the research will be reviewed in Chapter 2. Several field experiments used in this dissertation will be introduced in Chapter 3. The studies about current-wave-wind interaction are presented in Chapter 4. The detection and analysis of dominant wave breaking and the effects of upper ocean shear on it are shown in Chapter 5. Chapter 6 gives the conclusions about the whole dissertation.

Chapter 2

Background

While the boundary between the ocean and the atmosphere has been extensively studied it is still not well understood. Heat, mass and momentum cross this boundary at a rate determined by many features related not only the sea surface motion but also the properties of the atmospheric and the oceanic boundary layers on each side of the interface. Central to understanding the processes at the boundary is gaining knowledge about the flux of momentum across the air-sea surface. The flux is mostly from the atmosphere to the ocean currents through drag, but less frequently, the flux is from the wind-waves or currents back to the atmosphere.

If we treat the sea surface as a sharp boundary between two fluids of different properties, we can model the flux of momentum from one of the fluids to the other as a drag force per unit area at the sea surface. This is the surface shear stress. My studies in this dissertation focus on the wind stress in the air side. Early in the twentieth century aerodynamicists successfully related the wind stress over a solid surface to its physical roughness (Richardson, 1920), and meteorologists have, with less success, used these concepts to calculate atmospheric drag over land. When interest changes to air flow over the sea surface, much lower drags are observed than expected from the physical

roughness. Why does the sea surface look so rough but support little drag? While this question still remains to be fully answered, it soon becomes obvious that the drag coefficient of the sea is not only dependent on wind speed, but also the sea state. Surface waves play an important role when we investigate the wind stress at air sea interface. In this chapter, I will review previous theories and studies about wind stress, ocean wave effects on the wind stress, current-wave interaction studies etc. This background information will guide me toward the study of current-wave-wind interaction and dominant wave breaking.

2.1 Wind Stress over the Ocean

2.1.1 Monin-Obukov Similarity Theory

The horizontal force of the wind on the surface (land or sea) is called the wind stress. Considered in another way, it is the vertical transfer of horizontal momentum by wind shear. Thus momentum is transported between the atmosphere and the sea surface. The traditional theoretical and experimental approach to estimating air-sea fluxes has utilized of the framework of Monin-Obukhov (M-O) similarity theory (Monin and Obukhov, 1954). In this theory, the friction velocity u_* is introduced as a turbulent velocity scale. In the absence of buoyancy, and with the assumption of eddy viscosity increasing linearly with height z and friction velocity, this leads to the well known logarithmic velocity profiles of a shear layer. u_* is calculated in terms of the downstream momentum flux

$-\overline{u'w'}$ and crosswind momentum flux $-\overline{v'w'}$, where u', v' and w' are downwind, crosswind and vertical fluctuating wind velocities respectively. The bar is a time averaging operator.

$$u_* = \{(-\overline{u'w'})^2 + (-\overline{v'w'})^2\}^{1/4} = \sqrt{\left|\frac{\vec{\tau}}{\rho}\right|} \tag{2.1}$$

where $\vec{\tau} = \rho\{(-\overline{u'w'})\vec{i} + (-\overline{v'w'})\vec{j}\}$ is the wind stress and ρ is the air density. Here $\vec{i}$ and $\vec{j}$ represent unit vectors along and perpendicular to the mean wind respectively. The fluctuating velocity components u', v' and w' are decomposed from instantaneous velocities by the Reynolds decomposition method: $u = \overline{U} + u'$; $v = \overline{V} + v'$; $w = \overline{W} + w'$. Here u, v, w are the instantaneous velocities of the downwind, crosswind and vertical components and $\overline{U}, \overline{V}, \overline{W}$ are their mean parts. By definition $\overline{u}' = \overline{v}' = \overline{w}' = 0$.

If M-O similarity theory is valid, then $-\overline{v'w'}$ is negligible, and the stress is in the mean wind direction: $u_*^2 = -\overline{u'w'}$. More generally, buoyancy is an additional source (or sink) of turbulence. An important consequence of M-O similarity theory is that buoyancy can be brought into the problem through the addition of a single length scale L

$$L = -\frac{u_*^3 T_0}{\kappa g \overline{w'\theta_v}'} \tag{2.2}$$

where $\kappa \approx 0.4$ is the dimensionless von Kármán constant; g=9.8 m/s^2 is the acceleration of gravity; T_0 is the reference absolute temperature; $\overline{w'\theta_v}'$ is the kinetic heat flux (θ_v' is turbulent component of virtual temperature).

The Obukhov length L is the height where the mechanical and the buoyant forcing are equal.Using $dU/dz = u_* / \kappa z$ (Monin and Obukhov, 1954), we can define the stability parameter or flux Richardson number ζ :

$$\zeta = \frac{z}{L} = \frac{-g\alpha\overline{w'\theta_v'}}{-\overline{u'w'}(\frac{dU}{dz})} = \frac{buoyant \quad destruction(production)}{shear \quad production} \tag{2.3}$$

where $\alpha = \frac{1}{T_0}$. As $\zeta \to 0$ there is no buoyant forcing; this is called the neutral condition.When $\zeta < 0$, the environment is unstable. When $\zeta << -1$, turbulence is generated mainly by buoyancy and shear production is negligible. $\zeta > 0$ means a stable environment; for $\zeta >> 1$, buoyant destruction removes turbulence at a rate larger than the turbulence is produced by shear.

We define normalized flux-gradients ϕ_u and ϕ_θ as:

$$\phi_u(z/L) = (\kappa z / u_*)(\partial U / \partial z) \tag{2.4}$$

$$\phi_\theta(z/L) = (\kappa z / T_*)(\partial \Theta / \partial z) \tag{2.5}$$

where $T_* = -\overline{w'\theta_v'}/u_*$ is a turbulent temperature scale and Θ is the mean value of potential temperature. By assuming the momentum flux and heat flux to be constant in surface layer, the mean quantities at height z are obtained by integrating (2.4) and (2.5) from z_0 and z_{oT} :

$$U(z) - U(0) = \frac{u_*}{\kappa}\ln\left((\frac{z}{z_o}) - \Psi_u\left(\frac{z}{L}\right)\right) \tag{2.6}$$

$$\Theta(z) - \Theta(0) = \frac{T_*}{\kappa}\ln\left((\frac{z}{z_{0T}}) - \Psi_\theta\left(\frac{z}{L}\right)\right) \tag{2.7}$$

where z_0 is the roughness length for momentum flux and z_{oT} is the roughness length for sensible heat flux. $U(z)$ and $\Theta(z)$ are the horizontal wind speed and potential temperature at height z above the surface. Ψ_u and Ψ_θ are the integrated forms of ϕ_u and ϕ_θ:

$$\Psi(\zeta) = \int_{z_o/L}^{z/L} [1-\phi(\zeta)]/\zeta d\zeta \quad . \tag{2.8}$$

The most common expressions of the ϕ-functions in the interval of $-2 < z/L < 1$ are empirical equations based on measurements over land. In case of stable stratification (*L>0*), linear functions are both theoretically derived and experimentally supported (Monin and Yaglom, 1971):

$$\phi_u = 1 + B_1\zeta \tag{2.9}$$

B_1 varies, according to observations, from 4.7 to 5.2; $B_1 = 5$ is assumed in this dissertation. For regions with moderately unstable stratification, the Businger-Dyer formulation is widely used (Businger et al. 1971; Dyer 1974):

$$\phi_u = (1 - C_1\zeta)^{-1/4} \tag{2.10}$$

where the values of C_1 ranging from 16 to 28 fit the data derived from the measurements over oceans (Edson et al. 1998); $C_1 = 22$ is used in this study.

Several decades of research using this procedure has provided parameterizations of the dimensional shear that vary only slightly from one another (e.g. Dyer and Hicks 1970; Wyngaard and Coté 1971; Kaimal et al. 1972; Champagne et al. 1977; Dyer and Bradley 1982; Frenzen and Vogel 1992; Oncley et al. 1996). As a result, the MO similarity hypothesis has provided nearly universal functions from these experiments and it is

widely accepted by the atmospheric community. These semi-empirical relationships are often used to estimate the desired turbulent quantities from mean measurements over the ocean where direct measurement of the fluxes is very difficult as described in section 2.1.3. However, the use of overland measurements to infer surface fluxes over the ocean is questionable, particularly close to the ocean surface. Therefore, the universality of these relationships to all surface layers is a current topic of intense debate.

2.1.2 Parameterization of the Wind Stress

Parameterization of the wind stress over the ocean is an important issue in the numerical analysis of atmosphere-ocean interactions for modeling, since winds blowing at the surface constitute a very important driving force for ocean currents and waves. Wind is routinely observed at many coastal locations around the world, but these are little help in deducing them over the open ocean. Historically, observations from ships and buoys constitute a major portion of our knowledge of winds over the oceans, but since winds vary over a variety of time scales including hourly to annual, it is difficult to obtain complete wind information at all temporal and spatial scales over the oceans. As satellite technology develops, microwave scatterometers and radar altimeters, which infer the wind stress by sea surface roughness, are becoming an important source of wind data. Such sensors will benefit from our increased understanding of wind stress over the ocean, especially considering the wave effect on wind stress.

Over the ocean, we can consider wind stress in the boundary layer as

$$\vec{\tau} = \vec{\tau}_w + \vec{\tau}_v + \vec{\tau}_t \tag{2.11}$$

which are wave-induced stress, viscous stress and turbulent stress respectively on the right side. Janssen (1989) showed the distribution of turbulent stress and wave-induced stress as a function of height above air-sea interface (Figure 2.1). Wave-induced stress is a stress caused by direct input of momentum flux due to the presence of waves (Janssen, 1989). The viscous stress is only significant very near the surface, where the viscous layer has a height of O (1mm) (Donelan, 1990). Above that, turbulent stress is from wind shear and buoyancy. Generally, $\tau \approx \vec{\tau}_t$ at 10-m height for the measurements both on land, and over the sea.

Figure 2.1 shows in low wave age conditions ($C_P / u_* = 5$ and for $gz / u_*^2 < 0.1$), the wave-induced stress by long waves is about 95% of total stress whereas the turbulent stress (which goes to short waves) is only 5%. The layer near the surface where the wave-induced component is significant is called the "Wave Boundary Layer" (WBL). For $C_P / u_* = 5$, the height of the WBL is predicted by Janssen's model to be order $u_*^2 / g \approx 1cm$. In contrast, wave field development is undeveloped ($C_P / u_* = 23$), the WBL is predicted to be smaller and O (1mm).

Drennan et al. (1999) showed the WBL had a depth with O(1m) under wind sea wave conditions, but Smedman et al. (1999) showed the WBL can extent to 30m height under swell conditions. Since the total stress is constant in the surface layer, if the wave-induced stress becomes dominant at some level, the turbulent stress is consequently reduced, resulting in a modification of mean wind profiles (Stewart, 1961). As a result,

M-O similarity theory cannot be applied to the WBL. Until now, the understanding of wave-induced stress and WBL are limited because of the difficulty of conducting near-surface measurements over strong waves.

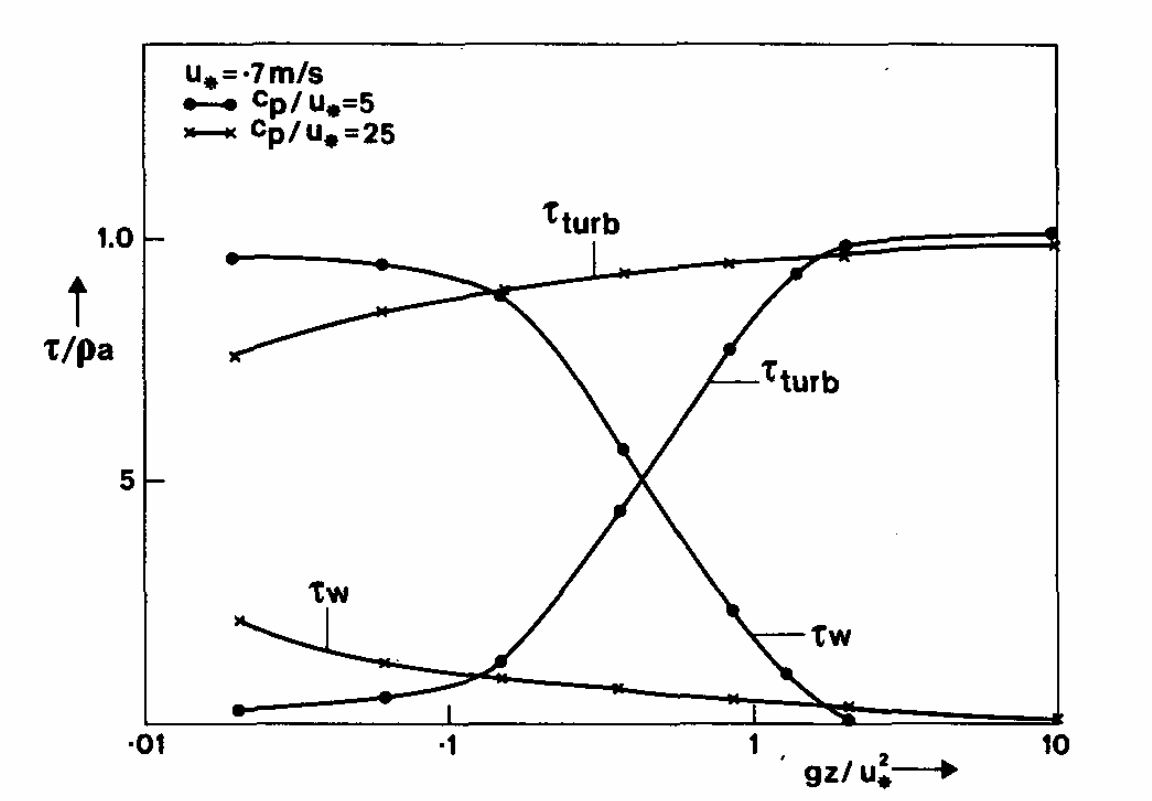

Figure 2.1: Distribution of turbulent stress and wave induced stress as a function of height, the contribution of viscous stress is not shown because it is less than 5%. C_p is phase speed at wave peak frequency; u_* is the friction velocity; C_p / u_* is wave age. $\tau_{turb} = \tau_t$ in equation 2.11. τ_w is wave-induced stress.

2.1.3 Measuring Wind Stress

In order to measure wind stress at the air-sea interface, there are two types of methods: direct and indirect.

Direct method:

The direct method of measuring momentum flux in Equation 2.1 is called the eddy correlation method. This method requires sampling of fluctuations of relevant parameters (u' and v') over a wide range of scales, and correlating them with the concurrent and co-located turbulent components of vertical velocity w'. Sampling of the turbulent signals must be fast enough and long enough in order to capture all scales contributing to the flux. However, this is a difficult task due to mesoscale (non-turbulence) effect at low frequency and inadequate sensor response at high frequency; consequently the typical sampling frequency and length is order 10Hz and 20min for typical measurement heights and wind speeds. This is sufficient for normal atmosphere conditions (Donelan 1990). The data in this dissertation are sampled at 20Hz for 30min.

Although common over land, the eddy correlation method over the sea has been limited by the availability of suitable platforms. Fixed flux platforms or towers have the obvious disadvantage that fixed structures are scarce in the ocean and generally located in shallow-water. Furthermore, they face the difficulty of causing flow distortion around sensors. The data of this dissertation are collected from a mobile buoy. The obvious problem that arises when measuring the flux from mobile platforms is that part of the measured velocity is due to platform motion. The motion contaminants have three sources according to Edson et al. (1998): (1) Instantaneous tilt from anemometer due to pitch, roll and heading variations of the platform; (2) Angular velocities at the anemometer due to the rotation of the platform about its local coordinate system axes; (3) Translational velocities of the platform with respect of a fixed-frame reference. With the development, a motion package has been developed for use in buoys (Anctil et al., 1994),

the problems associated with platform motion have essentially been solved. This will be discussed in Chapter 3.

Indirect methods:

Indirect methods include the inertial dissipation method, the profile method, and the bulk method. The inertial dissipation method (Pond et al. 1971) was derived from turbulent kinetic energy (TKE) budget, which describes the physical processes that generate turbulence:

$$\frac{\partial \overline{e}}{\partial t} + U.\nabla \overline{e} = u_*{}^2 \frac{\partial U}{\partial z} - \frac{g}{T_0}\overline{w'\theta_v'} + \frac{\partial \overline{w'e'}}{\partial z} + \frac{1}{\rho}\frac{\partial \overline{p'w'}}{\partial z} + \varepsilon \ . \tag{2.12}$$

(1) (2) (3) (4) (5) (6) (7)

where $e = 0.5(u'^2 + w'^2 + v'^2)$ (2.13)

is turbulent kinetic energy

(1) corresponds to local storage of TKE; (2) is the advection of TKE by the mean wind; (3) is the shear production of TKE from the mean wind; (4) is buoyant production or loss; (5) is vertical turbulent transport; (6) is pressure transport; (7) is molecular dissipation of TKE.

Assuming local storage and advection to be negligible, and dividing (2.12) by $u_*{}^3 / \kappa z$ we arrive at

$$\phi_u - \zeta - \phi_t - \phi_p = \frac{\kappa z}{u_*{}^3}\varepsilon \tag{2.14}$$

where $\phi_t = \frac{\kappa z}{u_*^3}\frac{\partial \overline{w'e'}}{\partial z}$ and $\phi_p = \frac{\kappa z}{\rho u_*^3}\frac{\partial \overline{w'p'}}{\partial z}$. According to M-O theory ϕ_u, ϕ_t and ϕ_p are expected to be universal functions of ζ . Then from a known dissipation rate and dimensionless functions (Högström , 1996), the stress can be readily determined. In practice, ε is usually estimated from the inertial subrange of the frequency spectrum, assuming Taylor's hypothesis:

$$\varepsilon = (\overline{f^{5/3} S(f)}/\alpha_k)^{3/2}(2\pi/U) \tag{2.15}$$

where *S(f)* is the wind velocity spectrum, and the mean is taken over the frequencies in the inertial subrange, where $S(f) \propto f^{-5/3}$ and $f >\sim 2Hz$. $\alpha_k \approx 0.52$ is the *Kolmogorov* constant (Sreenivasan 1995) . Then

$$u_* = [\kappa z \varepsilon /(\phi_u(\zeta) - \zeta - \phi_t - \phi_p))]^{1/3}. \tag{2.16}$$

ϕ_t and ϕ_p will usually assumed to cancel each other (Dupius et al 1997). Since the inertial subrange belongs to the high frequency part in the spectrum, it is not affected by either turbulent flux distortion or platform motion. Hence the method remains popular for flux measurement for vessels. However, the inertial dissipation method has been questioned by the production or destruction terms in the TKE being changed in strong swell condition (Janssen 1999; Drennan et al.,1999 and Smedman et al., 1999).

The profile method uses the dimensionless gradient functions (2.4). When we measure the mean wind speed at two different heights Z_1 and Z_2

$$\frac{U_{z1} - U_{z2}}{u_*} = \frac{1}{\kappa}[\ln\frac{Z_1}{Z_2} - \Psi(\frac{Z_1}{L}) + \Psi(\frac{Z_2}{L})]. \tag{2.17}$$

From (2.17) we obtain the friction velocity. The method is rarely employed over the sea, as profile measurements from vessels are particularly prone to mean flow distortion errors, since the flow distortion is itself a function of height (e.g. Wieringa 1980; Wyngaard 1981). However, Powell et al. (2003) utilized the dimensionless functions (2.4), along with measured profiles from dropsondes to calculate the friction velocity in hurricane conditions.

The bulk method uses an empirical coefficient to estimate the momentum flux from a measured mean wind speed. The relation is:

$$u_*^2 = C_D \left| U - U_0 \right| (U - U_0) \tag{2.18}$$

U_0 here is the same as the U(0) in Equation 2.6 which is the wind speed at the sea surface and equal to surface current speed. U_0 will be used in the following. C_D can be determined from (2.6) with help of measurement. Combining 2.6 and 2.18 leads to

$$C_D = f(z, z_0, \Psi_u) = [\kappa / (\ln(z / z_0) - \Psi_u)]^2 \ . \tag{2.19}$$

C_D is usually corrected to be a reference height of 10 m and to neutral stability so equation (2.19) becomes:

$$C_{DN} = [\kappa / \ln(z / z_0)]^2 \ . \tag{2.20}$$

In most applications, C_{DN} is used which refers to the drag coefficient under neutral condition. The bulk method can estimate the momentum flux based on the mean wind speed, so it can be used widely when dense spatial information is required. Bulk relation for wind stress by such as that of Large and Pond (1981):

$10^3 C_{DN} = 1.2, \qquad 4 \le U_{10} < 11 m/s$

$10^3 C_{DN} = 0.49 + 0.65 U_{10} \qquad 11 \le U_{10} < 25 m/s$

are still used in atmospheric or climate modeling.

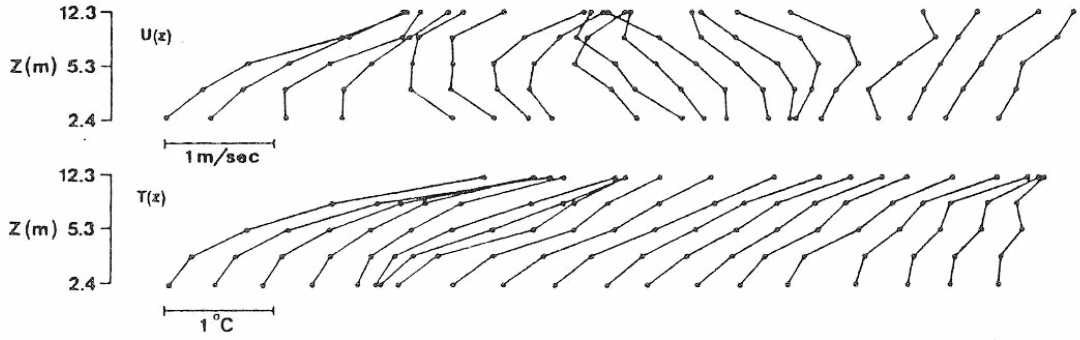

Figure 2.2:Wind speed profile (Upper panel) and air temperature profile (Lower panel) under the effect of swell.(Donelan 1990)

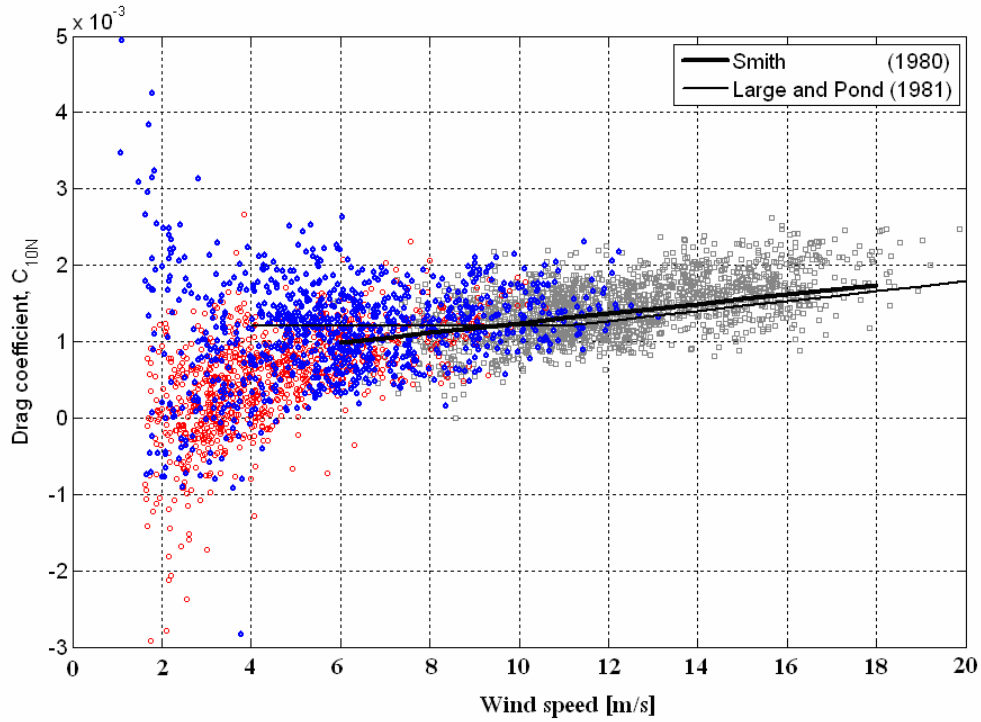

Figure 2.3: 10 m drag coefficients versus wind speed, showing the effect of swell. Data are: pure wind sea (gray) , following swell (red circle) and counter swell (blue dot) from Air-Sea Interaction Spar Buoys in the Shoaling Wave Experiment. The counter swell data show significantly enhanced drag; the following swell data significantly reduced drag or even upward momentum transfer. The thick and thin lines are the bulk relation from Smith (1980) and Large and Pond (1981).

All three methods have their own advantages for estimating the momentum flux. However, the indirect methods must rely on additional parameterizations to account for the interaction between the wave field and surface flux. These parameterizations are still

poorly understood and vary in different zones. In addition, the profile and inertial dissipation methods are based on M-O similarity theory, which has been brought into question by observations that the swell can change the wind profile in the surface layer (see e.g. Figure 2.2). The bulk relation (C_D Vs. U_Z) under swell conditions present more scatter than the situation where wind sea waves are dominant (Figure 2.3). So the direct measurements are needed if we want to improve these indirect methods. The data in this dissertation is from a sonic anemometer using the eddy correlation method.

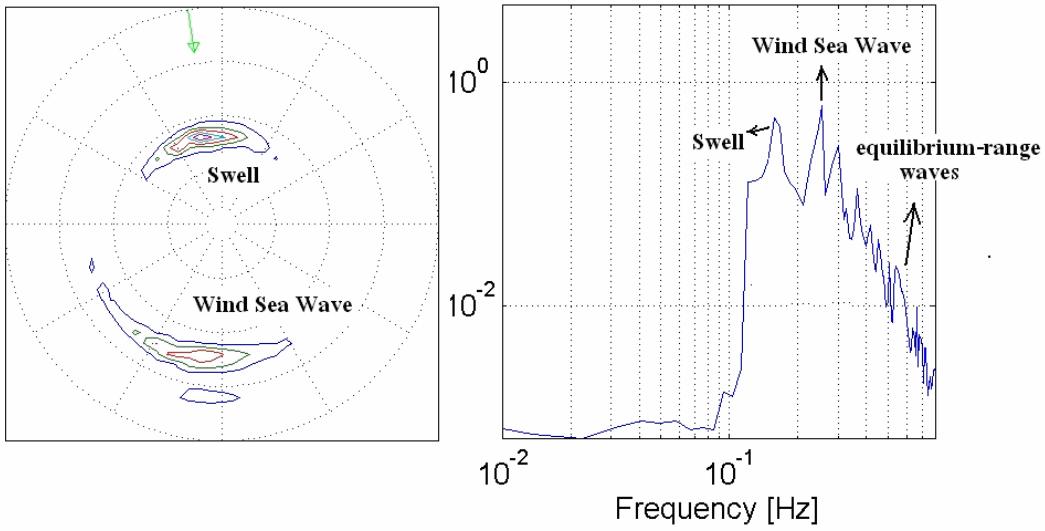

Figure 2.4: The left-side panel is a sample 2D wave spectrum, with north and east at top and right, respectively. The contours represent energy, and the four circles represent frequencies 0.1, 0.2, 0.3 and 0.4 Hz. The wind, 8 m/s, from -9 deg direction is shown by the arrow. The wave field is decomposed to two wave trains. The waves following the wind are wind sea waves with $f_p = 0.25hz$ and $c_p = 5.98m/s$. The waves propagating against the wind are swell, with $H_s = 0.61m$, $f_p = 0.18hz$ and $c_p = 9.67m/s$ The right-side panel is the 1D wave spectrum.

2.2 Sea State Effects on Wind Stress

2.2.1 Surface Wave Effect on Wind stress

Surface waves are the waves that occur at the interface between the atmosphere and ocean. They usually result from wind or geological effects and may travel thousands of kilometer before striking land. They range in size from capillary waves to huge tsunamis. There is little actual forward motion of individual water particles in a wave, despite the large amount of energy and momentum it may carry forward. We focus on wind-driven waves here.

To study the surface waves in the ocean, we need know the properties of waves at different frequency bands. A unidirectional wave frequency spectrum is the distribution of wave energy as a function of frequency (right panel in Figure 2.4); a directional wave spectrum is the distribution of wave energy as a function of frequency and direction (left panel in Figure 2.4). It describes the total energy of a wave-field at a given time. The waves at the frequencies around the peak are the energy-containing waves. They may be wind sea wave or swell waves. Waves that have been generated by wind in the ocean and are still under the influence of wind are known as wind sea waves. The waves extract energy from the atmosphere. The waves leaving the generating area and no longer under the influence of the generating wind are called swell waves. Figure 2.4 shows one case of coexisting swell and wind sea waves. Swells can propagate thousands of kilometers, carrying considerable energy. Swell is also one of the fundamental phenomena present at the air-sea interface. The part of wind wave spectrum, with the wave number or frequency between two and five times the values at the peak of the spectrum, collapse

onto a universal curve when the spectrum is properly scaled. The collapse was attributed to dynamic balance and so such part of the spectrum was referred to equilibrium range by Kitaigorodskii (1983) and Phillips (1985).

In order to study the effect of waves on the wind stress, we can isolate the wave-induced stress from the total wind stress as in 2.11. For the wind stress just above the viscous layer, the total wind stress is equal to the wave-induced stress $\vec{\tau}_w$. Wave-induced stress is supported by the surface waves as described by Plant et al. (1999)

$$\vec{\tau}_w = \rho_w \int \beta(\vec{k}) c(\vec{k}) \vec{k} F(\vec{k}) d\vec{k} \qquad (2.21)$$

ρ_w is density of sea water, $\beta(\vec{k})$ is the rate of transfer of momentum to or from a wave of wavenumber $\vec{k}$, $c(\vec{k})$ is the phase speed of that wave, and $F(\vec{k})$ is spectral density of the surface waves. $\vec{k}$ relates to wave frequency f by the dispersion relation ($\left|\vec{k}\right| = (2\pi f)^2 / g$ for deep water)

$\vec{\tau}_w$ is the stress corresponding to all scales of waves in equation 2.21. From earlier study (Plant et al., 1999), short and steep waves (including capillary and short gravity waves) are the primary roughness elements supporting the momentum exchange at air-sea interface. The wind sea wave and swell affect the wind stress at the air-sea interface mainly by form drag. The presence of swell changes the wave spectrum as seen in Fig 2 and the corresponding wave-induced stress will change as 2.21. That is the reason swell has been observed to modify the wind stress amplitude and direction at sea surface (Davidson and Frank,1973;Dobson, 1971; Smedman et al, 1994,1999; Drennan et al, 2001). From M-O similarity theory, the wind stress direction is assumed to be the same

as the mean wind direction. Recent research indicates this assumption is not true under swell condition.

We define the direction of the wind stress θ with respect to the mean wind , such that

$$\tan\theta = (-\overline{v'w'})/(-\overline{u'w'}). \tag{2.22}$$

Here positive angles correspond to the stress vector oriented to the right of the wind vector. In many early studies (e.g. Busch, 1977; Large and Pond, 1981; Geernaert et al.,1986), the cross wind stress $(-\overline{v'w'})$ was either ignored or assumed to be insignificant with respect to the $(-\overline{u'w'})$ term. This is consistent with M-O similarity theory (Monin and Obukhov, 1954), which assumes that the stress and wind vectors are aligned in the same direction, and also with measurements over the land.

Smith (1980) used a sonic anemometer to measure wind stress over the open ocean. They found 15% of their data have stress directions $|\theta| > 26°$. While not advocating the practice is general, Smith eliminated these cases from his data set due to uncertainties over possible contamination due to sensor motion. More recently however, such data have been retained, and efforts have been made to understand the physics behind the development of off-wind stress components. Zemba and Friehe (1987), in their aircraft study of a California coastal jet, noted the off-wind stress angle to increase with height from near zero 30m above the surface to almost 60° at 170m. They attributed the shift to Eckman turning of the coastal wind jet. Geernaert (1988) observed that the direction of wind stress may correspond to atmospheric stratification, with the stress angle taking different signs depending on the atmospheric stability (i.e. on whether cold or warm air was advecting over the sea).

In order to consider the wave effect on the wind stress direction, we can analyze the problem in the framework of 2.21 and 2.22. We can get the wind stress direction right above viscous layer as

$$\tan\theta = \frac{\int \beta(k_y)c(k_y)k_y F(k_y)dk_y}{\int \beta(k_x)c(k_x)k_x F(k_x)dk_x} \tag{2.23}$$

where k_x, k_y are the wave numbers in the downwind and crosswind direction. k_y orients to the right of mean wind direction. For swell dominant conditions, if the low frequency swell waves are not inline with wind, the swell-induced stress may cause the wind stress direction to shift away from mean wind direction (Rieder et al., 1994). Generally, higher frequency waves are always assumed to be under the direct effect of wind forcing, so these waves propagate in the same direction with wind (with a spreading angle). Therefore wind sea waves are not thought to cause wind stress direction steering. Air flow over long waves and the presence of short waves on the surface are two elements of a coupled system, which have been described simultaneously. This is also the reason why the wind stress over land is different from over the ocean.

Although the mechanisms about how waves affect wind stress are still vague, many field experiments support this effect. Rieder et al. (1994) presented the wind stress direction in the whole frequency band along with local wave spectra (Figure 2.5). For that case, the wind is directed toward 190° , the swell direction is toward 120° , and we observed the wind stress direction is close to swell direction at swell peak frequency. The high-frequency waves have a quicker response time to turning winds (Masson, 1990), and are close to wind direction. The direction of the stress in the peak frequency of swell is

aligned more closely with the direction of waves at that frequency, and the direction of the wind stress at the high-frequency part is more closely aligned with the waves at those frequencies. That suggests that the fluctuations in the wind field at each frequency may be coupled to the fluctuations in the sea surface at the same frequencies.

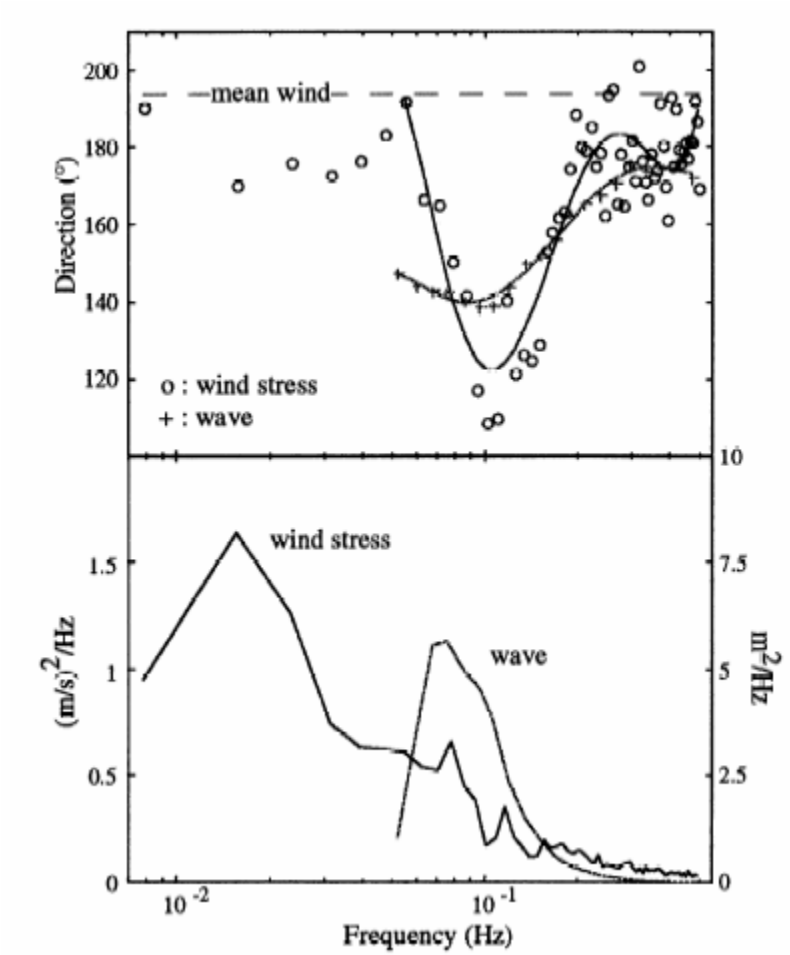

Figure 2.5: (top) direction and (bottom) magnitude of wind stress and waves versus frequency for an 8 hour period. The variations with frequency of the wind stress and wave directions are similar. In this case, the low-frequency stresses are closely aligned with the long waves. Waves with frequencies greater than 0.19Hz have component wave ages less than 1 (From Rieder et al., 1994).

Rieder and Smith (1998) found a clear peak caused by waves in the *u* and *w* cospectra at the wave peak frequency band when swell is strong. From their studies, the wave-correlated, residual, and total stress spectra are plotted in Figure 2.6. The wave influence is represented by a strong peak in the wave-correlated and total stress spectra at

the dominant wave frequencies. For the low wind case (left), the wave-correlated stress represents nearly all the stress in the middle band. Outside these limits, the power in the correlated stress spectrum is nearly one order magnitude below the total. For the right-panel case, the wind is stronger and the stress over all frequencies rises, making the peak at the wave frequencies less visible. In contrast, the residual stress maintains a form that is both simpler and more consistent between the two cases. Some results from other experiments confirm their finding. Grachev et al., (2003) found swell has a significant effect on total stress near the sea surface; the direction of swell and wind can change the vector of the total stress.

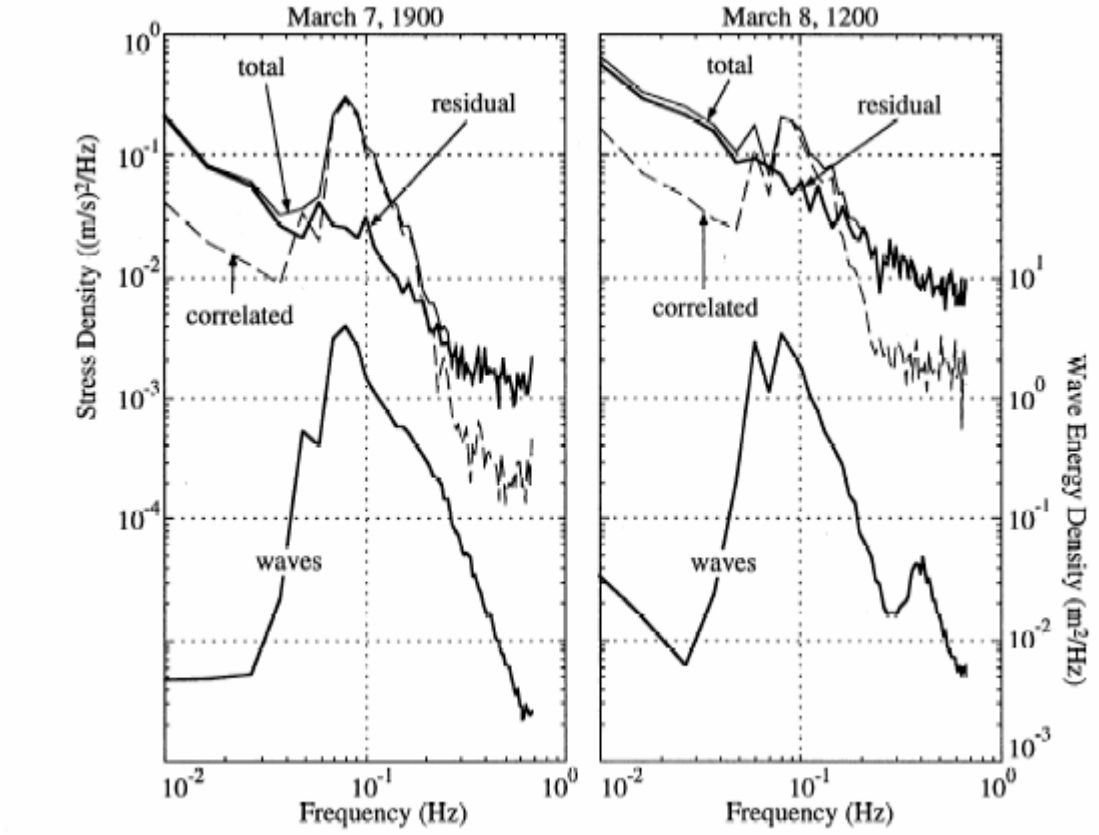

Figure 2.6: Wave-correlated, residual, and total stress spectra versus frequency for the period around (left) March 7, 19:00 and (right) March 8, 12:00. Wind speed for the left and right panel is 5 m/s and 13 m/s. A wave influence is represent by the strong peak in each spectra at the dominant wave frequencies. In the middle band (0.06Hz~0.16Hz), the wave-correlated stress is a large fraction of the total, especially for the first, low wind-speed period. (From Rieder and Smith, 1998)

Wind wave generation, and the momentum flux and energy flux exchange at air sea interface during wind wave generation have been active topics for several decades. The physical mechanisms have been investigated both in theory (Monin and Obukhov, 1954; Miles 1957; Phillips 1957; Janssen 1989; Makin 1995) and in the field experiments (Stewart 1974; Smith 1988; Fairall et al.,1996). Several numerical models to simulate wind wave generation and air-sea interaction have been shown to work well in the pure wind sea condition without swell and current (Booij et al., 1999). However, the real conditions in the open ocean are very complex. Swell waves and ocean currents are known to affect the wind wave generation and momentum flux (Davidson and Frank, 1973; Dobson, 1971; Smedman et al, 1994, 1999; Kelly et al., 2001, 2004; Ardhuin et al.,2007). In addition, the appearance of wave breaking during certain situations can change the sea surface roughness and wave energy distribution across the frequency band. Swell waves, ocean current and wave breaking may not be under the direct forcing of wind in some cases, hence they can cause problems when we apply numerical relations about wind wave generation and air sea interaction from pure wind sea condition. In order to clarify the physical mechanisms and make the numerical relations about wind wave generation and air sea interaction work under real ocean condition, we need to study the problems in the framework of coexisting wind, waves, current and breaking.

2.2.2 Ocean Current Effect on Wind Stress

Some observations of currents affecting wind stress have been reported recently by analysis of remote sensing data (Chelton et al., 2003; Kelly et al., 2001, 2004). To date, no in-situ measurements or laboratory can confirm the findings from space. In my

dissertation, I will use the data from several field experiments to study this problem. Our focus here is on the direction of the stress vector, more specifically on deviations of the stress direction from that of the wind. This issue is of particular relevance to the measurement of winds over the ocean via satellite remote sensing.

Radar scatterometers, such those on QuikSCAT or ERS-1/2, have provided global wind fields operationally for over a decade (e.g. Bentamy et al., 1999). These radars operate by sending microwave pulses to the sea surface and measuring the power backscattered from the surface roughness based on Bragg scattering theory. An empirical model (e.g. Bentamy et al 1999; Wentz and Smith, 1999) is used to relate the backscatter and azimuth angle to wind speed and direction. However, since backscatter is proportional to centimeter-wavelength surface waves (depending on radar frequency and incidence angle), whose growth is proportional to the wind stress, scatterometer measurements are related more to the wind stress than to the wind itself (e.g. Weissman et al, 1994). Hence any deviation of the wind and wind stress directions can lead to an incorrect retrieval of wind direction. These problems have been noted in several scatterometer studies (e.g. Cornillon and Park, 2001; Dickinson et al., 2001). Here we study the problem with a comprehensive in situ data set of wind, wind stress, surface currents and wave measurements, complementing the scatterometer data.

The effect of surface current on wind stress has not been investigated in detail. A current co-linear with the wind is expected to influence the stress through its effect on the relative wind speed. Over much of the ocean, surface currents are wind driven, with a magnitude of 3% of mean wind speed (Wu 1975). In these cases the effect of currents on stress is negligible. However, in equatorial regions or over western boundary currents, the

surface current speed can exceed $1\,ms^{-1}$ (Richardson and Mckee 1984; Weisberg 1984). Current speeds for the Gulf Stream may reach $2\,ms^{-1}$; and tidal flows near coastal areas are as strong. In these regions, the co-linear currents can modify the wind stress magnitude by up to 30%.

Cornillon and Park (2001) removed the mean value of wind vectors retrieved from NSCAT over a warm core ring (Figure 2.7). Where they removed the background wind retrieved from backscattered radar (averaged wind in the study area, upper panel), the residual wind vector (lower panel) correlated with the current vector in the warm core ring. Since backscattered wind is known to measure the wind stress, this shows the surface current modified the wind stress. Kelly et al. (2001,2004) compared the wind velocity measured by QuikSCAT with wind velocity from TAO buoys (middle panel in Figure 2.8), they found the differences in both magnitude and direction of scatterometer winds and in-situ wind measurements, which were attributed in part to surface current by comparing the middle panel and lower panel in Figure 2.8. This is the first direct evidence about wind retrieval from scatterometer to be affected by the surface current. Chelton et al. (2003) attributed some modifications of wind stress measured by QuikSCAT to the effect of surface current.

Drennan and Shay (2006), with in situ measurements of wind, wind stress and surface currents, reported a steering of the stress away from the mean wind direction by almost 30° when the Florida Current intruded into the experimental domain. Although this effect has been reported by the above scatterometer studies, this is the first time it has be observed in an in-situ study (Figure 2.9). Haus (2007) demonstrated that cross-wind

current shear led to reduced wave growth rates and that could be explained by stress veering.

In this study, we investigate the effect of current on the wind stress direction. The magnitudes of current velocity may play an important role in the wind stress. The current velocity can be defined as

$$U_0 = (U_{0X})\vec{i} + (U_{0Y})\vec{j} \tag{2.24}$$

where U_{0X}, U_{0Y} are the current velocity in the mean downwind and crosswind direction. U_{0X} is positive in the downwind direction and the positive U_{0Y} orients to the right of mean wind direction.

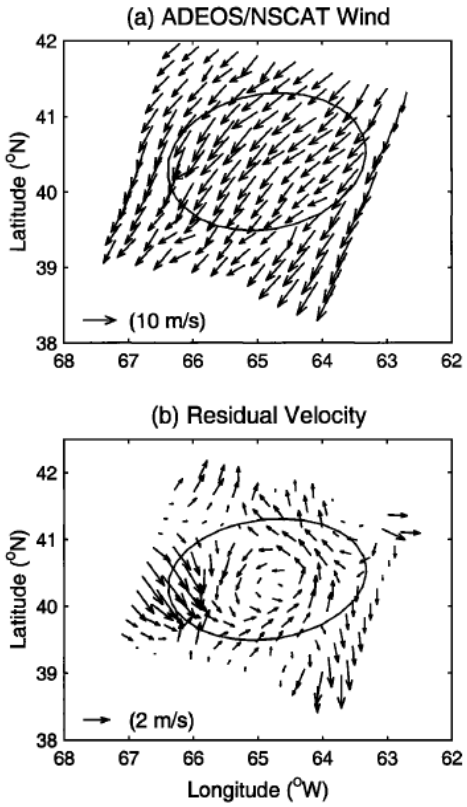

Figure 2.7: An example of the processing of scatterometer data. Upper panel: The scatterometer winds with the outline of a warm core ring. Lower panel: The wind field with the vector averaged wind over the ring removed. (Figure 2 of Cornillon and Park, 2001)

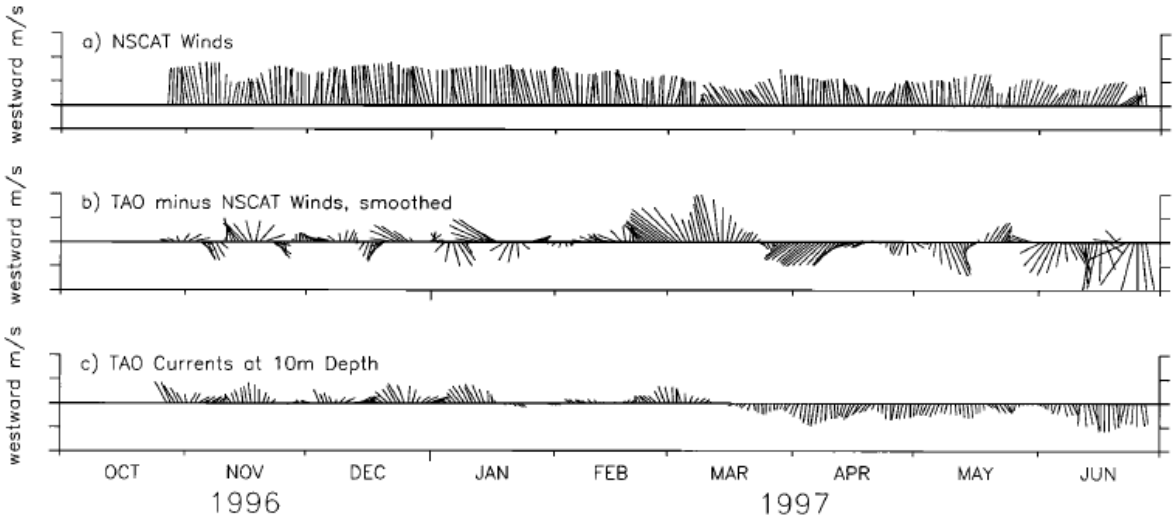

Figure 2.8: Winds and currents at $140°W$ on the equator. (a) Daily averaged winds from NASA scatterometer (NSCAT) for October 1996 to June 1997 (westward is up). (b) The difference between TAO buoy and NSCAT winds. (c) Ocean current from current meters at 10-m depth. (Figure 2 from Kelly et al. 2001)

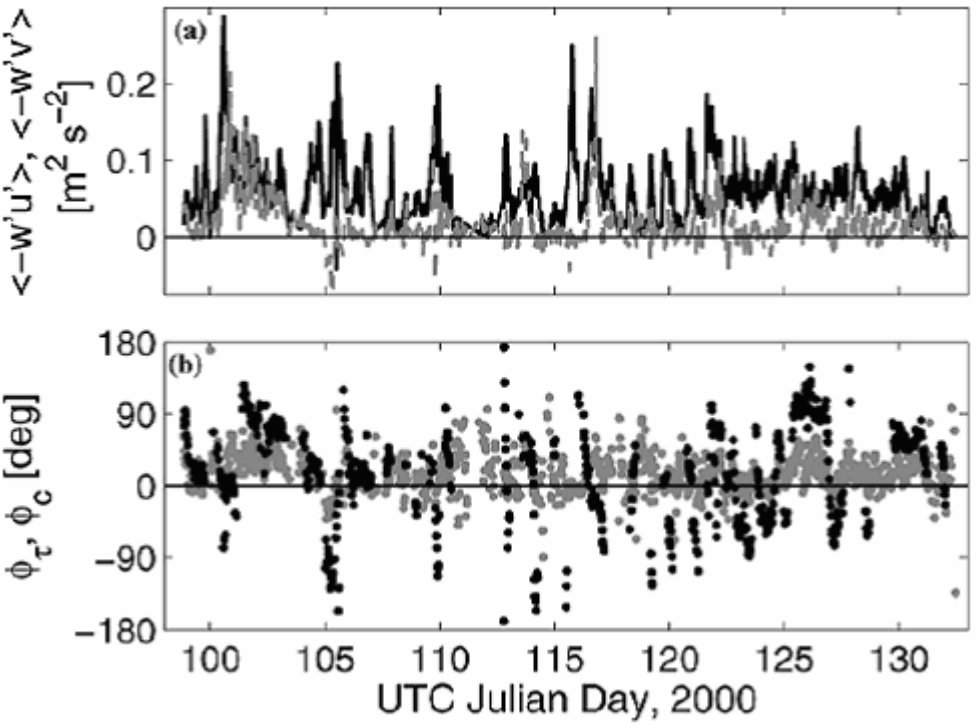

Figure 2.9 (a) along-wind $-\overline{w'u'}$ (solid) and cross-wind $-\overline{w'v'}$ (dashed) stress components during period of an intrusion of the Florida current. (b) relative direction of the stress vector (o), peak waves (●) and surface current (x) with respect to the wind. (Modified from Figure 11 from Drennan and Shay, 2006).

The off-wind current direction has the following relation

$$\tan\theta_c = (U_{0Y}) \Big/ (U_{0X}) \tag{2.25}$$

The angles of current θ_c and wind stress θ have the same direction definition with respect to mean wind; positive angles correspond to orientation of the right of the mean wind direction.

Since the viscous stress is ignored at the measurement height during most field experiments, the current will not affect wind stress direction directly through it. However, current can change the amplitude and direction of the waves propagating into current domain. The key consideration of the wind stress steering by current is surface waves. Assuming no swell exists in the ocean, the wind stress direction results from integrating the effect of waves at all frequency band as indicated by equation 2.21. If wind is stationary in the open ocean in the absence of current, the wind sea waves are typically aligned with the wind; then $\theta = 0$. Once a current is present, current-wave interaction can change the wave direction through wave refraction, which causes the wind stress direction to be variable. We know the wave-current interaction depends on both current velocity and wave frequency (or wave number). The relative stress direction θ also corresponds to the wave number (or wave frequency). In order to study the wind stress shift by current, two problems shall be considered: (1) How are waves at all frequency bands refracted by current? (2) What is the effect on wind stress angle by the waves at all frequency bands?

Wave-current interaction remains as one of the least tested theories in the study of wave dynamics, and the role of large horizontal gradients of the interaction can be

assumed to affect the stress through a complicated set of coupled processes. The purpose of the study is understand the mechanism.

2.3 Current-Wave interaction

The change in a wave field as it propagates into a surface current is analyzed by decomposing the wave field into a series of purely harmonic components. Also the time and length scales of the current are assumed to be much larger than the period and wavelength of the waves. The sea surface displacement at any position $\vec{x}$ and time t can be expressed as the sum of components of angular frequency ω_n and wavenumber $\vec{k}_n$:

$$\eta(\vec{x},t) = \sum_n [\mathrm{Re}(a_n e^{i(\vec{k}_n \bullet \vec{x} - \omega_n t + \varepsilon_n)})] \tag{2.26}$$

with a_n the amplitude, ε_n a random phase and $\omega_n = 2\pi f_n$. f_n is wave frequency and ω_n is angular frequency. For waves propagating on a surface current, $\vec{U}_0(\vec{x},t)$, the angular frequency, measured at a fixed point, includes a Doppler shift:

$$\omega_n = \sigma_n + \vec{k}_n \bullet \vec{U}_0(\vec{x},t) \tag{2.27}$$

where the intrinsic frequency, σ_n, and the wave number are related by the linear dispersion relation. For the deep ocean condition, the problem is simplified by using the deep wave approximation to the dispersion relation,

$$\sigma_n{}^2 = gk_n \tag{2.28}$$

where g is the gravitational acceleration.

2.3.1 Wave Action Conservation

Evaluation of the effect of currents on waves is facilitated by the conservation of wave action (Bretherton and Garrett 1968). This takes the form:

$$\frac{\partial A_n}{\partial t} + \nabla \bullet \left\{ (\vec{C} + \vec{c}^{\,g}{}_n) A_n \right\} = 0 \tag{2.29}$$

where $A_n = E_n / \sigma_n$, E_n is the energy density of the wave train; $\vec{c}^{\,g}{}_n = \dfrac{\partial \sigma_n}{\partial k_n}$ is the group velocity.

The way in which waves and currents are known to interact depends on the incident directional wave field and on the two-dimensional structure of the surface current. The consideration of current-wave interaction under wind forcing is complex, and rare by investigation. However, it may be possible to obtain a reasonable approximation of the interaction by using a local model based on wave action conservation, in which wind-generated waves enter a region of uniform current from quiescent water assuming the balance between wind input energy and dissipation (Huang et al., 1972).

Based on the conservation of wave action, Huang et al. (1972) showed that the unidirectional wave spectrum in deep water $S(\omega, U_0)$, under the influence of current, is related to $S_0(\omega)$, the wind wave spectrum in zero current conditions, as

$$\frac{S(\omega, U_0)}{S_0(\omega)} = \frac{4}{[1 + (1 + \dfrac{4U_0\omega}{g})][(1 + \dfrac{4U_0\omega}{g})^{1/2} + (1 + \dfrac{4U_0\omega}{g})]} \tag{2.30}$$

We assume the uniform current velocity U_0 is inline with the wave propagating direction (i.e., positive for following current)

One serious drawback from this simple model is that, for an opposing current, the theory predicts an unlimited growth of the high-frequency wave components. These short waves are limited in their growth either by reflection or breaking due to excessive steepness.

2.3.2 Doppler Frequency Shifting

Clearly the equilibrium-range waves by wind can also be obtained by other methods. Kitaigorodskii et al. (1975) examined the problem of an equilibrium spectral range in the case of surface waves on a uniform current. Their approach was from the principle, first suggested by Phillips (1958), of a universal shape for wavenumber spectrum in the equilibrium range of a wind wave spectrum. Based on the idea of a saturation range where the wave energy is limited by breaking, Phillips (1958) derived, on dimensional grounds, a wavenumber spectrum, $\Psi(\vec{k})$, of the form

$$\Psi(\vec{k}) = Bk^{-4}G(\theta) \ . \tag{2.31}$$

where B is a nondimensional constant, and $G(\theta)$ the normalized angular spreading function. Assuming that, in the case of a uniform current, the wavenumber spectrum still has an equilibrium range of the universal shape, Kitaigorodskii et al. (1975) derived an expressing for the equivalent frequency spectrum

$$E(\omega) = \int_{-\pi}^{\pi} \frac{\Psi(\vec{k})k}{\partial\omega/\partial k} d\theta \ . \tag{2.32}$$

Using the dispersion relation (2.27) to estimate the factor $\partial\omega/\partial k$ and with the wavenumber spectrum $\Psi(\vec{k})$ given by (2.32), Hedge et al. (1993) made some estimates of wave spectral changes by large-scale currents using an equilibrium range formulation based on (2.31):

$$\frac{S(\omega,U_0)}{S_0(\omega)} = \frac{1}{J(\omega_v,\gamma)} \text{ with } \omega_v = U_0\omega/g \text{ and } J = 1 + 3p\omega_v + q\omega_v^2 \tag{2.33}$$

where p and q are functions of relative angle γ between wind and current and the angular speading function used.

2.3.3 Relative motion

Another way to estimate the wave spectrum is through the momentum flux at the air-sea interface. From wind wave generation theory, the wave spectrum shall be determined by the wind stress, and the wind stress is determined by the relative motion between atmosphere and ocean.

From Phillips (1985), the equilibrium wave frequency spectrum has the form

$$S(\omega) \sim g u_* \omega^{-4} \tag{2.34}$$

Then the equilibrium range wave spectrum considering the relative motion has the relation.

$$\frac{S(\omega,U_0)}{S_0(\omega)} = \frac{u_{*(U-U_0)}}{u_{*(U)}} \tag{2.35}$$

where $u_{*(U)}$ and $u_{*(U-U_0)}$ are the friction velocity at absolute wind speed and wind speed relative to surface current conditions. Figure 2.10 compares the modeled wave spectra on

the basis of (1) wave action conservation (Huang et al., 1972), (2) Doppler frequency shifting (Kitaigorodskii et al., 1975), and (3) relative motion between atmosphere and ocean with the wind wave spectrum under no current condition. Panel (a) is for the current following wind situation and panel (b) is for the current opposing current situation. To begin with, we assume the ocean wave field is represented by the Pierson-Moskowitz (1964)-Phillips(1985) spectrum.

$$S(\omega) \sim \beta g u_* \omega^4 \exp[-\alpha(\omega_0 / \omega)^4] \tag{2.36}$$

where α and β are non-dimensional constants equal to 0.74 and 0.0081 respectively, and $\omega_0 = g / U_{10}$. When wind waves are generated in a uniform current zone, the wave spectrum will change due to the interchange of energy between wave and current (Huang et al., 1972), or Doppler frequency shifting (Kitaigorodskii et al., 1975) or just the modification of wind forcing because of relative motion between atmosphere and ocean. The wind forcing change due to relative motion causes only minor modification for current condition much less than for the wave spectrum change due to Doppler frequency shifting and energy exchange between current and wave. For the opposing current condition, the wave action conservation theory predicts a cut off frequency $\omega_c = -g / 4U_0 = 2.45 s^{-1}$ at $U_0 = 1 m/s$, and wave energy at any higher frequency band is zero; for the current following wind condition, the wave spectra on the basis of wave action conservation theory are lower than no current condition. Doppler frequency shifting will predict an opposite effect to that of wave action conservation theory. Generally, the results from wave action conservation theory seem more close to reality since previous studies indicate rougher surface for current opposing wind

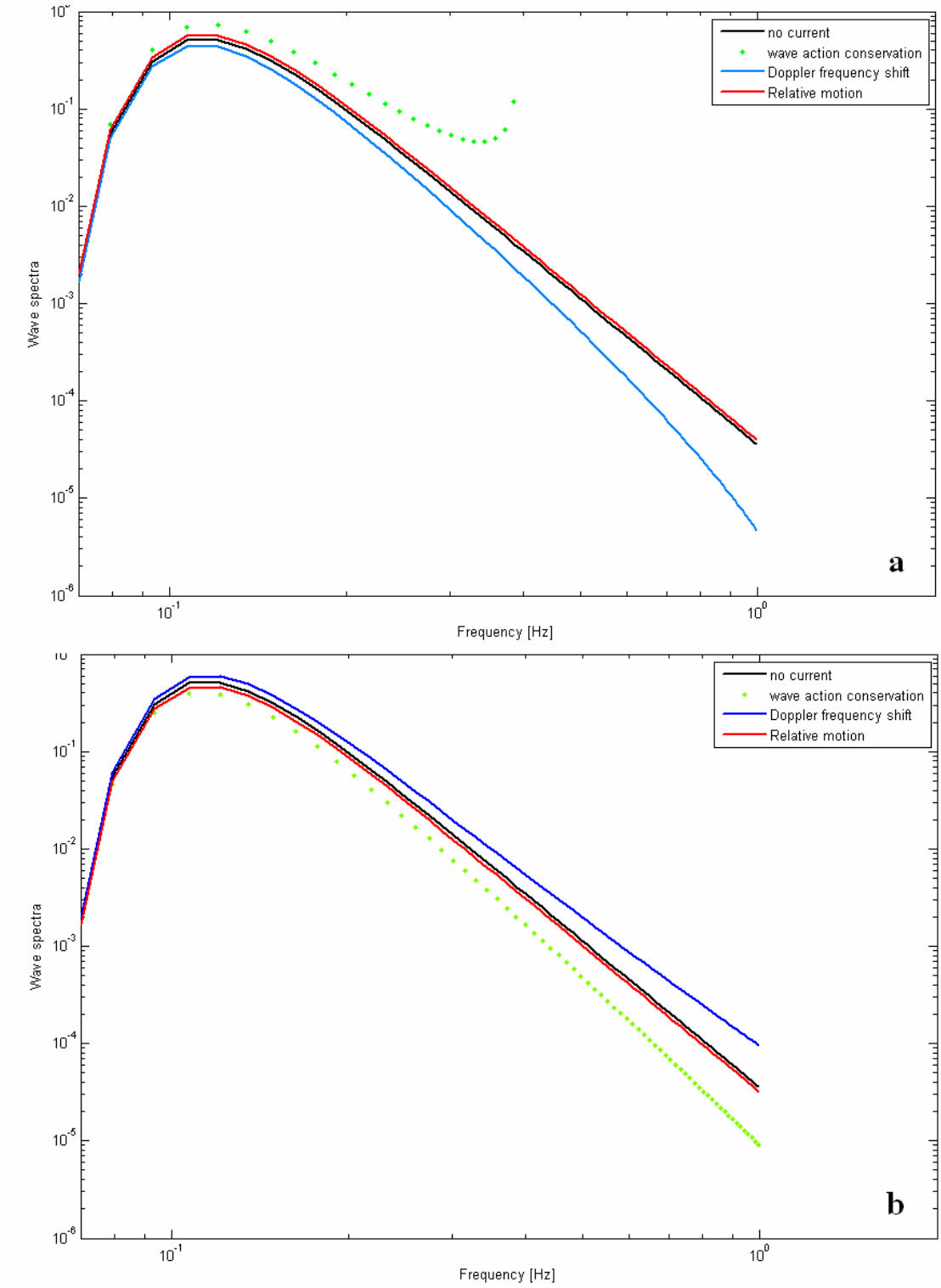

Figure 2.10 (a)Comparison of wave spectra when wind against current condition with 10 m/s wind against 1 m/s current speed; (b) Same as panel (a) with wind in the same direction with current. The wave spectrum under no current (black line); the wave spectrum by Doppler frequency shift (blue line); the wave spectrum by relative motion(red line); the wave spectrum by wave action conservation (green dot).

condition and smoother surface for current following wind condition (Wang et al. 1994; Masson, 1996). We need to know which theory among the three can best predict what happens to wind waves in a current field. Masson (1996) modulated a hybrid wave spectrum in presence of a current. From her research, the energy-containing waves follow the wave action conservation, while equilibrium-range waves will be affected mostly by Doppler frequency shifting. The new wave spectrum with current shows a better comparison as shown in Figure 2.11. Wave tank data from Long and Huang (1976) indicated the measured wind generated wave spectra under current condition have a similar shape to the hybrid wave spectrum of Masson (1996). From Masson (1996) and Long and Huang (1976), the short waves in the equilibrium range have smaller amplitude for opposing current and larger amplitude for following current conditions.

2.4 Wave breaking

The breaking of ocean waves is a commonly occurring phenomenon, often including significant effects which are of fundamental and technological importance. Wave breaking which is categorized as plunging, spilling and microbreaking, is believed to play an important role in the transfer of momentum, mass and heat across the air-sea interface (Melville 1996). Even though we have come to understand wave breaking more in recent years, the detecting of wave breaking, the physical mechanism of wave breaking generation and the effect of wave breaking at the air-sea interface are still not well known because of the physical complexity of the process. Many investigations have been performed to detect breaking waves and estimate the breaking probability in wave tanks

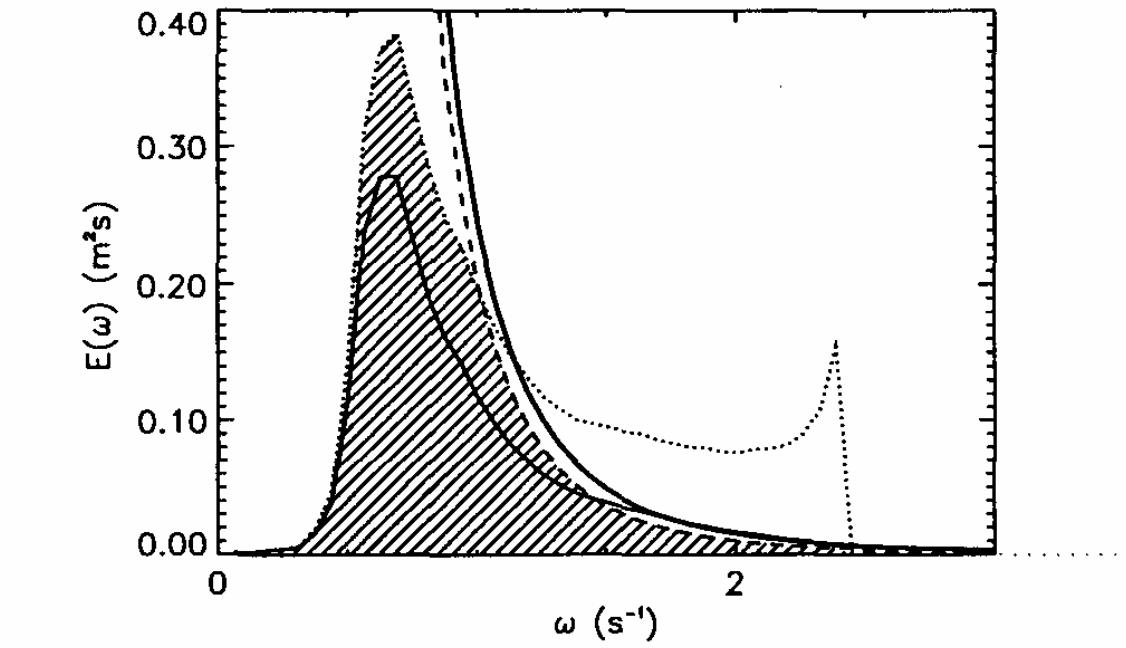

Figure 2.11: Mean frequency spectrum for weak current effect condition (thin full line). The same spectrum interacting with a current $U_0 = -1m/s$ according to the theory of wave action conservation, $E_1(\omega)$ (dotted line). The dashed line shows the equilibrium range spectral parameterization in the opposing current on the basis of saturation range where the wave energy is limited by breaking (Phillips 1958). The shaded area indicates the full spectrum. The equilibrium range with $U_0 = 0$ is also given as the thick full line. The figure is from Masson (1996)

(Xu et al., 1986; Huang et al., 1989). Controlled laboratory studies have also been proven useful in ding the scaling relationships between the surface waves and surface forcing and also improving the understanding of the kinematics and dynamics of breaking.

Many field experiments have shown whitecap coverage to be a function of wind speed (Monahan, 1971; Monahan and O'Muircheartaigh, 1980; Andreas, 1992; Toba and Chen, 1973; Wu, 1979; Lafon et al., 2003). However, the relatively long duration of whitecaps compared to the short life of a breaking wave may result in errors in using whitecap

coverage to represent the wave breaking (Figure 2.12). In order to avoid errors related to whitecap coverage, several studies have tried to quantify breaking probability in the field (Thorpe and Humphries, 1980; Longuet-Higgins and Smith, 1983; Weissman et al., 1984; Holthuijsen and Herbers, 1985; Katsaros and Atakturk, 1992; Xu et al., 2000; Banner et al, 1999, 2002).

Estimating the breaking probability in the ocean depends on either direct observation (visualization) or indirect methods (measuring sound generated by wave breaking). The visualization method is still considered as the most reliable way to count breaking waves, but both experience of the observer and the distance or angle between observer and breaking waves are factors affecting the estimate of breaking probability. Another limitation for the direct observation is the difficult working environment, especially in high wind conditions. Indirect methods (e.g. acoustic) increase the chance to observe breaking waves under the high wind conditions but the lower reliability compared with the visualization method needs to be considered.

For the above reasons as well as complex generating mechanisms of wave breaking, the relationship between breaking probability (Toba et al., 1971;Thorpe and Humphries 1980; Longent-Higgins and Smith,1983; Holthuijsen and Herber,1986) and wind speed presents a lot of scatter, which causes difficulties in extending the relation between breaking probability versus wind speed from the wave tanks to the ocean. However, attempts at confronting these difficulties are justified by the importance of breaking for the processes occurring at the air-sea interface and the requirement of breaking information in wave models.

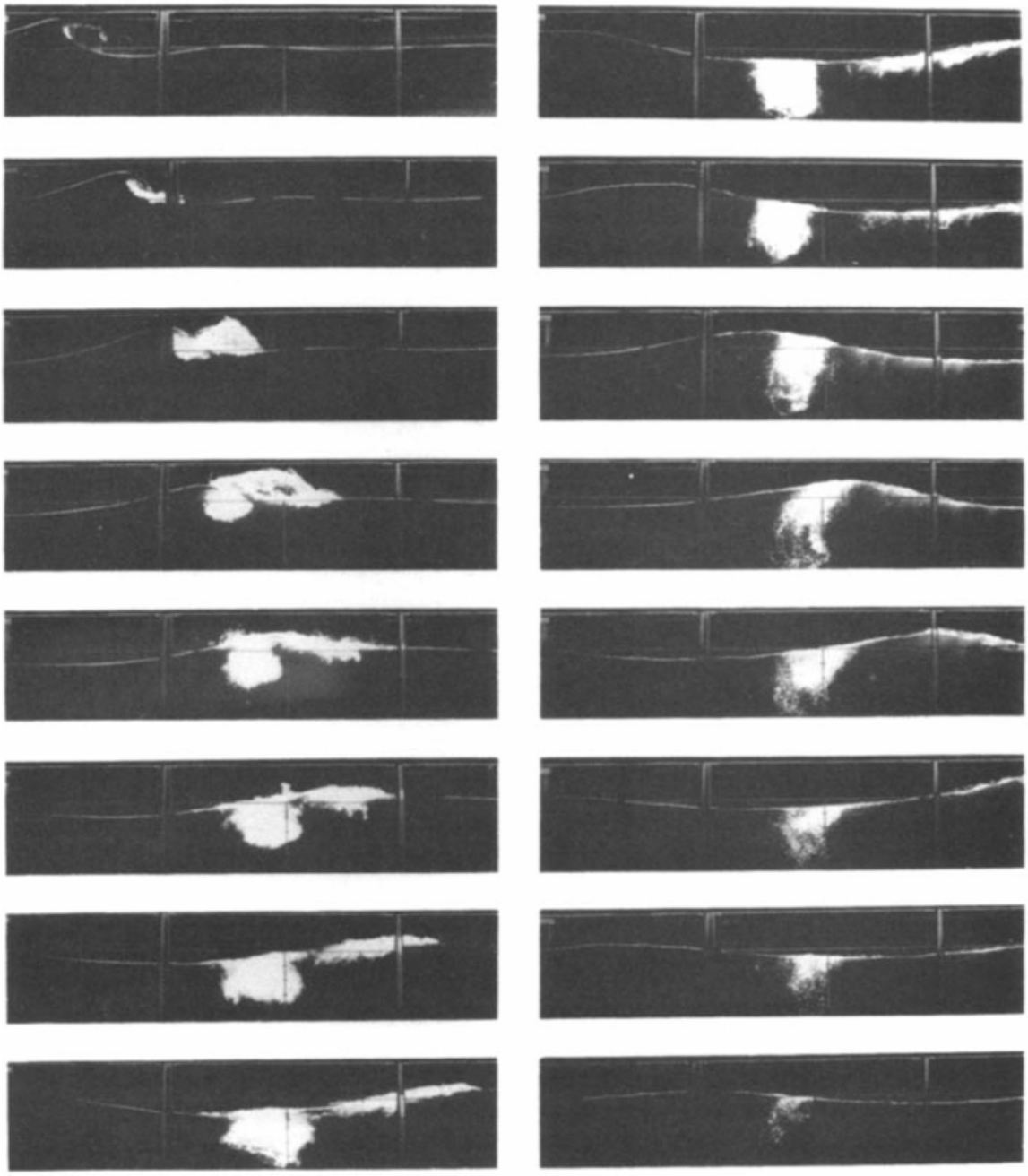

Figure 2.12: Generation of a plunging breaking wave in the laboratory showing significant air entrainment and degassing as large bubbles rise back to surface (Modified from Figure 2 in Melville, 1996)

In the laboratory, researchers have proposed several different breaking criteria to detect wave breaking through surface elevation data (Xu et al., 1986; Huang et al., 1989). Some of these criteria have been proven successful in various lab experiments. (Xu et al., 1986;

Huang et al., 1989). In this dissertation, breaking criteria using local parameters for breaking detection are applied to wave staff data collected in the ocean by Air-Sea Interaction Spar (ASIS) buoys (Graber et al., 2000). We test the feasibility of applying local criteria in the field and use the measured breaking data to understand the environment effect on breaking probability through the analysis.

Our studies about air-sea interaction, current-wave interaction, and wave breaking are on the basis of the field data. In the next Chapter, we will introduce the instruments and experiments related to my studies.

Chapter 3

Equipment and Experiments

The field data we use in this dissertation are from two nearshore experiments: the 1999 Shoaling Wave Experiment and the 2003 Baltic Swell Experiment. The two experiments will be described in the section 3.2. In each experiment, Air-Sea Interaction Spar buoys (ASIS) are used as platforms to measure the wind stress, wind and waves in the ocean. An Ocean Surface Current Radar (OSCR) is used to collect current vector maps in the experimental domain. Scatterometer wind data in the experimental domain are obtained from QuikSCAT. In order to study the current-wind interaction, we also apply the Simulating Wave Nearshore Model (SWAN) to simulate current-wave interaction in the field experiments. In the following, we will introduce the equipment, model and field experiments.

3.1 Equipment

3.1.1 Air-Sea Interaction Spar Buoy

During the experiments, ASIS buoys (Fig. 3.1) were equipped with one or more Gill 3-axis Solent sonic anemometers (model 1012R2A) at several meters height from the surface. Sonic anemometers measure three orthogonal components of the wind $\vec{u}_B = (u_b, v_b, w_b)$. A motion package, including 3 orthogonal pairs of rate gyros (Systron

Figure 3.1: The fully-loaded ASIS buoy as deployed during a field experiment. Three Sonic anemometers and two thermistors are installed on ASIS buoy.

Donner GC1-00050-100) and linear accelerometers (Columbia Research Laboratory SA-307HPTX) and a compass (Precision Navigation TCM-2), was installed in an underwater housing to measure the three orthogonal components of linear acceleration, $\vec{a}_B = (a_{b1}, a_{b2}, a_{b3})$, and three components of rotational motion, pitch (θ), roll (ϕ) and yaw (ψ) (Figure 3.2). These motion data are used to transform the wind components to a stationary frame based on an algorithm given by Anctil et al. (1994) and Graber et al. (2000):

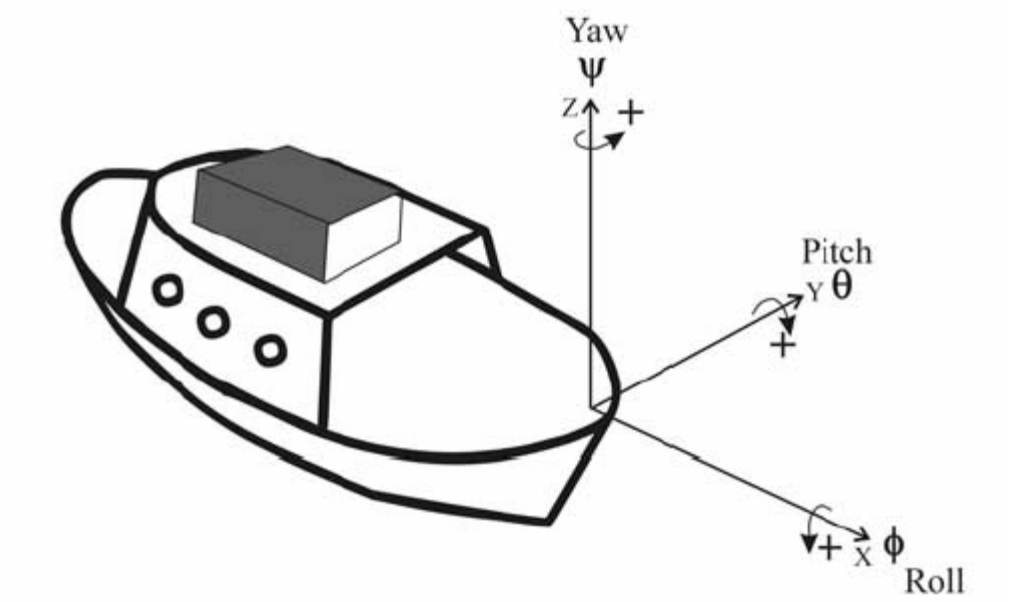

Figure 3.2: Coordinate system used in the application of eddy correlation method. (From Pedreros et al. 2003)

(1) Given the rotational motion, we can write down the rotation matrix $\vec{T}_{BE}$ which transforms measurements taken in the buoy reference frame to earth coordinates, by following Goldstein (1950):

$$\vec{T}_{BE} = \begin{pmatrix} \cos\theta\cos\psi & \sin\phi\sin\theta\cos\psi - \cos\phi\sin\psi & \cos\phi\sin\theta\cos\psi + \sin\phi\sin\psi \\ \cos\theta\sin\psi & \sin\phi\sin\theta + \cos\phi\cos\psi & \cos\phi\sin\theta\sin\psi - \sin\phi\cos\psi \\ -\sin\theta & \sin\phi\cos\theta & \cos\phi\cos\theta \end{pmatrix} \qquad (3.1)$$

The sonic anemometer measurements were converted to an earth reference frame using the transformation matrix $\vec{T}_{BE}$.

(2) Compensation for the axial motions of the buoy by integrating the measured linear accelerometer signal $\vec{a}_b$ and using $\vec{T}_{BE}$ to transform buoy referenced values to earth referenced ones. The acceleration due to gravity, $\vec{g} = (0,0,-g)$, is also account for.

(3) Accounting for the angular velocities induced by the buoy's rotations, since the anemometer is located at some distance, $L_B = (L_x, L_y, L_z)$, from the motion sensor. Here $L_B \approx (0.2, 0.2, 12)$. The angular velocity of the buoy is given by

$$\vec{\Omega} = \begin{pmatrix} -\dot{\theta}\sin\psi + \dot{\phi}\cos\theta\cos\psi \\ \dot{\theta}\cos\psi + \dot{\phi}\cos\theta\sin\psi \\ \dot{\psi} - \dot{\phi}\sin\theta \end{pmatrix}, \tag{3.2}$$

where the dot above a symbol represents the derivative of the quantity with respect to time. The angular velocity at the sonic anemometer is then given by $\vec{\Omega} \times T_{BE} L_B$.

Combining the three components, we can write the motion corrected wind speed as

$$\vec{u} = \vec{T}_{BE}\vec{u}_B + \vec{T}_{BE}\int(\vec{a}_B + \vec{g})dt + \vec{\Omega} \times \vec{T}_{BE} L_B \tag{3.3}$$

All signals are sampled at 20Hz for 60-minute periods, and the data are processed in blocks of 20 or 30 minutes. The momentum flux (eddy correlation) and velocity profile are obtained after motion correction. An average tilt correction is used to force $\overline{W} = 0$.

ASIS is equipped with an 8-element array of capacitance wave gauges (a centered pentagon of 1-m radius with 3 gauges in the center). The wave array data are corrected for the motion of the buoy (Drennan et al., 1994; 1998). The maximum likelihood method is then applied to obtain directional wave spectra (Capon, 1969). Finally, the wave partitioning method (Gerling, 1992), which is used to characterize wave systems from temporal sequences of directional wave spectral estimates, is applied. The wave partitioning method decomposes the wave field into wave trains. Normally the wave field includes several wave trains. A wave train is bounded by local minima around a peak with the constraint that the energy spreading is less than 45^o on both sides of peak

frequency. The mean period, mean propagation direction, and energy of each wave train are calculated. The energy of each wave train is defined as $E = \iint S_{\eta\eta}(f, \theta_w) d\theta_w df$ where $S_{\eta\eta}$ is the two dimensional energy spectrum of surface elevation (η), f is the frequency and θ_w is propagation direction (Drennan et al. 2003). For future reference we introduce σ, the RMS surface elevation, and the significant wave height, $H_s = 4\sigma = 4E^{1/2}$.

3.1.2 Ocean Surface Current Radar

Ocean Surface Current Radar (OSCR) is a High-Frequency (HF) radar. During the operation of HF radar, a vertically polarized HF signal is propagated at the ocean's electrically conductive water surface. The ocean is a rough surface, with water waves of many different periods. When the radar signal hits ocean waves that are 3-50 meters long the transmitted signal scatters in many directions. In this way, the surface can act like a large diffraction grating. The radar signal will return directly to its source only when the radar signal scatters off a wave that is exactly half the transmitted signal wavelength, and that wave is traveling in a radial path either directly away from or towards the radar. The scattered radar electromagnetic waves add coherently resulting in a strong return of energy at a very precise wavelength. This is known as the Bragg principle, and the phenomenon is known as 'Bragg scattering'.

What makes HF Radar particularly useful for current mapping is that the ocean waves associated with HF wavelengths are almost always present. OSCR radar can operate under two transmitted frequencies (Stewart and Joy, 1974). The 25.4 (44.9) MHz

corresponds to a 12 (6) m EM wave, which will scatter from a 6 (3) m surface wave. Here we use OSCR at transmitting frequency at 25.4 MHz. The details of HF radar properties are in Table 1.

So far three facts about Bragg waves are known: their wavelength, period, and travel direction. Because we know the wavelength of the wave, we also know its speed very precisely from the deep water dispersion relation. The returning signal exhibits a Doppler-frequency shift due to surface currents. In the absence of ocean currents, the Doppler frequency shift would always arrive at a known position in the frequency spectrum. In fact the observed Doppler-frequency shift does not match up exactly with the theoretical wave speed. The Doppler-frequency shift includes the theoretical speed of the wave plus the influence of the underlying ocean current on the wave velocity in a radial path (away from or towards the radar). So, once the known, theoretical wave speed is subtracted from the Doppler information, a radial velocity component of surface current is determined. By looking at the same patch of water using radars located at two or more different viewing angles, the surface current radial velocity components can be summed to determine the total surface current velocity vector.

Direct comparison of remotely sensed current velocities with point measurements is complicated by the different sampling strategies. The HF radars sample the current over a ~1 m thick slab working at 25.4 MHz transmitted frequency. In regions of high horizontal or vertical shear a single point measurement may differ significantly from that of OSCR (Graber et al., 1997). A comparison of the OSCR derived surface currents with a Vector Measuring Currrent Meter with $0.02 m/s$ accuracy at 4 m depth revealed only $0.07 m/s$ rms differences during Duck94 (Shay et al. 1998). The standard deviations of the velocity

difference were 0.11 and 0.22 m/s for the east-west and north-south components respectively.

Table 1: OSCR System Capabilities and Specifications

	HF
Frequency (MHz)	**25.4**
Resolution (km)	**1**
Range (km)	**40**
Measurement cycle (min)	**20**
Spatial coverage (km^2)	**700**
Maximum number of measurement points	**700**
Data Storage (days)	**120**
Transmitter Peak Power (KW)	**1**
Transmitter Average Power (W)	**2**
Power Consumption (KW @ 240V)	**1**
Transmit antenna elements (Yagi; 6dB gain)	**4**
Receive antenna elements (phased array)	**16**
Accuracy: Radial current (cm/s)	**2**
Accuracy: Vector current (cm/s)	**4**

3.1.3 QuikSCAT

The SeaWind scatterometer on QuikSCAT satellite is a Ku-band microwave radar launched on June 19, 1999 and operated by the National Aeronautics and Space Administration (NASA). From 25-km resolution measurements across a 1600-km swath,

QuikSCAT samples more than 90% of the global ocean every 24 hours. During the Shoaling Wave Experiment (SHOWEX), the SeaWind radar scanned the area covered by OSCR twice each day. The scatterometer on QuikSCAT sends Ku-band microwaves to the ocean surface and measures the normalized radar cross-section (NRCS), which is the signal backscattered by the centimeter scale waves on the sea surface. While short waves of this scale are generated by the wind stress at the surface, the primary QuikSCAT product is the wind vector. Ocean currents are known to affect the wind vectors from QuikSCAT by modifying the NRCS (Chelton et al., 2003). In order to study the current effect on wind stress and wind vectors from QuikSCAT, level 2B (wind vector) data from Jet Propulsion Laboratory are used to compare with the wind vectors from ASIS buoys. Since the empirical model function to drive level 2B data does not include any ocean current parameter, we expect to observe an effect of current on wind stress by comparing the wind vectors from QuikSCAT with ASIS data.

3.1.4 Air-Sea Interaction Salt Water Tank

The Air-Sea Interaction Salt Water Tank (ASIST) at the University of Miami is especially well suited for studies related wave breaking. The centerline wind speed can be programmed in the range of 0 to 30 m/s. The tank is 15 m long in its working section and 1 m wide with its height of 1 m divided equally between air and water. The tools for measuring stress include hot-film anemometry, digital particle image velocimetry (DPIV) and laser/line scan cameras for measuring the water surface elevation with great precision, about 10^{-4} m. Two elevation measurements over 10 m thus yield slope precision of $10^{-5.}$

Fluxes of momentum, heat and mass across the air-water interface including the exchange of gases and aerosols can also be measured in the tank. Here, we are using the data from tank to study breaking waves.

3.1.5 SWAN Wave Model

In order to investigate the influence of current on the wind wave generation, we use the Simulating Wave Nearshore (SWAN) model (Booij et al.,1999). SWAN is a third-generation wave model designed to overcome traditional difficulties of applying wave action in coastal regions. SWAN can describe the evolution of the two-dimensional wave energy spectrum in arbitrary conditions of wind and current. It assembles all relevant processes of generation, dissipation, and nonlinear wave-wave interaction in a numerical code that is efficient for small scale, high-resolution applications. The directional wave spectra from SWAN can be easily compared with those from ASIS buoys. This comparison between wave model and buoy data will be made in the following Chapter. Here we present the basic principles behind the model.

Including the effect of the ocean current, the wave evolution problem can be formulated with a balance equation for the wave action. The governing equation for SWAN is

$$\frac{\partial A}{\partial t}+\frac{\partial C_{gx}A}{\partial x}+\frac{\partial C_{gy}A}{\partial y}+\frac{\partial C_{g\sigma}A}{\partial \sigma}+\frac{\partial C_{g\alpha}A}{\partial k}=\frac{S_{all}}{\sigma}. \tag{3.4}$$

The wave action density is equal to the energy density divided by the relative frequency $A = E/\sigma$. The first term in the left-hand side of (3.4) is the local rate of change of wave

action density, the second and third terms are the propagation of wave action in (x,y) directions with propagation velocities C_{gx} and C_{gy}. The fourth term is the shifting of the relative frequency due to variation of depth and current (with propagation velocity $C_{g\sigma}$ in σ space). The fifth term represents depth-induced and current-induced refraction (with propagation velocity $C_{g\alpha}$ in wave number space). S_{all} is the total of source/sink terms expressed as wave energy density. S_{all} represents the effects of wind generation, nonlinear wave-wave interaction and dissipation, so $S_{all} = S_{in} + S_{nl} + S_{di}$.

The effect of quartet wave-wave interactions is represented by the scattering term S_{nl}, which represents the effect of transferring energy from the spectral peak to lower and higher frequencies. The energy transferring to lower frequency leads to the lower peak frequency and the transfer to higher frequency leads to energy dissipation by breaking. This term in SWAN is parameterized using the Discrete Interaction Approximation (DIA) by Eldeberky (1996). DIA is taken because the full computation of the quadruplet wave-wave interactions is extremely time consuming and not convenient in any operational wave model. The DIA technique is based on the studies by Abreu et al. (1992) who described triad wave-wave interactions in terms of a spectral energy source term initially, followed by Eldeberky and Battjes (1995) who extended the previous expression from shallow water waves to wind waves.Wind input in SWAN is expressed as the sum of linear and exponential wave growth

$$S_{in}(\sigma,k) = A_a + B_b E(\sigma,k) \tag{3.5}$$

Exponential wave growth B_b is typically larger than linear wave growth a_1 by one or more orders of magnitude. For the term B_b, two optional expressions are used in the

model. The first is taken from an early version of the WAM model, which is due to Snyder et al. (1981) and Komen et al. (1984). The momentum flux from wind to wave is quantified by the bulk relation of Wu (1982). It has the form,

$$B_b = \max\{0, 0.25\frac{\rho_a}{\rho_w}\left[28\frac{u_*}{C}\cos\theta_{wind-wave} - 1\right]\} \tag{3.6}$$

where ρ_a and ρ_w are the densities of air and water, C is wave phase velocity, $\theta_{wind-wave}$ is the angle between wind and wave.

The loss of wave energy owing to whitecapping and its spectral distribution S_{ds} is more complex and uncertain than quartet wave-wave interactions and wind input energy. Most of the parameterization used here follows Donelan and Yuan (1994), who use the pulse-based model of Hasselmann (1974). The weak point in this family of parameterizations is the definition of a spectrum-averaged steepness, which leads to anomalous swell effects on wind wave growth. The present simulation focuses on the directional wind wave spectra under uniform current, and we neglect the impact of swell. SWAN can quantify change of the wave height and wave length by current, and the change can easily add to the overall wave steepness by wind, therefore the direct loss of energy of wind sea owing to whitecapping can therefore be correctly parameterized since the whitecapping is caused by co-forcing of the wind and surface current.

In this study, we just want to know the properties of the directional wind wave spectra under uniform current, so we turn off some options such as depth-induced wave breaking and dissipation of bottom friction.

3.2 Experiment

3.2.1 Shoaling Wave Experiment (SHOWEX)

SHOWEX took place off Duck, North Carolina during October-December 1999. The goal of this experiment was to improve the scientific understanding of the properties and evolution of surface gravity waves in intermediate- and shallow-water depths (typical of inner-continental shelves up to the edge of the surf zone). The focus for this research was driven by a range of U.S. Navy needs including improving wave forecasts, understanding the interactions between waves and acoustical and optical processes, air–sea interaction, remote sensing, forces on vessels and structures, and sediment transport issues. The experimental region (Figure 3.3) is interesting for air-sea interaction research as it is influenced by several distinct sources of forcing: the Chesapeake Bay buoyancy current, the Gulf Stream, swell waves propagating onshore, and winds from a variety of directions. During SHOWEX, the OSCR system was deployed starting on 27 October (YD 300) and ending on 10 December (YD 344). OSCR consisted of two HF radar transmit/receive stations. The master station was located at $36°11'N, 75°49'W$; the slave was located at $36°25'N$, $75°50'W$ (Figure 3.3). Three ASIS buoys were deployed for the SHOWEX experiment. Bravo was deployed on YD 302 at $36°14'N, 75°40'W$ at a depth of 20m. Yankee was deployed the next day at $36°25'N, 75°31'W$ in 25m. Romeo was deployed at $36°26'N, 75°15'W$ seven days earlier than Yankee. Bravo operated continuously until late on YD 326 when the anemometer failed due to power limitations. Yankee and Romeo, with extra batteries, operated continuously until recovery on YD 347.

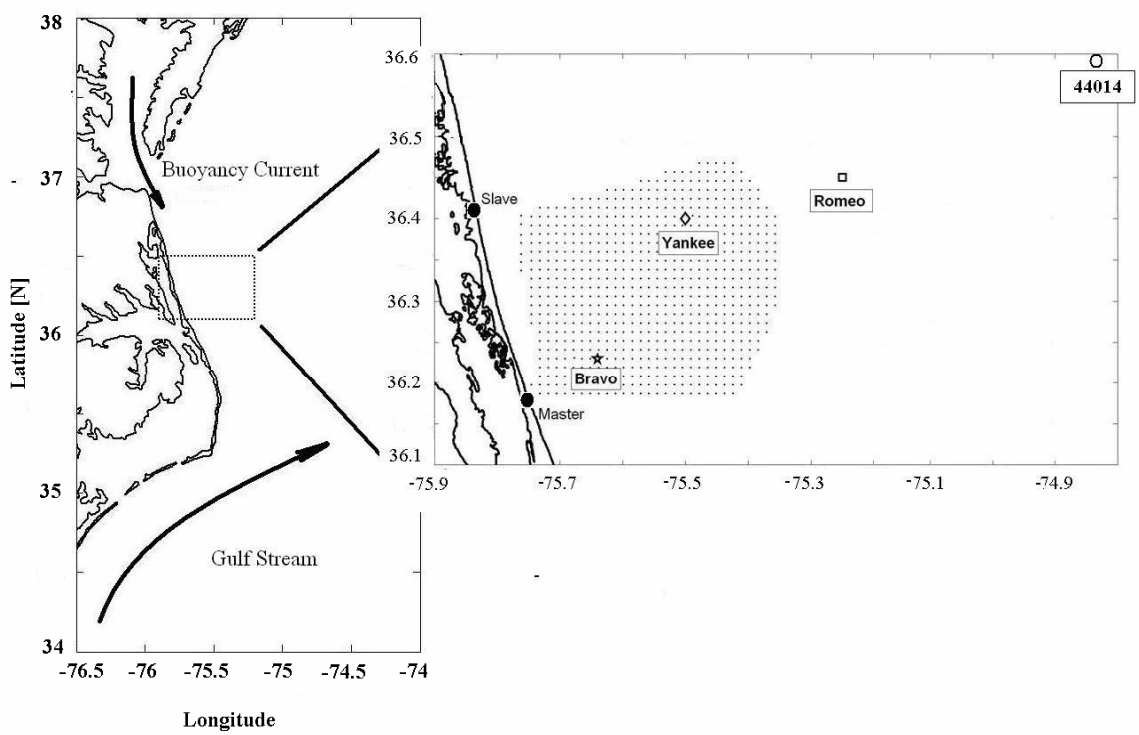

Figure 3.3: Left: Location of Shoaling Wave Experiment at the Duck, North Carolina showing the OSCR cell (dots), the Air Sea Interaction Buoys (Bravo-star; Yankee-diamond; Romeo-square) The circle is National Buoy Center buoy 44014. The master and slave sites for the HF radar (black circles) were located at the shore.

The conditions experienced during SHOWEX are summarized in Figure 3.4. Figure 3.4a shows the atmospheric pressure from NDBC buoy 44014 near the SHOWEX domain. Figure 3.4b shows the 10-m neutral wind speed at Yankee. The QuikSCAT wind speeds from the cell including Yankee are also plotted. The two groups of data have generally good agreement with a correlation coefficient $\gamma = 0.93$ in the whole experiment. The wind direction from QuikSCAT and ASIS has a correlation coefficient $\gamma = 0.83$ (Fig. 3.4c).

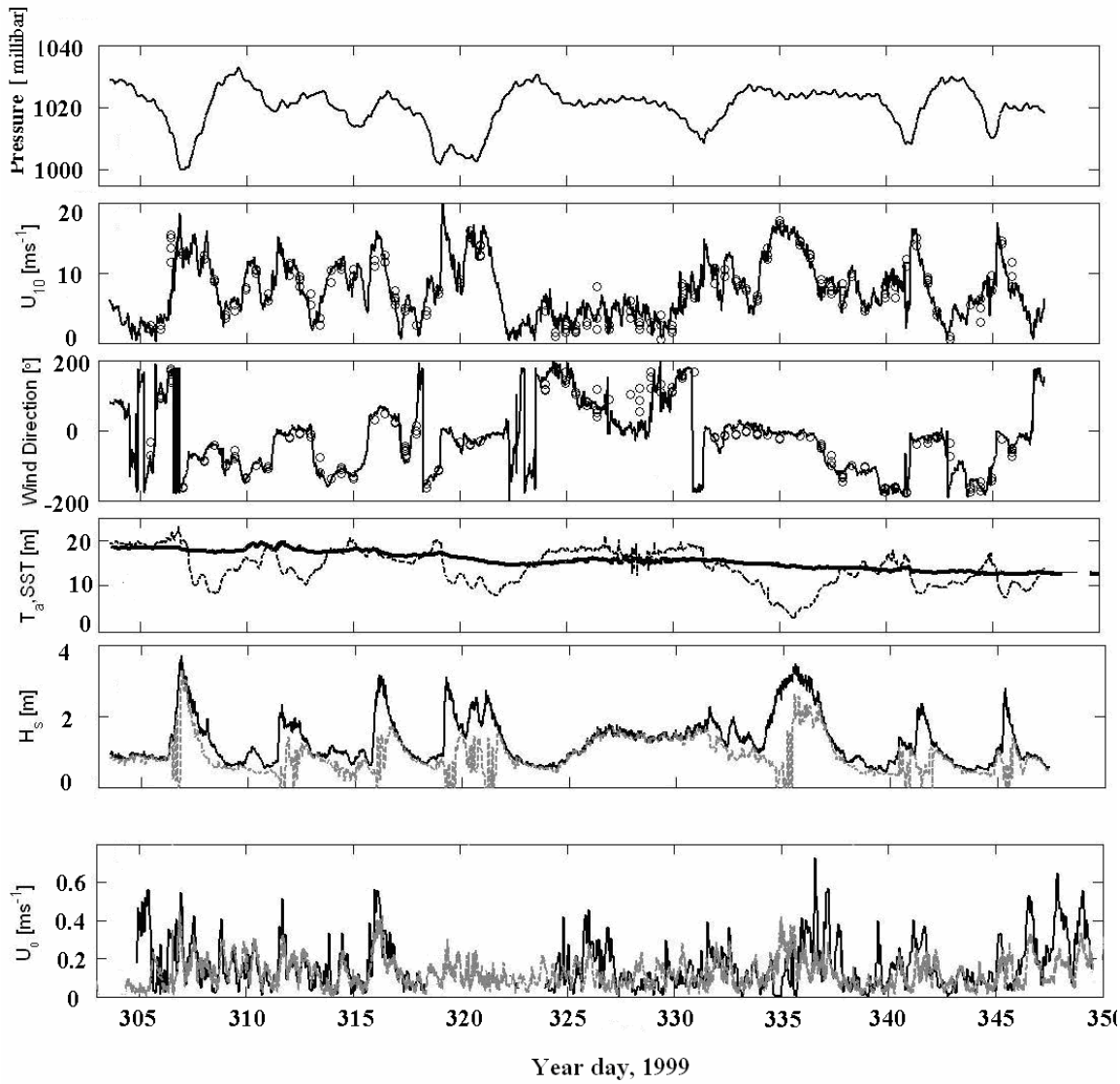

Figure 3.4. Summary of meteorological conditions and sea states during SHOWEX using the data from Yankee except indicated. The panels show: (a) The atmospheric pressure from NDBC buoy 44014. (b)10-m wind speed (black line) and QuikSCAT (circle). (c) wind direction (black line) and QuikSCAT (circle). (d) air temperature (gray solid) and water temperature(dashed). (e) significant wave height (black line) and Significant swell height (gray line). (f) current speed from OSCR (black) and current meter at 5 meter depth (gray).

Of particular note are the dramatic drops in air temperature following the offshore passage of cold fronts (Fig. 3.4d). The gradual seasonal cooling of the shelf waters is also seen in panel d. The significant wave heights of total waves and swell are shown in panel

e. The surface current, from the OSCR cell closest to Yankee, and the current at Yankee from current meter at 5-meter depth show good agreement in the majority of cases (Fig. 3.4f). The differences between the two measurements can be mainly attributed to the depth difference (Graber et al., 1997). Previous observations by Haus et al. (2003) and Rennie et al. (1999) have revealed the presence of coastal buoyancy currents from Chesapeake Bay. During SHOWEX, these strong along-coast currents from the north were observed following strong rainfall events in the Chesapeake Bay drainage basin.

3.2.2 Baltic Swell Experiment (BASE)

The BASE experiment took place during fall 2003 near the island of Östergarnsholm in the Baltic Sea. Direct (eddy correlation) measurements of momentum flux at two different heights (2.51m and 5.56m) were made from a moored Air-Sea Interaction Spar buoy.

As shown in Figure 3.5, an ASIS buoy was deployed about 6 km SSE of Östergarnsholm Island ($57^o25'N\ \ 19^o3.3E$) in 45-m water depth. Östergarnsholm is an island situated about 4 km east of the main island of Gotland in the Baltic Sea (Figure 3.5). It is small ($\sim 2\times1\ \ km^2$), low and flat with a few trees. The peninsula in the southeast part of Östergarnsholm is about 1 km long and no more than a couple of meters above the mean sea level. At the southernmost tip of the peninsula there is a 30 m high tower. The distance from the tower to the shoreline is some tens of meters in the sector $80° \sim 220°$.

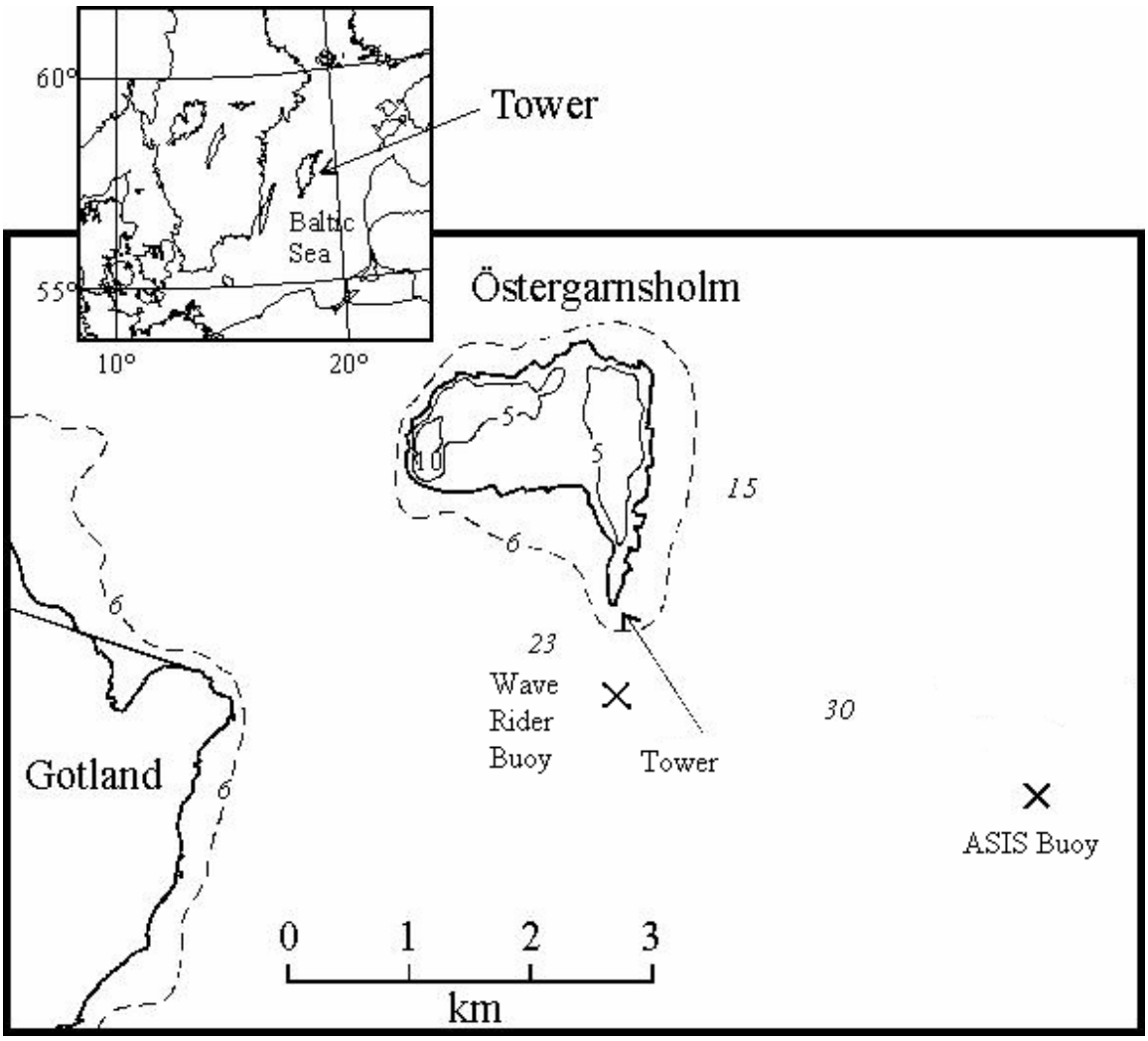

Figure 3.5 Map of the experiment site. The ASIS buoy is moored in 45m-deep water; 4 km to the SSE of the tower site on Ostergarnsholm. (Modified from Smedman, 1999)

The tower base is situated about 1 m above the mean sea level. The actual heights of measurements are corrected with the aid of water level measurements at Visby harbor, situated at the western coast of the island of Gotland (Sjöblom and Smedman, 2002). Östergarnsholm is exposed to open-ocean conditions when winds are coming from an easterly or southerly direction (about $80° \sim 210°$). The undisturbed water fetch is over 150 km in this sector. The slope of the sea floor right offshore of the peninsula is approximately 1:30 down to a depth of 19 m, and 1:17 further out to the south and the

ratio becomes even smaller further out. The possible influence of limited water depth on the tower measurements has been carefully studied in Smedman et al. (1999). In September and October, strong swell/weak wind is expected to happen frequently (Smedman et al., 1994). Furthermore the wind is expected to be in-line with the swell at the experiment site. This is rare in the open sea. The tower can measure the wind speed and direction at 5 levels: 7, 12, 14, 20, and 29 meters above the tower base. Wave measurements are made from the ASIS buoy and also by Kahma and Pettersson of Finnish Institute for Marine Research (FIMR) from directional wave-rider buoys moored 1 km and 3 km offshore of the tower.

The experiment in the Baltic was conducted from 3 September, to 27 October 2003. During this time, the system stopped working from 10 October to 23 October, because the batteries were out of power. A total of 1809 30-minute time series of atmospheric and oceanic information were collected during nearly 40-day experiment.

The conditions during BASE are summarized in Figure 3.6. The 10 m neutral wind speed is plotted in Figure 3.6a; the momentum flux (downwind direction) is shown in Figure 3.6b. The air-sea temperature difference is typically small ($\pm 2^{o}C$), except for the last three days of the whole experiment, when the temperature difference (see Figure 3.6c) between air and water is around $4^{\circ}C$, this is a very unstable condition. The significant wave height is given in Figure 3.6d. The highest waves always occur with the highest wind speed. Also shown is the inverse wave age (Figure 3.6e).

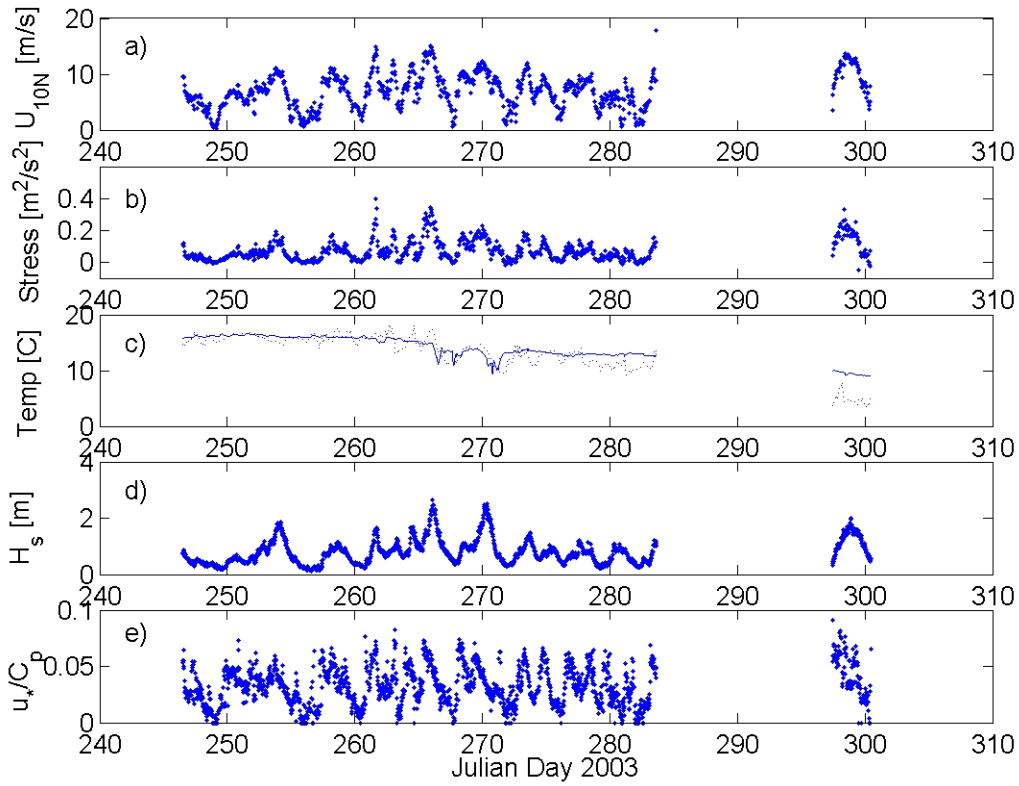

Figure 3.6: Meteorological and wave condition during BASE. The data shown are (a) 10 m neutral wind speed, (b) inline-wind stress, τ / ρ [$m^2 s^{-2}$], (c) air (dotted) and sea temperatures, (d) significant wave height, and (e) inverse wave age.

Chapter 4

Wind Stress Direction Shift due to Wave-Current Interaction

Although there has known to be an effect of current on the wind stress for decades, to date the supporting measurements have been indirect via remote sensing. Direct measurements which show the effect of current on wind stress are very rare. In this Chapter, we use the data from the SHOWEX experiment to study this problem. Our studies here focus on the wind stress direction shift as a result of a current. The current effect on the wind stress amplitude will not be considered here since the current speeds are too small compared with the mean wind speeds during the experiment.

4.1 Wind Stress Shifting

The wind speeds and directions from both Bravo and Yankee buoys from YD 305 to 318 during SHOWEX, when both buoys and the radar were functioning, were chosen for in-depth analysis. Romeo is out of the OSCR domain so we don't consider its data here. As noted previously there are several occasions when the wind stress direction was significantly different from that of the mean wind (Figure 4.1). Most notable was the 25 hour period starting around 14 UTC on Day 307, when relative stress angles of order 30° were seen for extended periods at both buoys. The wind stress direction shifting in Figure 4.1 is partly caused by the current effect; we will focus on this in this chapter.

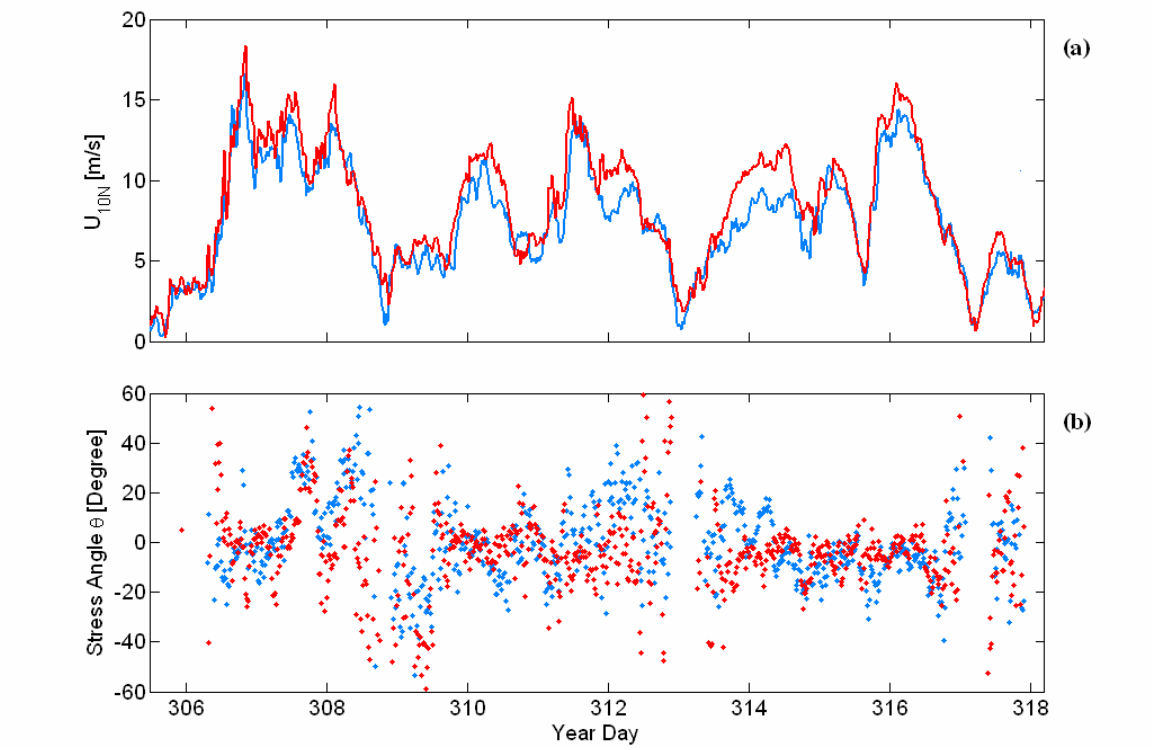

Figure 4.1: Wind speed (a), and wind stress angle with respect to the wind (b) during the SHOWEX experiment of 1999. Blue and red show data from the Bravo and Yankee buoys respectively. Wind stress angles are shown only for wind speeds over 4 m s^{-1}.

A significant cross-wind current speed U_{0Y} may affect both the stress magnitude and direction, in particular by, influencing or initiating a crosswind stress $(-\overline{v'w'})$. The cross-wind components of both stress and current are plotted in Figure 4.2, panels a and b respectively. To isolate the current effect, two cases between YD 305 to 318 were selected for further investigation. During the two cases, referred to as (1) and (2), the main influence on crosswind stress is the ocean current state: swell waves are either col-linear with the wind or weak, and the atmospheric stability is near neutral. Outside of these times, the crosswind stress, when present, may be under the effect of two or more factors. For example, during the periods from YD 306.35 - 307.25 and from YD 311.4 - 313.15, crosswind swells and currents were opposed. The relation between θ and U_{0Y} is plotted

in Figure 4.3 with special attention to the data from cases (1) and (2). Cases (1) and (2) represent two different phenomena and mechanisms of current effects on wind stress direction. For case (1), there is strong horizontal shear in the footprint of Bravo. The two peaks of cross-wind stress ($-\overline{v'w'}$) not only correlated to local current but more specifically to the current shear in the upwind direction (as discussed below). For case (2), the buoyancy current is relatively uniform across the domain, and strong. We found ($-\overline{v'w'}$) was steered about $10°$ away from mean wind direction even though the wind was strong during that time period. We next discuss each case in more detail.

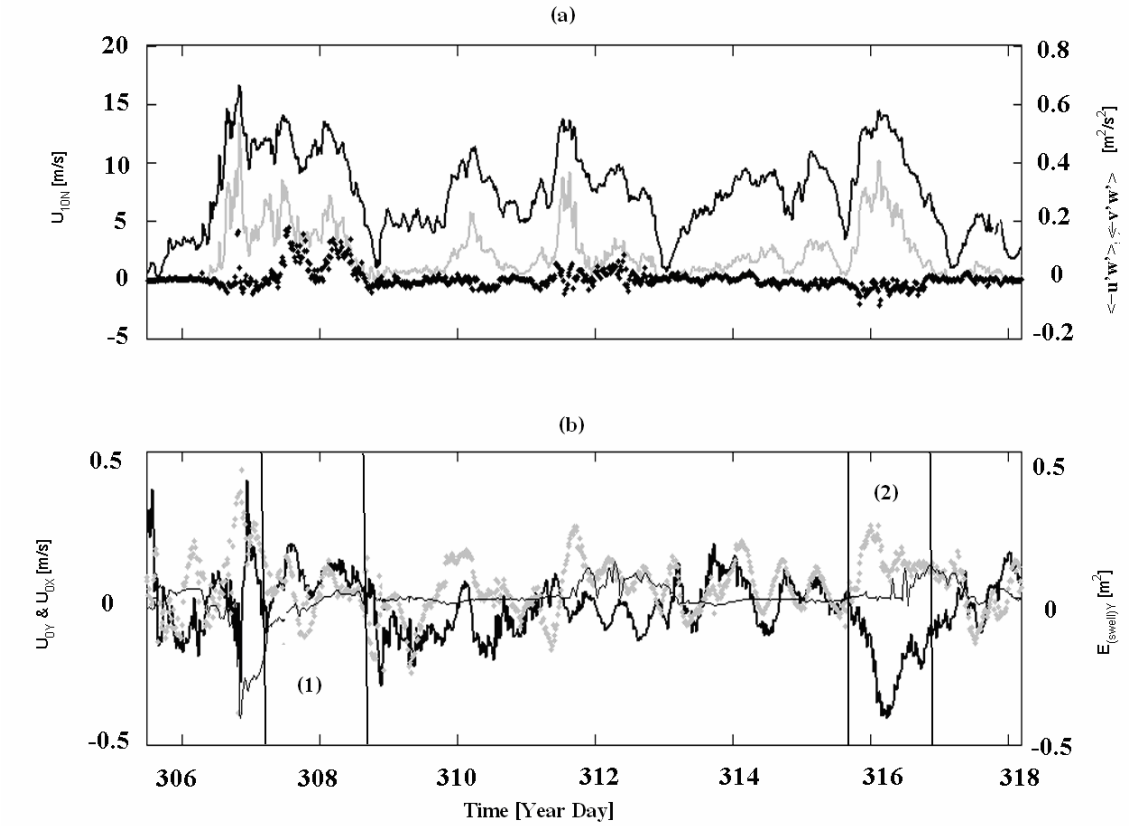

Figure 4.2: (a) shows the time series of 10m wind speed (black solid line) and along-wind wind stress (gray line) and cross-wind stress (black dot line) from Bravo during SHOWEX experiment. (b) Along-wind current speed (gray dot line), cross-wind current speed (black solid line) from OSCR at the location of Bravo, cross-wind swell wave energy (black dash line). Cases (1) and (2) show the cross-wind current effect on wind stress direction.

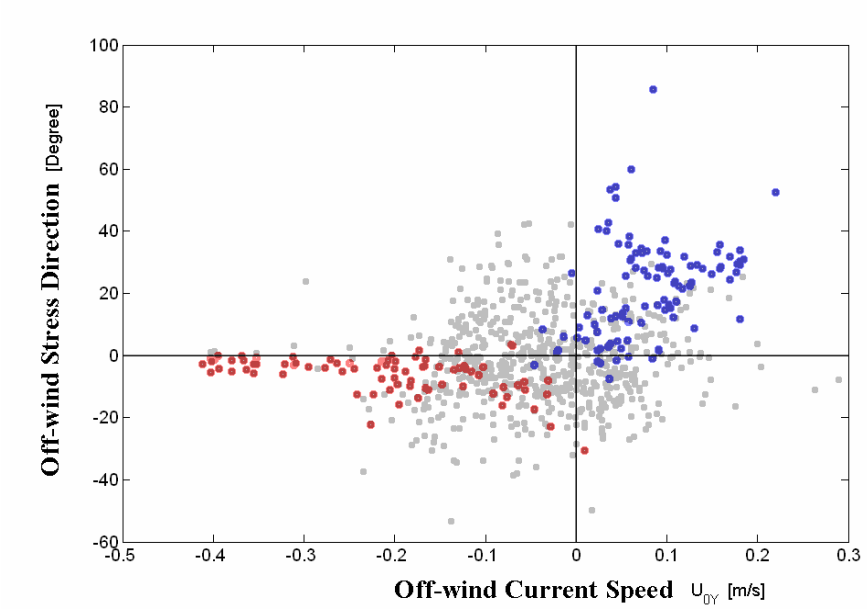

Figure 4.3: Off-wind stress angle plotted against the cross-wind current speed. The gray dots indicate all the data with wind speeds over 4 m/s during YD 305 to YD 318. The blue dots show case (1) and the red dots show case (2).

4.2 Shear current (Case 1)

On YD 306, the day prior to the case 1, a cold front associated with a nearby low pressure region passed through the area resulting in high winds, and a dramatic drop in air temperature over the SHOWEX domain (Fig. 3.4). Atmospheric stability (Figure 4.4f) remains close to neutral during case (1), due to the consistently high winds. Prior to the passage of the front, winds were over 10m/s from SSE, roughly shore parallel (Figure 4.4b), and the wave field was near full development with H_s (significant wave height) up to 3.5m (Figure 4.5, panels a and b). At this point, wind, waves, currents (weak, and primarily wind forced, 0.3 m/s) and wind stress were all close to co-linear (Figure 4.5b). As the depression passed to the north, the winds backed to the NW. For case (1) see Fig. 4.4d, the wind was blowing against the remnant swell (Figure 4.5e and f), which decayed quickly to O(0.5m) within 24 hours, i.e. by the end of case (1). Although swell waves dominated the sea state during case 1, they are not expected to influence the stress angle,

as the swell and wind were near co-linear. This was clearly not the case in the hours preceding case (1), when the wind and swell were nearly perpendicular (Figure 4.5, c, d). Despite this, the relative stress angle at this time was still small, possibly due to the additional effects of turning winds and surface currents. To simplify the analysis, case (1) starts 8 hours after the wind direction becomes NW, i.e. after the wind waves reach equilibrium.

The surface current from the OSCR cells closest to Bravo and Yankee are shown in Figure 4.4e. Although the surface currents during case (1) were typically small, there was a significant cross wind component U_{0Y}. In Figure 4.3, we plot relative stress angle versus U_{0Y} for the full 2-week period of Figure 4.2. The considerable scatter in the figure can be attributed to the various effects listed above, currents, swell waves, turning winds and stability. However, when the latter three effects were absent (as in case 1, distinguished by the blue dots), the stress angle was correlated with the cross-wind current with a correlation coefficient $\gamma = 0.68$. In Figure 4.6, we see the cross-wind current speed U_{0Y} and the cross wind stress, $(-\overline{v'w'})$ during period case (1). U_{0Y} peaked on YD 307.6 and 308.25 at almost the same time for two buoys . $(-\overline{v'w'})$ was at its maximum values during those two days for Bravo. $(-\overline{v'w'})$ at Yankee was a little weaker than at Bravo, but the two peaks are still clearly visible. During this time $(-\overline{v'w'})$ was much stronger than any other time period during SHOWEX; the relative direction θ also reached its maximum value (about $40°$ away from the mean wind direction) during case (1).

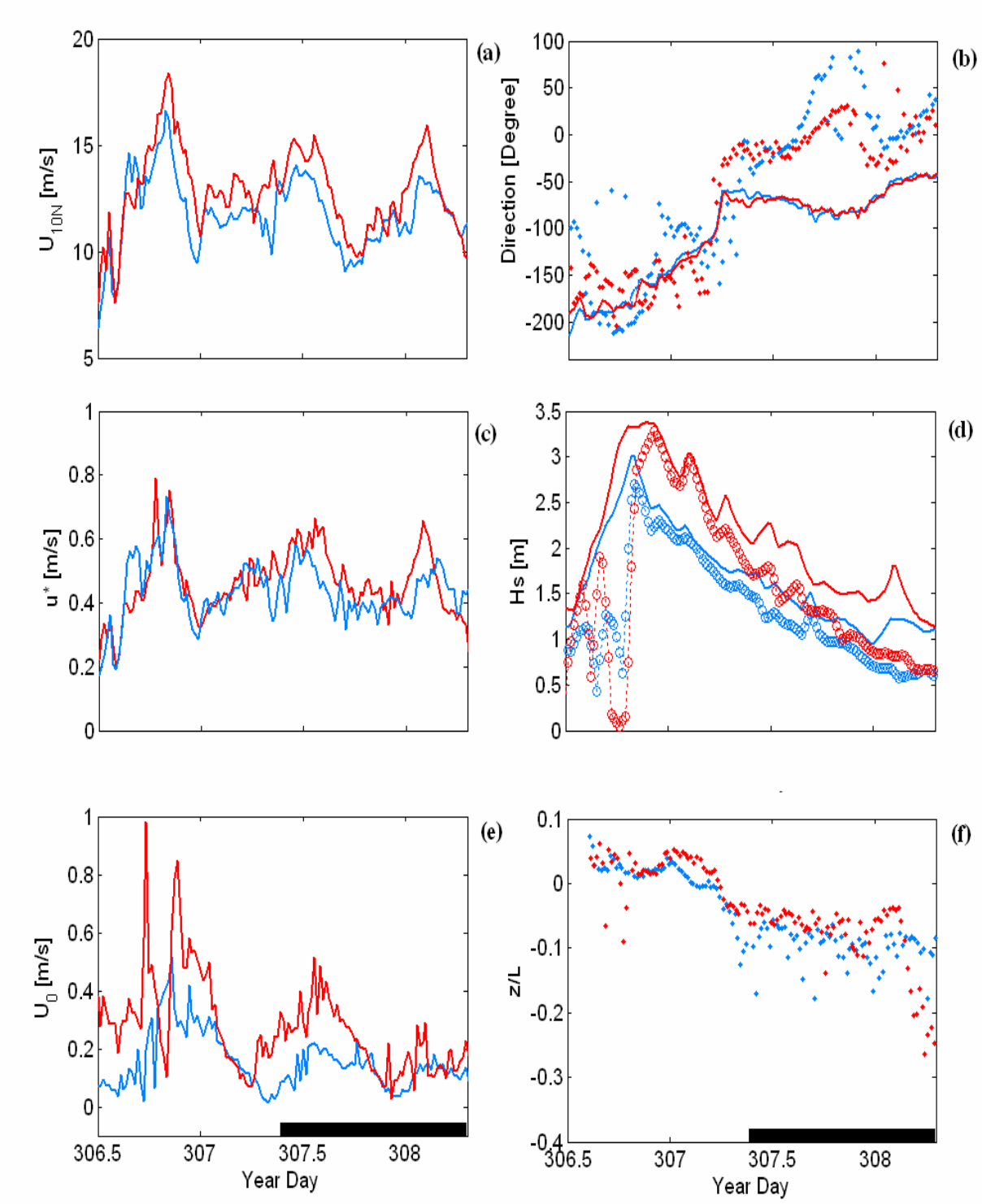

Figure 4.4: Data from Bravo (blue) and Yankee (red) buoys. The panels show: (a) wind speed; (b) wind direction (lines) and absolute current direction from OSCR (dots); (c) friction velocity; (d) significant wave height (lines), significant height for swell (circles); (e) surface current speed; (f) atmospheric stability during and preceding case 1.

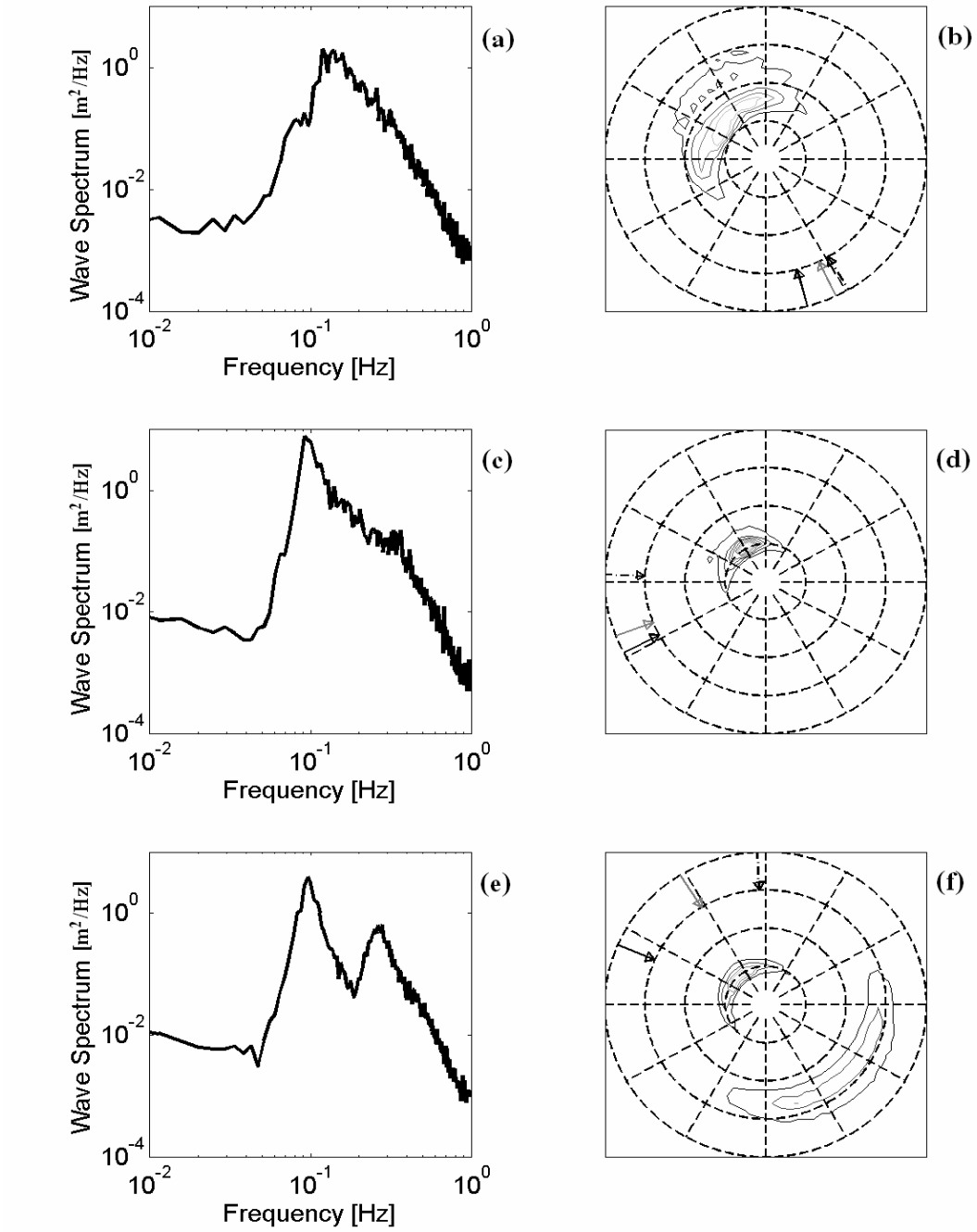

Figure 4.5 One dimensional (left panels) and two-dimensional (right panels) wave spectra at Bravo. Panels a and b are from YD 306, 1335-1542. Panels c and d are from YD 307, 0204-0410. Panels e and f are from YD307 1125-1331. The dashed circles in the 2D spectra denote frequencies 0.1, 0.2, 0.3 and 0.4 Hz. North and East are at the top and right of the plot, respectively. The three arrows show the wind direction (black), stress direction (grey) and current direction (dashed).

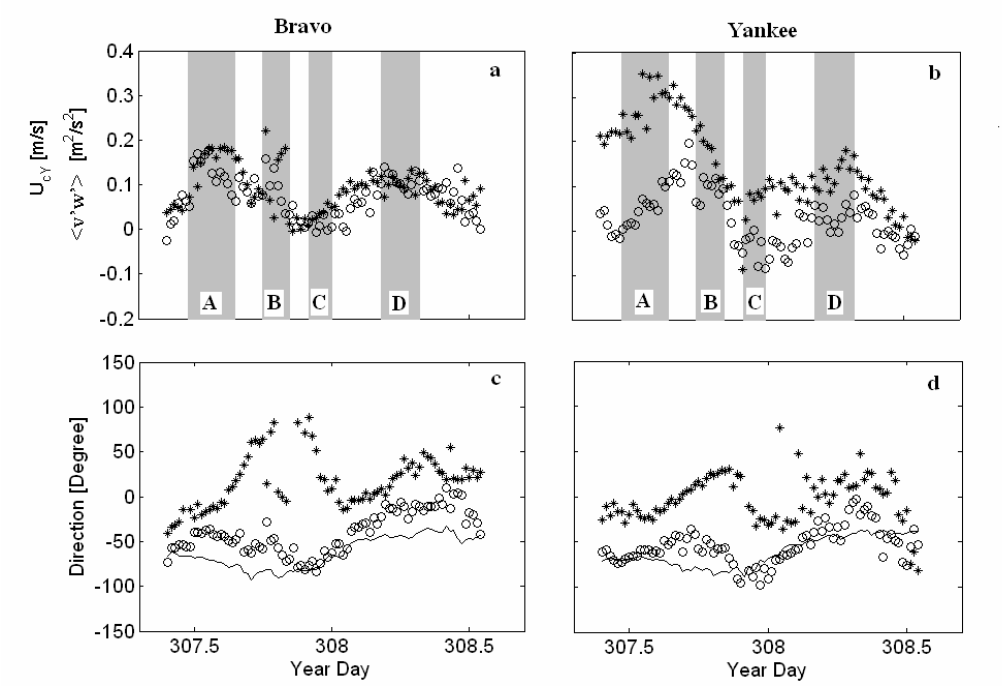

Figure 4.6: The off-wind current speed (star) and crosswind wind stress vectors (circle) at Bravo (panel a) and Yankee (Panel b) during case (1). (A), (B), (C) and (D) are four time periods identified in the text. Current direction (star), wind direction (solid line), and absolute wind stress direction (circle) are shown for Bravo and Yankee in panels c and d, respectively.

In Figure 4.6, four subperiods of case (1) are identified. Each period represents a 3 - 5 hour period; during which the ocean current was almost stationary. For period A, Bravo and Yankee were located at the edge and center, respectively, of a region of strong along-coast current (Figure 4.7a). The NW wind passed over a region of high lateral shear before reaching Bravo; the wind stress at Bravo was steered about 30° to the current direction. Meanwhile, the wind reaching Yankee was moving over a low-shear region; the wind stress direction was only steered about 10° from mean wind direction to the current direction. During period B, there were a strong current over the whole domain (Fig. 4.7b): the wind stress steering was similar (and large) at the two buoys.

During period C, the currents throughout the domain were weak. The current speeds at

the buoys and in the upwind direction were smaller than any other time in case (1), and the horizontal shear was also small. At both buoys, the wind and wind stress were aligned. During period D, Bravo was again downwind of a region of shear (Figure 4.7d). Although the current speed is less during period A, the upwind horizontal current shear is very clear. The wind stress steering was about $30°$. The other buoy, Yankee, was located in a more uniform current (Figure 4.7d). The horizontal current shear in the footprint of Yankee was weaker than Bravo. The wind stress shifting was less than what we found from Bravo.

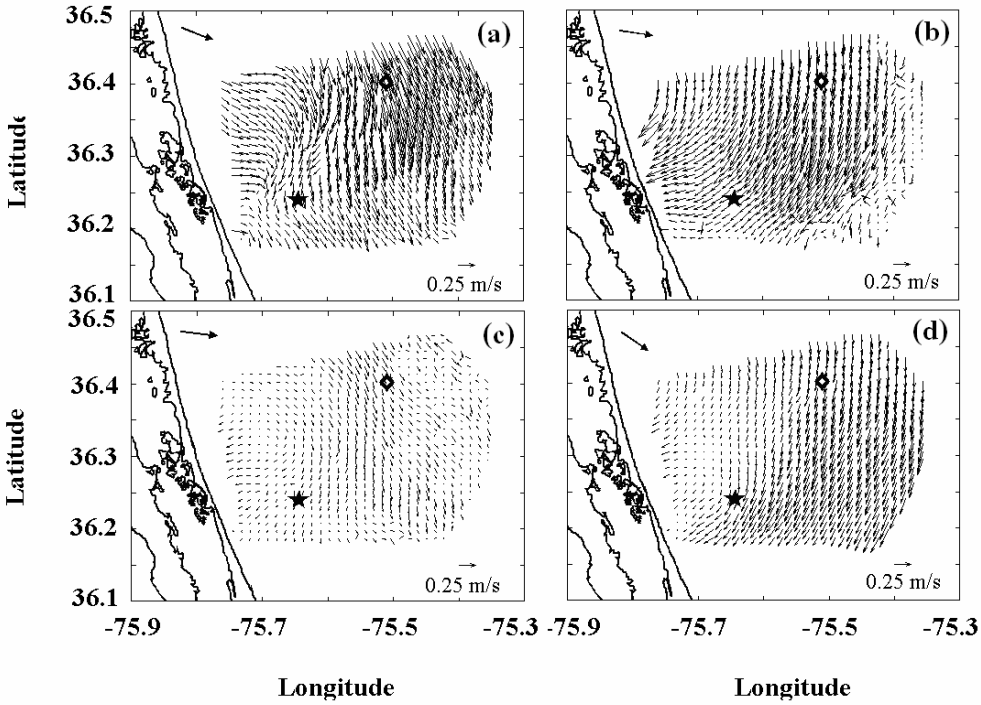

Figure 4.7: Current vector maps for four time periods during case 1 measured by OSCR. Panels (a),(b),(c) and (d) correspond to the periods indicated in Figure 4.6. The two ASIS buoys Bravo (star) and Yankee (◊) located in the scanning domain of OSCR are indicated. The arrow at the upper-left corner of each panel indicates the averaged wind direction.

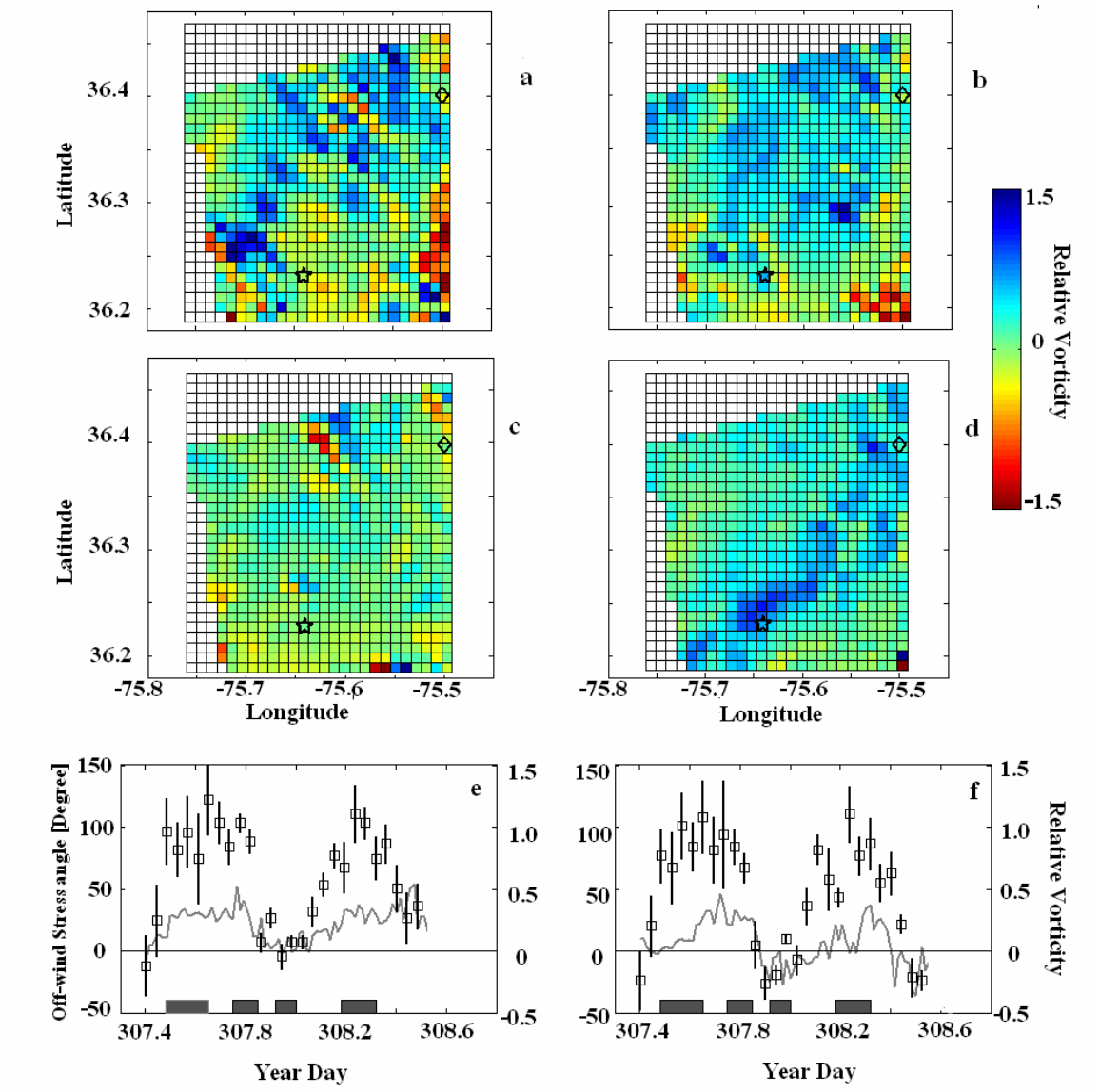

Figure 4.8: Panels (a),(b),(c) and (d) show relative vorticity (the ratio of observed vorticity to the local Coriolis parameter) maps for the corresponding panels in Figure 4.7. The data at the edge of OSCR is ignored. Panels (e) and (f) show time series of averaged upwind vorticity (squares, with error bars showing one standard deviation) and off-wind stress angle (line) for Bravo (e) and Yankee (f). The shaded areas in the bottom of each panel show the four periods of interest (as Figure 4.6).

From the above, we conclude that horizontal shear immediately upwind of the buoys (in the flux footprint) may be an important factor in influencing wind stress direction. We use the vorticity ($\omega = \frac{dU_{0Y}}{dx} - \frac{dU_{0X}}{dy}$) to quantify the horizontal shear. Each panel in

Figure 4.8 presents the surface current vorticity in the OSCR domain around the buoys. We pay extra attention to the vorticity in the upwind direction of Bravo and Yankee. For periods A and D, the wind sea waves passed the edge of a strong along-coast current to reach Bravo. The maximum vorticity is about $1.2f$ for A and $1.1f$ for D, where f is the local Coriolis parameter. The edge of the along-coast current can be seen clearly in Figs. 4.8a and 4.8d. The nonuniform current in period B has a relatively constant vorticity in the major part of the measurement area. We observe similar wind stress steering for Yankee and Bravo during period B. The vorticity during C, when currents were weak across the domain, is significantly lower than the other periods (Figure 4.8c). The corresponding wind stress was almost aligned with the mean wind.

To further investigate the correlation between vorticity and wind stress steering for two buoys, we average the vorticity from 10 (2X5) cells in the upwind direction (5 in the upwind direction; 2 in the crosswind direction). The results are shown in Figure 4.8e for Bravo and Fig. 4.8f for Yankee. The wind stress steering with upwind current vorticity from the two buoys indicates that the horizontal shear has an important influence on wind stress. The horizontal shear has a correlation coefficient $\gamma = 0.51$ with wind stress direction at Bravo. For periods A and D, Bravo and Yankee were just downwind of strong shear: the vorticity was high with large scatter. Period B shows high vorticity with much less scatter since the current meandering was relatively homogeneous for that time. All these periods with high upwind vorticity are with the strong wind stress steering. The significant correlation between wind stress deviation with upwind current vorticity at both buoys indicates that the horizontal shear has an important influence on wind stress.

To further understand the relation between current shear and wind stress steering, we

plot the cross wind current, U_{0Y}, for periods A and D in Figure 4.9. $\frac{dU_{0Y}}{dx}$ is the main source of vorticity during those two periods, with $\frac{dU_{0X}}{dy}$ making much less contribution but bringing significant noise to the vorticity map. From Figure 4.9b, Bravo and Yankee were right at the maximum gradient of U_{0Y} during period D: we observe a similar wind stress veering for the two ASIS buoys during this period. During period A, Bravo was behind (downwind) the edge of strong current. The strong shear affected the wind stress direction; the horizontal shear right at Yankee in the upwind direction was not strong (Figure 4.9a). The differences of wind stress steering at two locations support horizontal shear as the dominant factor affecting the wind stress direction in Case (1).

Wind stress is clearly related to the roughness elements on the sea surface, which are determined by the surface waves of all frequencies. Although there are few studies relating local current vorticity and wind stress, the relation between vorticity and wave refraction has a long history of research, much of it investigating waves propagating through a current field (Kenyon, 1971; Shay et al., 1996; Haus, 2007). The resulting refraction of the small scale waves ultimately causes the wind stress steering.

OSCR wave directions at peak spectral frequency (Wyatt et al., 2005) are shown in Figure 4.9a for period A. The available wave data cover a smaller area than ocean current data because the signal-to-noise requirements for processing wave height measurement are more restrictive than for currents. The peak wave directions are observed to change right after passing the strong horizontal shear (Figure 4.9a). These refracted wind sea waves lead to the wind stress steering. OSCR wave data was not available for other periods of interest.

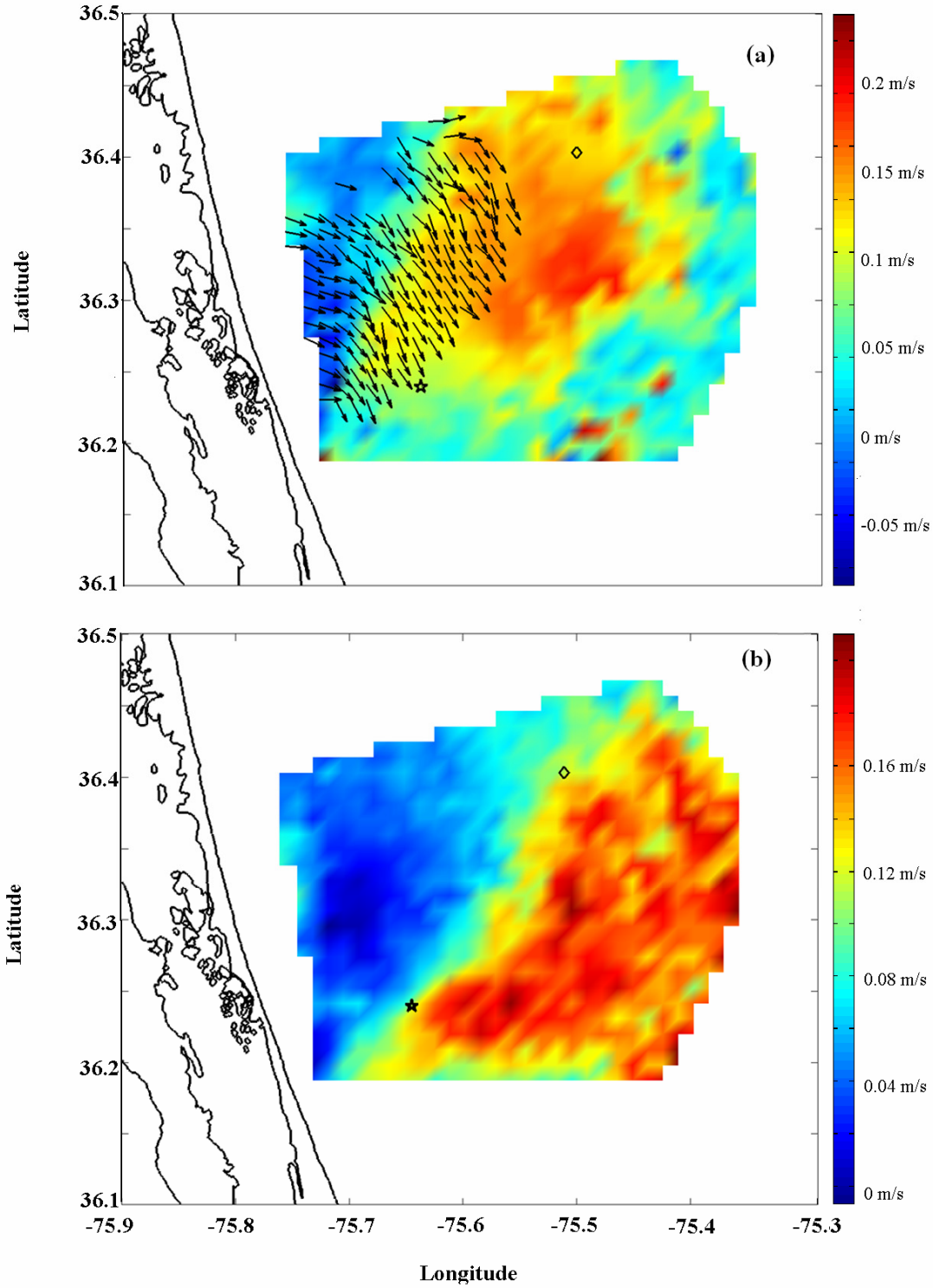

Figure 4.9: Cross-wind current speed (U_{0Y}) maps for periods A and D (panels a and b, respectively). The arrows in panel (a) are the wind sea wave directions measured from OSCR. The star and diamond symbols show the locations of the Bravo and Yankee buoys respectively.

The ASIS buoys provided high-resolution directional wave spectra for the frequencies up to 1 Hz. The wave data set from Bravo and Yankee were used to investigate the wave refraction associated with the horizontal shear and wind stress steering. For Bravo, the strong current shear was in the upwind direction for period A. The waves at frequencies above 0.5Hz generally were aligned with the mean wind direction, while wind sea waves at the spectral peak (0.25~0.3 Hz) were shifted $30^{\circ} \sim 40^{\circ}$ towards the current direction (Figure 4.10a). The corresponding wind stress direction was steered from the mean wind direction towards the current direction. At the same time, the spectra at Yankee (Figure 4.11a) were almost unaffected by the horizontal shear, since Yankee was too far from the strong along-coast current edge (Figure 4.9).

During period B, the current vorticity was relatively high in the entire experimental domain (Figure 4.8b); there was similar wave refraction for Bravo and Yankee (Figs. 4.10b, 4.11b). The waves in the peak frequency bands were refracted by the high vorticity shear associated with the curving current, but the high frequency waves, which are under the strong wind forcing, were still in the same direction with wind. The wind stress at both buoys was steered to the south by the refracted wind sea waves. Once the current and horizontal shear were very weak during C (Figure 4.8c), the directional wind wave spectra from both buoys showed no deviation from the wind direction in any frequency band (Figure 4.10c and 4.11c). The corresponding wind stress was close to the mean wind direction. Period D, when the current vorticity again became significant in the footprint of both buoys (Figure 4.8b), shows directional wave spectra and stress steering similar to period B (Figure 4.10d and 4.11d)

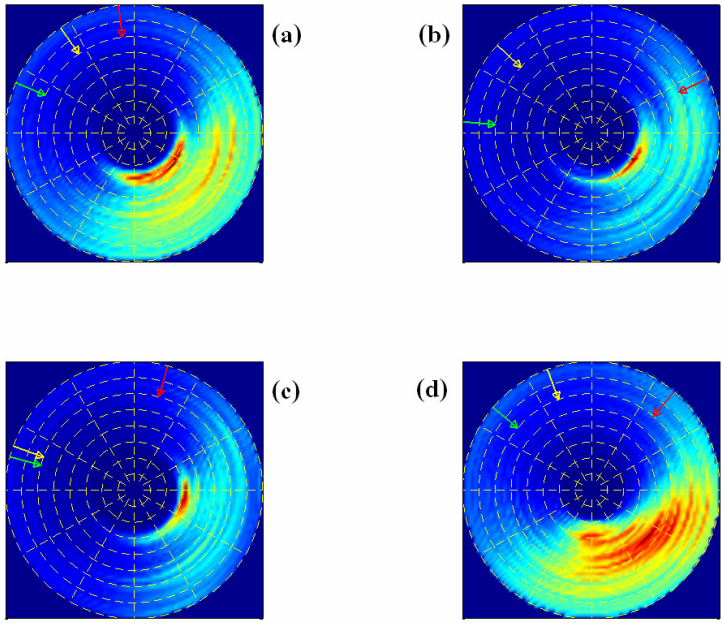

Figure 4.10: (a)-(d) show the averaged directional wave spectra ($\times f^2$) for Bravo at time periods (A)-(D) in figure 6. The dashed circles identify frequencies from 0.1Hz to 0.8Hz. North and east are at the top and right of each panel. The green arrow in each panel indicates the mean wind direction, the yellow arrow is the wind stress direction, and the red one means the current direction from OSCR right at the Bravo. In order to see the wind sea wave peak clearly, the wave spectra are multiplied by frequency squared.

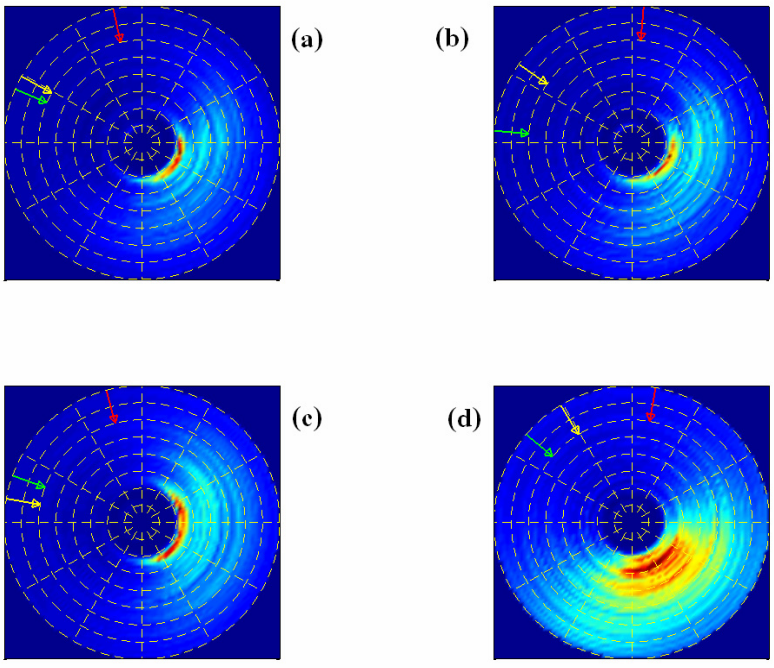

Figure 4.11: Same as Figure 4.10, but for Yankee.

Our hypothesis is that the effects we are observing, namely the shifting of the wind waves and thence wind stress away from the mean wind direction, is a result of the wind waves interacting with the surface current field. Recently, however, it was proposed that the turning of the wind waves at the SHOWEX site could be the result of the slanting fetch geometry (e.g. Donelan et al., 1985; Pettersson 2004), and not the currents (Ardhuin et al., 2007). Indeed, one of case studies used by Ardhuin et al. (2007) took place during our period A in Figure 6. They attribute the dominant wind-wave shifting to the slanting fetch effect and the results from the implementation of two wave models, "WAVEWATCH III" (Tolman and Chalikov 1996; Tolman 2002) and Coupled Rays with Eulerian Source Term (Ardhuin et al. 2001; Ardhuin and Herbers 2005) appear to support their conclusions, at least qualitatively. They do not include the effects of the current in either model.

While slanting fetch may indeed result in a wave spectrum qualitatively similar to that observed here (i.e. a turning of the peak wind waves, but not of the wind waves in the equilibrium range), several key aspects of our observations are not consistent with the slanting fetch mechanism. First of all, Fig. 9a shows a sharp gradient of the peak wave directions along the current front. The slanting fetch effect would predict gradual changes (relaxation of the peak waves back to the wind direction) with increasing fetch, with no significant change at the current front. Likewise, the slanting fetch effect can not explain the rapid changes in relative stress angle observed at both buoys (Figs. 8e and f). In particular, during period C, the stress angles at both buoys changed from roughly 30˚ away from the wind (period B) to near 0˚ (period C), before returning to 20˚ (D). As no concurrent shifts were seen in wind speed or direction (Fig. 3), the wave model of

Ardhuin et al. (2007) would predict very similar results for those three periods. Significantly though, these stress angle changes are mirrored in the relative current vorticity changes seen in Figs. 8e, f. Indeed, the negative vorticity at Yankee during C results in negative relative stress angles. Hence, while the slanting fetch effect may make some contribution to the observed wave spectra, the currents are clearly the dominant factor.

We now explore the mechanisms by which currents may affect the waves and wind stress. One hypothesis is that the wind stress turning is due to refraction of the surface waves on the sheared current (Kenyon 1971). Refraction could explain the shift in the energy-containing waves away from the wind direction, but the observations show that the short waves remain in the wind direction – contrary to what is predicted by the sheared current effect.

In the presence of horizontally sheared currents, wind generated waves are forced by both current shear and wind. Alpers and Hennings (1984) proposed a model to explain the wave patterns seen in satellite radar images. Starting from wave action conservation, and accounting for the relaxation time of surface waves, they showed that short gravity waves are prohibited from being shifted by current gradients, since the time scales of propagation across the gradient are much smaller than those associated with wind forcing of the slow-moving short waves. Kudryavtsev et al. (2005) recently presented a new radar imaging model of oceanic current features. They confirmed the Alpers and Hennings result that short waves are not affected by current shears, and also showed that the same is not true for the longer waves near the spectral peak. Indeed, the wind forcing time scales associated with these longer waves are much shorter, so that

shear current forcing is dominant. This effect is clearly seen in their Fig. 7c: waves near the spectral peak are significantly shifted in direction though interaction with the current shear; for the higher frequency equilibrium-range waves, the effect disappears. This model prediction is fully consistent with our interpretation that current shears are the key to understanding the observed changes in the wave spectrum, and thence of the stress direction.

4.3 Uniform Current (Case 2)

Case 2 provides a good example for the investigation of wind wave generation on a uniform current. Wave generation by wind has been the subject of many theoretical and experimental enquiries during the past several decades (Miles, 1960; Phillips, 1966). The studies include energy input from wind to wave, wave-wave interaction, wave-current interaction and wave energy dissipation on current. If the wind is perpendicular to a uniform current, it is not clear from known wind wave generation and wave-current interaction theory that wind-generated waves shall still be in the same direction with the wind. Will wave refraction happen under this situation? If positive, can the wind stress direction be affected? In the following, the SHOWEX data are used to study these problems.

During case 2, the wind and current were close to perpendicular to each other for about one day (Figure 4.12). The current and wind fields at Bravo and Yankee were very similar during this time. The atmospheric stability was near neutral throughout the domain. The current was relatively homogenous during case 2, with an average speed of 0.5~0.6 m/s.

Meanwhile, the wind direction from QuikSCAT is closer to the wind stress direction than the wind direction from ASIS buoys. The SeaWind on QuikSCAT measures the sea surface roughness from short waves with centimeter-scale wavelength. Panels a2 and b2 in Figure 4.12 show the wind direction inferred from short gravity waves by QuikSCAT propagated in the direction between mean wind and current.

The case provides a good example to investigate wind wave generation on a uniform current. In Figure 4.13, when the wind direction was almost stationary, and a strong along-shelf current dominated the whole experimental site. The vorticity in the upwind direction of Bravo and Yankee is weak (Fig. 4.13b). Therefore, current vorticity is not a factor to cause the wind stress or wind wave veering here. The averaged directional wave spectra for Bravo and Yankee are also very similar (Figure 4.13c, 4.13d). Under the condition of wind blowing across a strong uniform current, the high frequency bands (up to the 1 Hz maximum of the ASIS wave spectra) clearly turned toward current direction, but the wind sea wave peak at 0.2 Hz remained in the wind direction. This phenomena shows a good example of wind-wave generation on the cross-wind surface current, which are difficult to simulate in the wave tank. In order to study this case, we will use wave model to simulate wind wave generation on a current. The output will be compared with our observation in the next section.

In order to further study wind wave generation in the presence of uniform current condition, we use the SWAN model. SWAN is a third-generation wave model designed to overcome traditional difficulties of applying wave action in coastal regions. SWAN can describe the evolution of the two-dimensional wave energy spectrum in arbitrary conditions of wind and current. It assembles all relevant processes of generation,

dissipation, and nonlinear wave-wave interaction in a numerical code that is efficient for small scale, high-resolution applications. In our application, the wind speed 12 m/s and current speed is 1 m/s. In Figure 4.14, panel (a) shows the wave spectrum of the wind following the current; panel (b) shows the spectrum when the wind blowing against a current. Panel (c) and (d) shows the spectrum when the direction between wind and current is 45° and 135° . For the wind following current condition, the peak frequency shifts to a higher frequency because of the Doppler effect, and the energy-contained waves have higher energy. The equilibrium-range waves have a narrow spreading angle compared with the "no-current" condition. For wind against current condition, the peak frequency, wave energy and spreading angle have opposite results compared with spectra from wind following current case. The most significant difference is in the high frequency part. Wave action conservation theory predicts a cut off frequency $\omega_{c,\theta} = -g/4(U \cdot C) = 2.45 s^{-1}$, and wave energy at higher frequency band is zero. These phenomenons may be caused by waves above cut-off frequency breaking on the basis of wave action conservation. However, wave measurements from field or lab experiments do not show this characteristic. But in reality, the momentum flux from wind is still transferred to short waves, so short waves with frequencies above $\omega_{c,\theta}$ are always observed. The SWAN model generates incorrect results at these frequencies.

4.4 Discussion

Traditional studies about wave-current interaction assume the time and length scales of the current are much larger than the period and wavelength of the waves. The Doppler effect of surface waves in the current may explain some findings of the wave modulations

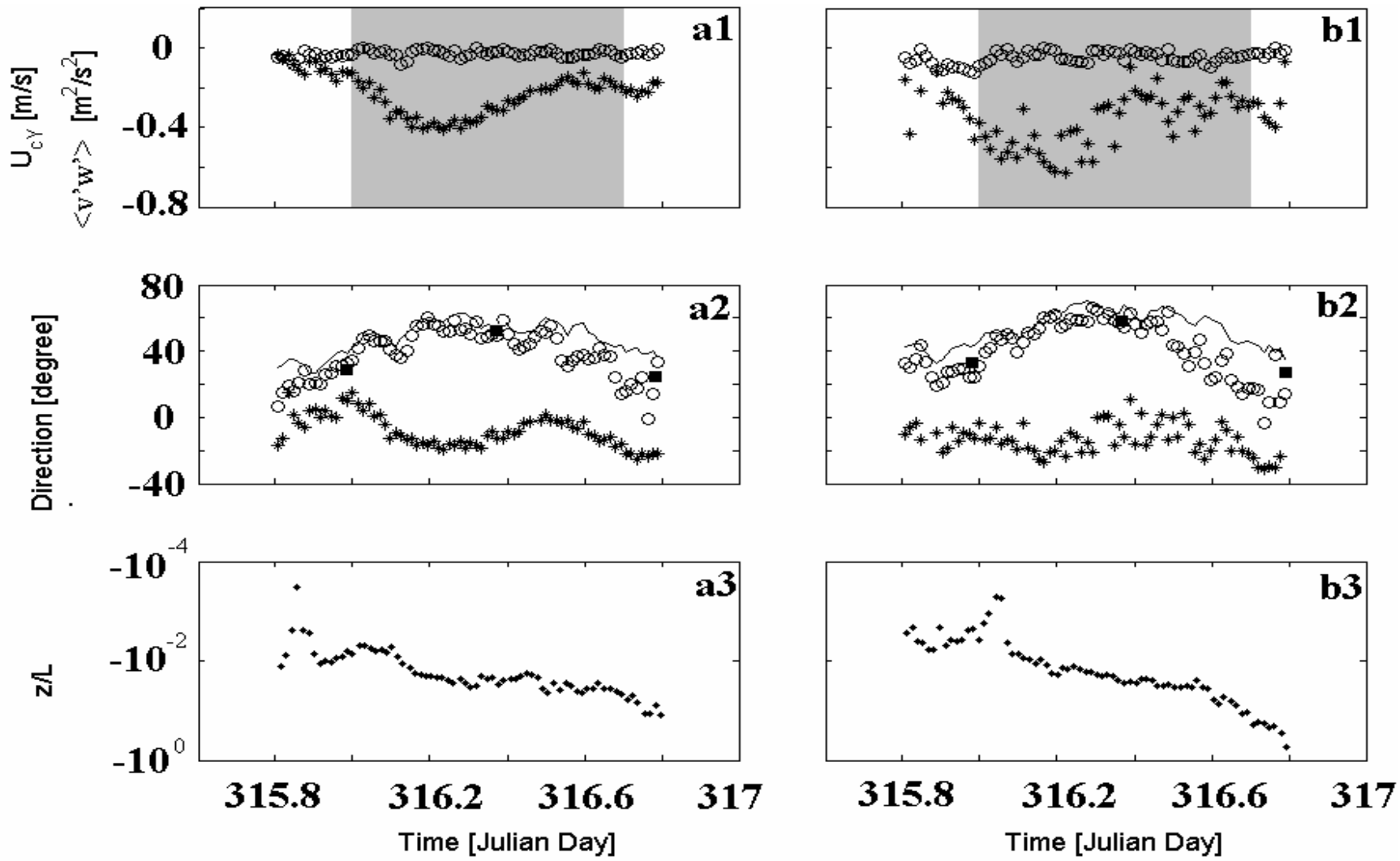

Figure 4.12: Data from case (2) in Figure 4.2. Panel (a1,b1) The Off-wind current speed (star) and crosswind wind stress vectors (circle). (a2,b2) Current direction (star), wind direction (solid line), and wind stress direction (circle), wind direction retrieved from QuikSCAT (square). (a3, b3) atmospheric stability . a1, a2 and a3 are the data from Bravo;b1, b2 and b3 are the data from Yankee

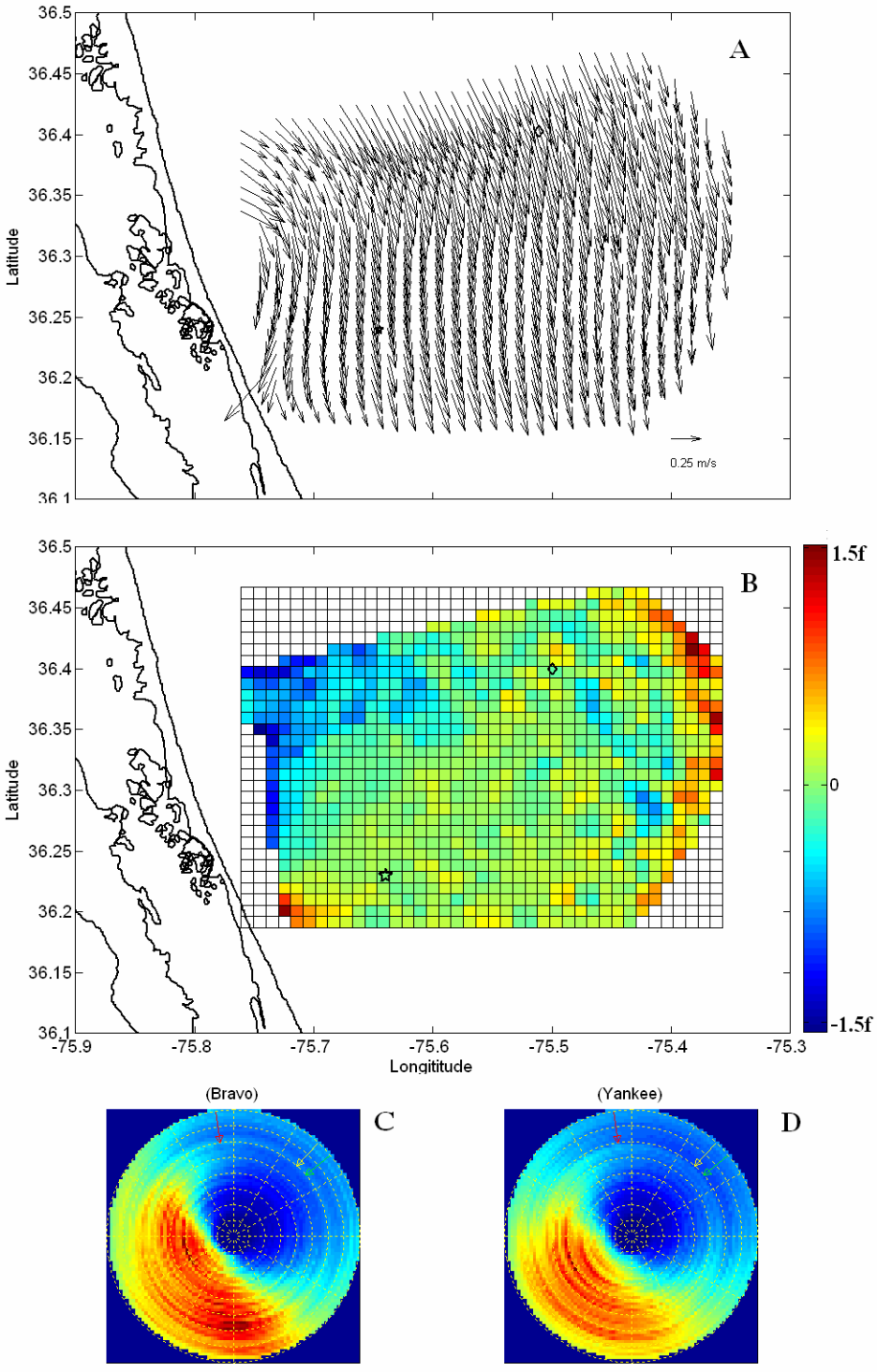

Figure 4.13: (A) The averaged current vector map for the case study. The star and diamond indicate the Bravo and Yankee. (B) The vorticity map for the corresponding panel (A). (C) the averaged directional wave spectra at Bravo. (D) The averaged directional wave spectra at Yankee. The green arrow in each panel indicates the mean wind direction, the yellow arrow is the wind stress direction, and the red one is the current direction from OSCR.

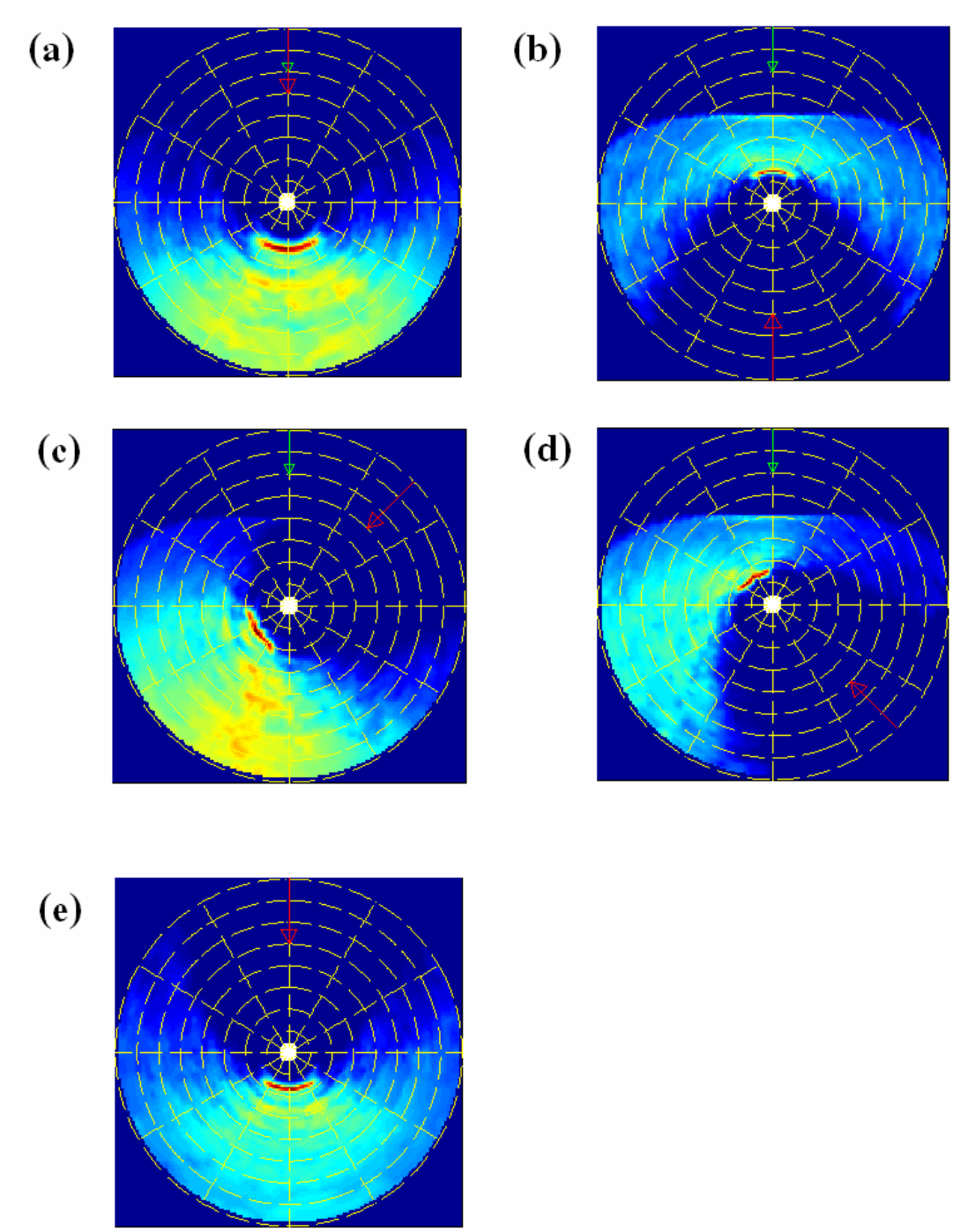

Figure 4.14: Wind wave spectra from SWAN model, wind speed 12 m/s and current speed 1 m/s. (a) Wind following current: wind direction and current direction at $0°$. (b) Wind against current: wind direction $180°$, current direction $0°$. (c) Wind crossing current: wind direction $45°$, current direction $0°$. (d) Wind crossing current: wind direction $135°$, current direction $0°$. (e) no current condition. Green arrows point to current direction, red arrows the wind direction.

by current variability. However, these considerations are on the basis that surface waves interacting with current are not under the forcing of wind, Current-wave interaction under wind forcing shows difference with the Doppler effect predicts. For example, Figure 4.11a shows the wave spectrum after the waves have propagated through a region of current shear. Comparing the wave direction on both sides of the current shear, the wave refraction of the energy-containing waves is well predicted by the Doppler effect. But by the same theory, the equilibrium-range waves should be refracted more by the current shear, because the faster (and longer) the surface waves, the smaller is the Doppler effect of surface current. This disagreement between reality and theory is clearly caused by the ignoring of wind forcing or other energy sources during application of the Doppler effect.

Another situation of invalidating the Doppler effect is wind-wave generation in the uniform current. For Figure 4.13, the current was almost temporally and spatially uniform, and the wind was stationary and crossing the uniform current. We observe no wave refraction for the energy-containing and equilibrium-range waves because of no current variability. The fact is the directional wave spectra from two ASIS buoys indicate the strong refraction for the equilibrium-range waves, and the refraction is stronger as the frequency increases. The energy-containing waves for that case are almost in the same direction as the mean wind.

Wind-wave refraction on a uniform current is also observed from scatterometer radar. Scatterometers measure microwave radar backscatter from centimeter-length waves on the ocean surface, which are generated by the wind forcing. An empirical retrieval algorithm is used to convert backscatter measurements into wind vectors (Wentz and Smith, 1999). The retrieval algorithm does not include the current effects on the

centimeter-length waves. Kelly et al. (2001, 2004) showed the systematic differences between winds measured by anemometer from a fixed point and scatterometer are due to ocean currents. Kelly et al. (2001, 2004) attributed the difference to the scatterometer measuring the motion of the air relative to the ocean. From their explanations, the centimeter-length waves are not in the absolute wind direction, but in the wind relative to current direction. This may agree with the equilibrium-range wave refraction under uniform current from Figure 4.14, but the energy-containing waves should be also in the direction of wind relative to current on the basis of their explanations, which is not true from our observation.

As above, the classical current-wave interaction theories present large differences in comparison with the findings in last section. A possible reason for the differences is the ignoring the wind impact on waves and wave dissipation when wind wave generation takes place on ocean currents. Although the current-wave theories were set up more then 50 years ago, adding the wave generation or dissipation parameters makes the problem become extremely difficult. Hence research on the wave generation or dissipation in the presence of current is sparse.

Kudryavtsev et al. (2005) focused on the divergence and convergence of small-scale waves by current variability, and also on their signatures in radar imaging. They did not consider the effect of uniform current on the short waves. For wind wave generation on uniform current, the relaxation time for the cross wind direction only has the wave breaking component (Since wave growth parameter only applies to the downwind direction). However, wave growth by wave breaking for the energy-containing waves is weak in comparison with equilibrium-range waves. Therefore, the relaxation time in the

cross wind direction for equilibrium-range waves is longer than energy-containing waves; wave refraction may happen more easily for equilibrium-range waves than energy-containing wave under uniform current. That could partly explain why only high frequency waves shift to current direction found by ASIS buoys as shown in Figure 4.12, 4.13.

The disagreement between wind directions from scatterometer and anemometer is probably caused by the difference between wind stress direction and mean wind direction. Liu et al. (2002) proposed that QuikSCAT measures the wind stress and not the mean wind near sea surface because the wind stress generates the ripples and waves to roughen the sea surface. We observe the wind direction retrieved from QuikSCAT to be closer to wind stress direction than the wind direction. The separation of mean wind and wind stress direction clearly correlates to the cross-wind current speed, which shifts the waves and stress to its direction. The shifting of waves is the direct medium to steer the wind stress. The modified wind stress then can affect the surface waves too. The interaction between wind, wind stress, waves and current makes radar backscatter respond more nearly to the stress. The mechanisms of this interaction and its effect to scatterometer measurement in the global scale are still under investigation

Since $\vec{\tau}_w$ corresponds to the waves in all frequency bands (though dominated by high frequency waves), the short gravity wave or dominant wave refraction caused by shear current or uniform current may modulate the surface stress. Once the waves are propagating in off-wind direction, the off-wind wave tends to drive the wind stress away from the mean wind direction, therefore cross wind stress ($-\overline{v'w'}$) becomes significant and the wind stress angle θ increases. On the other side, the cross wind stress may be one

parameter contributing to the off-wind surface waves. The whole process mentioned above is not a one-way interaction (*current* $\rightarrow$ *wave* $\rightarrow$ *wind stress*), but a more complex one such as (*current* $\leftrightarrow$ *wave* $\leftrightarrow$ *wind stress* $\leftrightarrow$ *current*). In the study of this process, we need consider the effects of breaking waves for both sides of air-sea interface. However, the detection and quantification of breaking waves in the open ocean is difficult. In the next Chapter, we will address this problem.

Chapter 5

Breaking Probability for Dominant Wave

5.1 Breaking Criteria

For most analyses of wave properties, we pay attention to global parameters, such as peak frequency and significant wave height. These global properties may give us general information about the wave field, but do not provide insight on when and where these quantities assume such values.

From a dynamical point of view, the information of local wave properties in real time is important for many problems of wave studies, such as deciding local breaking criteria. Yet, none of the traditional statistical methods employed to get global wave parameters have proven suitable for these investigations.

To detect breaking waves from temporal measurements, the Hilbert Transform has been applied (Melville, 1983; Huang et al. 1989; Griffin et al., 1996; Wu, 2002; Xu et al., 2000). Using measured surface elevation $\zeta(t)$ from a fixed point, we construct an analytical function $Z(t)$ with

$$Z(t) = \zeta(t) + i\xi(t) \tag{5.1}$$

where $\xi(t)$ is the Hilbert Transform of $\zeta(t)$, defined as

$$\xi(t) = \frac{P}{\pi} \int_{-\infty}^{+\infty} \frac{\zeta(t)}{\tau - t} d\tau \tag{5.2}$$

with P indicating the Cauchy principle value of integration evaluated at $\tau = t$.

The complex signal (5.1) can be expressed in the polar form as

$$Z(t) = a(t) e^{i\phi(t)} \tag{5.3}$$

where $a(t) = [\xi^2(t) + \zeta^2(t)]^{1/2}$ is the local wave amplitude. The phase function is

$$\phi(t) = \arctan[\frac{\xi(t)}{\zeta(t)}]. \tag{5.4}$$

By definition, the time derivative of the phase function is the local frequency

$$\sigma(t) = \frac{\partial \phi(t)}{\partial t} \ . \tag{5.5}$$

The local wave number is evaluated by the dispersion relation $k(t) = \sigma^2(t)/g$ for deep water, where g is gravitational acceleration.

The local phase velocity has the form

$$c(t) = \frac{\sigma(t)}{k(t)} \ . \tag{5.6}$$

Stokes (1880) and Melville (1983) showed that the phase velocity also had the form

$$c(t) = [g/\sigma(t)][1 + a^2(t)k^2(t)] \tag{5.7}$$

Although the above local parameter was derived for narrow-band processes, we still may get reasonably correct $c(t)$ from the above equation for ocean waves (Bitner-Aregerson and Gran, 1983). If linear wave theory is assumed, the local particle velocity is given by

$$u(t) = \frac{\partial \xi(t)}{\partial t} \tag{5.8}$$

$$w(t) = \frac{\partial \zeta(t)}{\partial t}$$

where $u(t)$ and $w(t)$ are the horizontal and vertical velocity components.

Melville (1996) questioned whether the application of the Hilbert Transform may cause errors in the results of local parameters, as the waves are not absolutely linear. Johannessen and Swan (2001) used Laser Doppler Anemometry (LDA) to measure water particle kinematics beneath a wave crest. They showed that wave directionality may dramatically reduce the difference between linear and second-order Stokes waves. Their results indicate that nonlinear wave modulations do not cause significant errors in the Hilbert Transform. Wu and Nepf (2002) show the difference between the linear wave assumption and wave tank measurements is less than 10%.

Given local wave parameters, two breaking criteria to detect wave breaking are used here:

(1) Geometric breaking criterion: This criterion is based on local geometry of the wave slope. Here we define breaking to occur when local inclination exceeds $30.37°$. Mathematically, $\frac{\partial \zeta}{\partial x} \geq \tan 30.37°$ (Longuet-Higgins and Fox, 1977). The surface inclination at a fixed point can be expressed as $\frac{1}{c(t)} \frac{\partial \zeta(t)}{\partial t}$ (Longuet-Higgins and Smith, 1983). Then the geometric breaking criterion has the form $\frac{1}{c(t)} \frac{\partial \zeta(t)}{\partial t} > \tan 30.37°$. Huang et al (1989) applied this criterion for detecting wind-wave breaking in the wave tank, and showed this criterion to be

suitable for identifying wave breaking in the laboratory. Xu et al. (2000) further applied the same criterion to wave data from an oil platform. The simultaneous visual observation of breaking waves indicated good agreement with the results using the geometric breaking criterion. Besides the local wave slope, other geometric parameters including the local wave steepness and symmetry are potential candidates to detect wave breaking. However previous analyses about these are very sparse. Although we will not address local wave steepness and symmetry in detail, the qualitative analysis between the different geometric parameters will be done when checking the validity of the breaking criterion $\frac{1}{c(t)}\frac{\partial \zeta(t)}{\partial t} > \tan 30.37°$ in the ocean with complex current conditions.

(2) Kinematic breaking criterion: The most common kinematic breaking criterion is the ratio of the local horizontal velocity $u(t)$ at the wave crest to the local wave speed $c(t)$. This criterion predicts wave breaking will occur if the ratio is greater than unity (Longuet-Higgins, 1969; Tulin and Li, 1992). The self-evident property of this criterion has drawn interest in recent laboratory studies (Huang et al. 1989; Wu and Nepf, 2002). However, other laboratory results show $\frac{u(t)}{c(t)} \geq 1$ is not a good standard for detecting wave breaking (Perlin et al. 1996; Chang and Liu, 1998; Stansell and Macfarlane, 2002; Oh et al. 2005). Even if their conclusions may not support the application of breaking kinematic criterion direction, the comparisons in the above articles show $\frac{u(t)}{c(t)}$ for breaking waves is still higher

than non-breaking waves. Therefore, we may still detect breaking waves by modifying the threshold value in the experiments.

5.2 Dominant Wave Breaking

The physical complexity of breaking waves leads to different results for similar experiments. In addition, the specific method or instrument used to calculate $u(t)$ and $c(t)$ affects the threshold of the kinematic breaking criterion. Huang et al. (1989) and Wu and Nepf (2002) assumed the waves in the laboratory are linear waves, and then applied the Hilbert Transform to calculate the local wave parameters. They concluded the kinematic breaking criterion with $\frac{u(t)}{c(t)} \geq 1$ is a robust and effective indicator for wave breaking even if the linear wave assumption is questioned by Melville (1996). She et al. (1997) showed the linear wave assumption may underestimate both $u(t)$ and $c(t)$ up to 20%, but $\frac{u(t)}{c(t)}$ is still close to the actual value. Qian and Duncan (2001) applied a nonlinear estimator to wave information from Particle Image Velocimetry (PIV), and confirmed that the critical value of breaking onset is consistent with theory. The breaking detection method by Huang et al. (1989) and Wu and Nepf (2002) may be applied to field experiments if high-resolution surface elevation data is available.

Perlin et al. (1996) used Particle Image Velocimetry (PIV) and Particle Tracking Velocimetry (PTV) to measure the particle velocity near the crest during plunging events. They found $MAX[\frac{u(t)}{c(t)}] \approx 1.3$ in the ejecting jet of the overturning waves. Chang and Liu

(1998) used $c(t)$ calculated from non-linear theory and $u(t)$ directly from PIV. They found $MAX[\frac{u(t)}{c(t)}] \approx 1.07$ during wave breaking. Wu and Nepf (2002) and Chang and Liu (1998) cannot provide direct evidence to support the kinematic breaking criterion, but their studies indicate $\frac{u(t)}{c(t)}$ at the onset of wave breaking is higher than unity from their measurements.

Stansell and Macfarlane (2002) used PIV to measure $u(t)$ and calculated $c(t)$ from surface elevation data by wave gauges. They avoided the linear approximation when estimating $u(t)$ and $c(t)$ at the crests, and observed $\frac{u(t)}{c(t)} < 1$ during breaking events. Although they drew the conclusion that $\frac{u(t)}{c(t)} \geq 1$ is not a good indicator for wave breaking, all waves with $\frac{u(t)}{c(t)} \geq 0.72$ were breaking in their analysis. Hence if the threshold of $\frac{u(t)}{c(t)}$ is lowered to 0.72, a kinematic breaking criterion may still work. Stansell and Macfarlane's observation is a conflict with the other studies cited above. Where does the difference come from? One possible answer is the sampling frequency. They used a wave gauge with 36 Hz sampling frequency to measure $c(t)$; this frequency is significantly lower than other experiments' sample rate. Wu and Nepf (2002) record their wave gauge signal at a 200 Hz frequency. Huang et al. (1989) digitized the wave gauge data at a rate of 128 samples/s to preserve the properties of surface jump. Perlin et al. (1996) set up the sampling at 125 Hz for PTV and even higher for PIV. These

analyses indicate the sampling frequency may be a factor for the threshold of breaking criteria, and may further affect the final results of breaking probability.

In Figure 5.1, we use data from the Air Sea Interaction Salt Water Tank at the University of Miami to test the sampling frequency effect on the breaking criteria. Surface elevation data were measured by Multiple Laser Elevation Gauges at a sampling frequency of 2000 Hz. We collected two groups of wave displacement data under different wind conditions (1) U=14.23m/s and (2) U=4.72m/s at 22 cm above the surface. Through visual observations, almost all dominant waves from (1) break; and no dominant wave breaking is found from (2). We applied the breaking kinematic and geometric criteria to the data; and then collect $MAX[\frac{u(t)}{c(t)}]$ and $MAX[\frac{1}{c(t)}\frac{\partial\zeta(t)}{\partial t}]$ at each dominant wave crest. The surface displacement measurements were sampled at 2000 Hz, so we can easily infer the low sampling frequency (1000, 500, 400, 200 and 100Hz) data from the original measurements.

The mean value of $MAX[\frac{u(t)}{c(t)}]$ and $MAX[\frac{1}{c(t)}\frac{\partial\zeta(t)}{\partial t}]$ with standard error bar under multiple sampling frequencies are presented in Figure 5.1a and 5.1b. From the results, we can find first that $MAX[\frac{u(t)}{c(t)}]$ and $MAX[\frac{1}{c(t)}\frac{\partial\zeta(t)}{\partial t}]$ decrease with sampling frequency no matter the wind speed. Secondly, for sampling frequency higher than a certain value, the theoretical breaking criteria still can be used to detect the breaking waves. However for lower sampling frequencies, a new breaking criterion threshold can be determined. These results indicate we can add a coefficient to the breaking criteria to apply them to data with lower sampling rates.

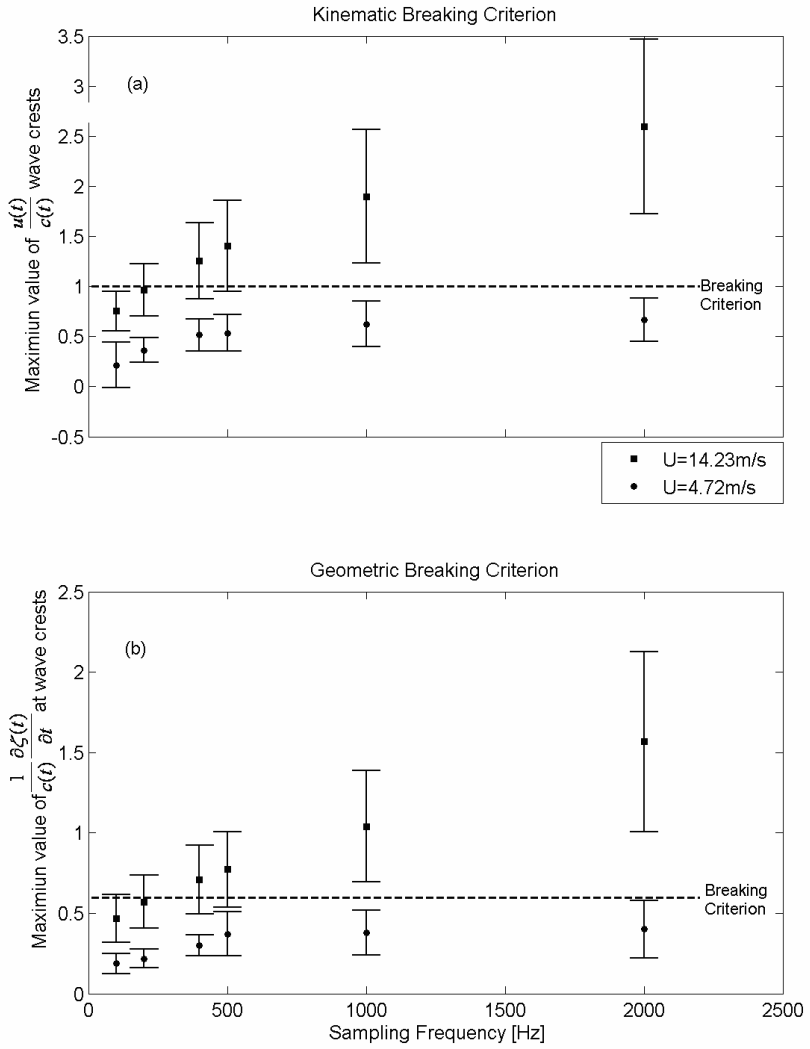

Figure 5.1. The average maximum value of breaking criterion formulations in the laboratory under various sampling frequencies. (a)breaking kinematic equation $\frac{u(t)}{c(t)}$ (b) breaking geometric criterion $\frac{1}{c(t)}\frac{\partial\zeta(t)}{\partial t}$. The dashed lines are the breaking criteria used to determine the breaking waves. Solid squares are the mean value of maximum values of $\frac{u(t)}{c(t)}$ or $\frac{1}{c(t)}\frac{\partial\zeta(t)}{\partial t}$ at wave crests for a wind speed of U=14.23 m/s (almost all dominant waves break under this condition); Solid circles are the mean value of maximum values of $\frac{u(t)}{c(t)}$ or $\frac{1}{c(t)}\frac{\partial\zeta(t)}{\partial t}$ at wave crests for measurements at wind speed U=4.72 m/s (almost no dominant waves break under this condition). The bars show the one standard error from the mean values.

Considering the data storage ability on the ASIS buoy, we used 20 Hz sampling frequency to collect surface elevation data for most deployments. It is adequate for most applications, but we must overcome the low sampling frequency effect before applying the data to the breaking wave detection. We have known the successful applications of kinematic breaking criterion with lower thresholds in the wave tank associated with a sampling frequency higher than 100 Hz. In the field experiment with ASIS buoys, although we did not have direct observations of breaking waves, the breaking threshold 20Hz for low sampling frequency may be estimated on the basis of the known breaking properties and previous measurements.

The time scale of breaking ΔT_b found by Huang et al. (1989) has the relation of $\Delta T_b / T_b \approx 0.05$, where T_b is the period of breaking wave. Since the dominant wind wave frequency is 0.3 Hz or even lower for our field experiments, we can calculate $\Delta T_b \approx 150ms$, which means the sampling interval 50 ms can detect the breaking event for dominant waves ,but may miss some information at the peak. Therefore the breaking criteria for the data from ASIS have a lower threshold value than theory.

We illustrate this problem using ASIS data in Figure 5.2. Since our data are sampled 20 Hz, we can easily subsample the surface elevation time series to a sampling frequency of 10 Hz. The Figure shows clearly the $\frac{u(t)}{c(t)}$ and $\frac{1}{c(t)}\frac{\partial \zeta(t)}{\partial t}$ for 10 Hz has lower values than 20 Hz data at the dominant wave crests. Combining the sampling frequency analysis from the wave tank and ASIS, it is reasonable for us to choose a coefficient ε_w ($\varepsilon_w < 1$). The modified breaking kinematic and dynamic criteria are:

$$\frac{1}{c(t)}\frac{\partial \zeta(t)}{\partial t} > (\tan 30.37°)\varepsilon_w \text{ and } \frac{u(t)}{c(t)} > \varepsilon_w \tag{5.9}$$

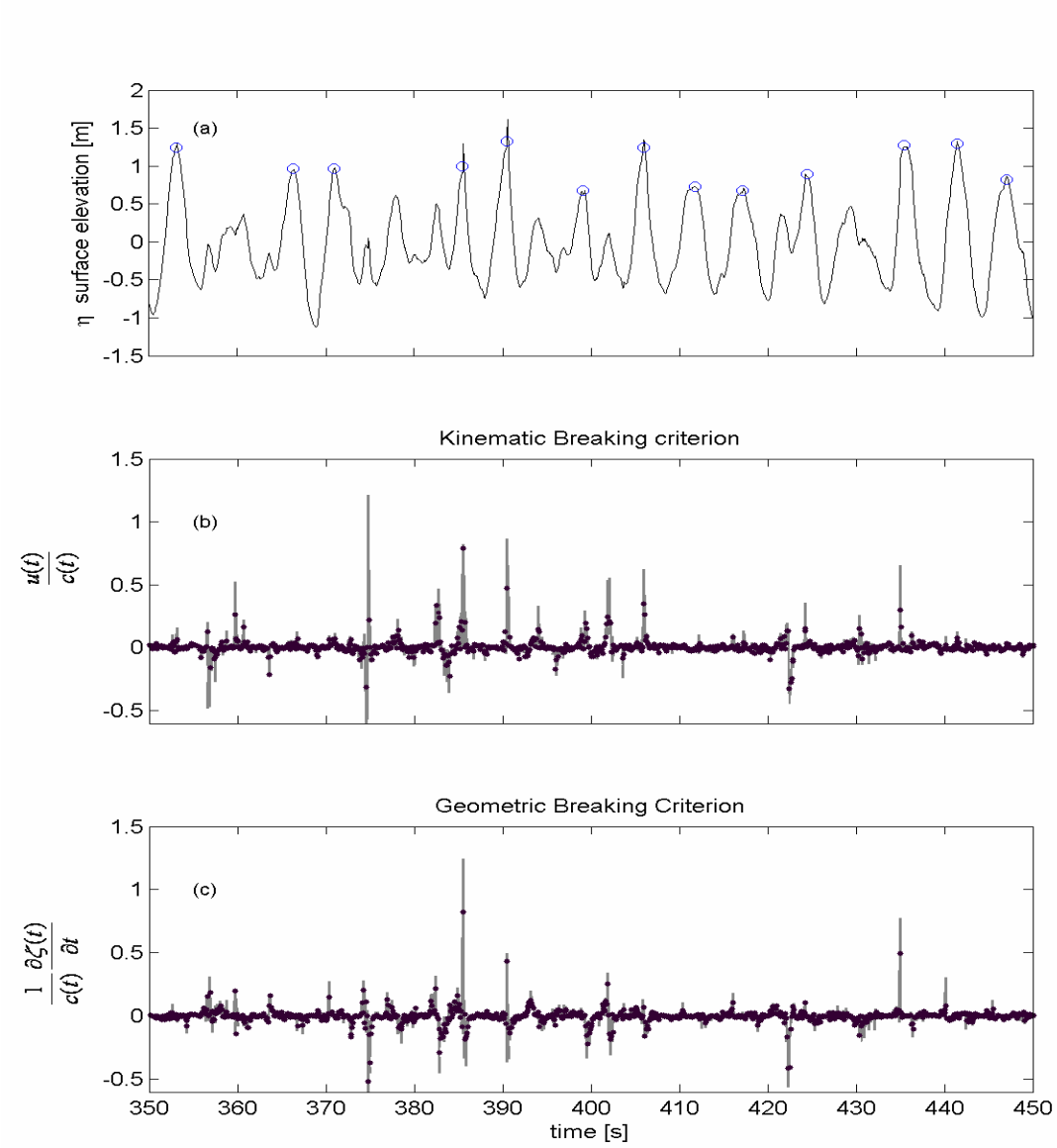

Figure 5.2: Sample field data. Time series of (a) surface elevation η, the wave crests with a circle are the dominant waves for the breaking wave statistics; (b) Kinematic breaking criterion, $\frac{u(t)}{c(t)}$;(c) geometric breaking criterion $\frac{1}{c(t)}\frac{\partial \zeta(t)}{\partial t}$. In panels (b) and (c) the black line is for 20 Hz sampling frequency, and the dot for 10 Hz

We present time series of surface elevation, $\frac{u(t)}{c(t)}$ and $\frac{1}{c(t)}\frac{\partial\zeta(t)}{\partial t}$ from Yankee buoy as an example. The time series is from at 15 Nov., 1999 when $U_{10N} \approx 18 m/s$. Figure 5.3a shows two groups of waves passing the Yankee buoy during a 200s period. The breaking events occur when of $\frac{u(t)}{c(t)}$ and $\frac{1}{c(t)}\frac{\partial\zeta(t)}{\partial t}$ exceed the threshold values, which are decided by equation 5.9.

For every buoy, we choose five wave gauges to detect breaking dominant waves. (a wave is classified as dominant wave when $f < 2f_P$). At each wave crest, if three or more gauges report the local wave parameter ratio exceeding the threshold value, then a breaking event is confirmed. As the distances between wave gauges are close to 1 m, the detected breaking scale has an order of 1 m. To count the total dominant wave crests (N_s) passing the wave gauge, we use the up-crossing method to locate wave crests and troughs We count the wave crests during 30 minutes. The period (T) of the single wave is decided by the time difference of wave troughs on both sides of the wave crest. The frequency of the single wave is $F_w = 1/T_w$. Here, the breaking probability for the dominant wave (P) is defined as the ratio of total breaking events (N_b) to total dominant waves (N_s) passing ASIS during 30 minutes.

$$P = N_b / N_s \times 100\% \quad (5.10)$$

If only one wave gauge reports a breaking event at some crest, it is very possible that the event is microbreaking event or just noise. Our statistics simply exclude this and focus on the dominant wave breaking. Because our results of breaking wave detection, if successful, shall be comparable with the previous breaking wave studies, we can infer the

value of ε_w from the known relationship breaking waves. From Figure 5.3b and 5.3c, the highest spikes, which very possibly represent the breaking waves at this wind and sea state condition, are usually found in the middle of wave groups. This finding is consistent with the observations of consecutive wave breaking in a series of wave packet (Donelan et al. 1972). This simple comparison of sample time series presents the promising results of breaking wave results. The key for applying the breaking criteria is to find out the correct ε_w for our data. Here we choose ε_w to match the results of earlier studies. We choose our ε_w to give the greatest agreement with the results of earlier studies.

Holthuijsen and Herbers (1986) compared the relation between the breaking probability and U_{10} from five different field experiments. That figure in Holthuijsen and Herbers (1986) is reproduced in Figure 5.4. Toba et al. (1971) and Holthuijsen and Herber (1986) used similar techniques to count breaking waves at all wave lengths. They coupled the visual identification of white capping with wave height measurements. Thorpe and Humphries (1980) used the telephotography in place of direct visual observation, and Longuet-Higgins and Smith (1983) employed a 'jump meter' to detect a breaking event of dominant waves. Both methods could miss counting the small scale breaking in contrast to the method from Humphries (1980). As such, the observed number of breaking waves should be less in the latter two cases.

In Figure 5.4, we assume $\varepsilon_w = 0.4$,0.5 and 0.6, and apply the kinematic breaking criterion $\frac{u(t)}{c(t)} > \varepsilon$ to all three buoy data sets in the SHOWEX experiment. From

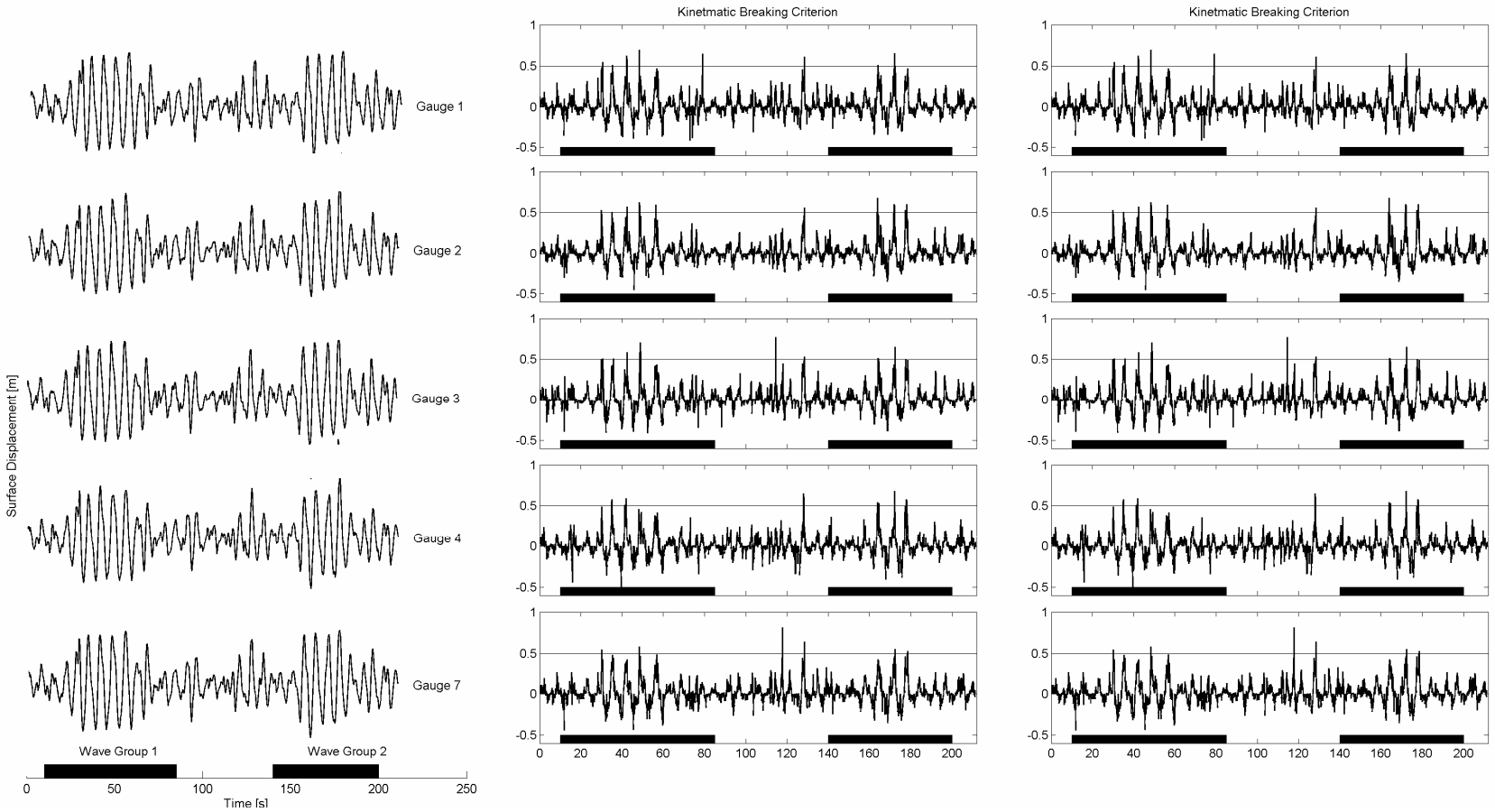

Figure 5.3. Sample data. Time series of (left) surface elevation η, (middle) breaking variable $\frac{u(t)}{c(t)}$, (right) breaking variable $\frac{\partial \zeta(t)}{\partial x}$ approximated by $\frac{1}{c(t)}\frac{\partial \zeta(t)}{\partial t}$. (a), (b) and (c) include the data from five wave gauges at Yankee during SHOWEX experiment. The gray lines in (b) and (c) indicate the breaking criteria with $\varepsilon = 0.5$.

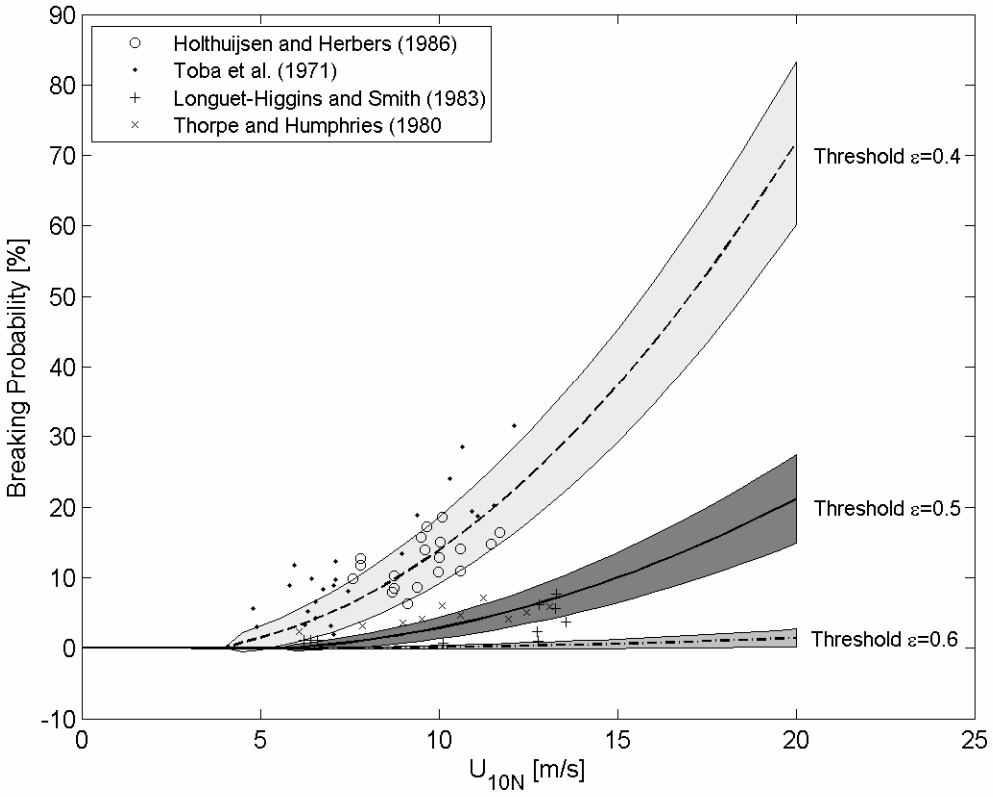

Figure 5.4. Breaking probability as a function of mean wind speed for $\varepsilon = 0.4$ (dashed), $\varepsilon = 0.5$ (solid) and $\varepsilon = 0.6$ (dashed-dotted). The shaded areas denote ± 1 standard error from the mean curves. The symbols represent data from four previous articles.

the relations between the breaking probability to the mean wind speed under three threshold values, $\varepsilon_w = 0.6$ is clearly too high to pick up breaking waves: the breaking probability is so low that P is close to zero even when $U_{10N} > 18 m/s$. This is not true as shown by Melville and Matusov (2001) who reported clear evidence of breaking of dominatant waves at $U_{10} > 7.2 m/s$ from the aircraft images in SHOWEX experiment. The relation of breaking probability vs U_{10N} from $\varepsilon = 0.4$ shows similar results to Holthuijsen and Herber (1986) and Toba et al. (1971). However, our detection method is

designed to find the breaking events only for dominant waves, hence the breaking probability should be lower than those for all scale breaking waves as Holthuijsen and Herber (1986) and Toba et al. (1971). The breaking probability from $\varepsilon = 0.5$ presents agreement with Thorpe and Humphries (1980) and Longuet-Higgins and Smith (1983)'s results for the large scale breaking events.

The above comparisons provide a quantitive estimate of the threshold value, but we need validate it with other data set. Katsaros and Atakturk (1992) used continuous video records of breaking events at their wave wires on Lake Washington. They attempted to establish a connection between breaking probability for dominant waves (microscale breaking is excluded from their analysis) and various atmospheric forcing parameters. They found the best correlation with $\gamma_c = 0.81$ for the following fit to their data:

$$P_b = -2.47 + 32.87u_*^2 + 42.37\frac{u_*}{C_p} \tag{5.11}$$

where u_* is the friction velocity and C_p is the wave phase velocity at peak frequency; $\frac{u_*}{C_p}$ is inverse wave age. In this model, they not only considered the wind forcing (u_*^2), but also reflected the stage of wave development ($\frac{u_*}{C_p}$).

In the SHOWEX experiment, three ASIS buoys measured u_* by the eddy-correlation method as discussed in Chapter 3; C_p can be inferred from the measured wave data. We calculate the wave breaking probability on the basis of the model from Katsaros and Atakturk (1992).

The measured breaking probability from certain buoys shows good agreement with the modeled results. The correlations are $\gamma_c = 0.64$ for Bravo and $\gamma_c = 0.76$ for Yankee in SHOWEX experiment and $\gamma_c = 0.78$ for the BASE experiment. Considering that the model is based on the reliable visual identification of wave breaking, the correlations show the detection of breaking by ASIS is very promising. The modeled the breaking probabilities are also compared with a series of measured breaking probability for various ε_w ($\varepsilon_w = 0.4$,0.5 and 0.6) , the results are shown in the Table 2. From the comparison, we find the highest correlation is from $\varepsilon_w = 0.5$ and also the slope is much closer to 1 for $\varepsilon_w = 0.5$ than $\varepsilon_w = 0.4$ or $\varepsilon_w = 0.6$. Therefore, we apply this coefficient to breaking criteria during the following analysis. In Figure 5.5, we show the relation between breaking probability and wind speed. The breaking probability from Romeo shows significant scatter in contrast with Bravo and Yankee from SHOWEX and the results from BASE. Through further analysis (see below), the scatter is caused by the complex sea states, not from the breaking criteria itself.

Similar comparisons between the modeled and measured breaking probabilities using geometric breaking criterion with $\varepsilon_w = 0.5$ are shown in Figure 5.6. They show lower correlations compared with the results from the kinematic breaking criterion for each buoy. Using the results from Katsaros and Atakturk (1992), the kinematic breaking criterion seem to be more suitable for field measurement than the geometric breaking criterion when apply to data. The reason is probably because the surface current and upper ocean shear may change the local geometry of wave slope. We will address this problem in the next section.

	$\varepsilon_w = 0.4$	$\varepsilon_w = 0.5$	$\varepsilon_w = 0.6$
Bravo (SHOWEX)	$\gamma_c = 0.28$	$\gamma_c = 0.64$	$\gamma_c = 0.29$
	$\chi = 0.21$	$\chi = 0.81$	$\chi = 3.11$
Yankee (SHOWEX)	$\gamma_c = 0.34$	$\gamma_c = 0.76$	$\gamma_c = 0.35$
	$\chi = 0.18$	$\chi = 0.88$	$\chi = 3.45$
Romeo (SHOWEX)	$\gamma_c = 0.11$	$\gamma_c = 0.37$	$\gamma_c = 0.09$
	$\chi = 0.25$	$\chi = 1.09$	$\chi = 2.78$
BASE	$\gamma_c = 0.30$	$\gamma_c = 0.78$	$\gamma_c = 0.33$
	$\chi = 0.31$	$\chi = 1.21$	$\chi = 4.32$

Table 2: The correlation coefficient γ_c and between the breaking model from Katsaros and Atakturk (1992) and breaking probability by different threshold value $\varepsilon_w = 0.4, 0.5, 0.6$ for four ASIS buoy wave data by kinematic breaking criteria. χ is the slope of the linear regression behavior of the model and the field data.

Banner et al. (2000) and Babanin et al. (2001) estimated the breaking probability (b_T) for dominant waves using data from several field experiments. Based on their approach, analysis of their data revealed that the probability of dominant wave breaking is strongly correlated with the significant wave steepness ($\beta = \frac{H_s k_P}{2}$ where k_p is the wavelength at peak frequency) for the broad range of wave conditions investigated. Of particular interest is a threshold of this parameter below which negligible dominant wave breaking occurs. Beyond the threshold, a near-quadratic

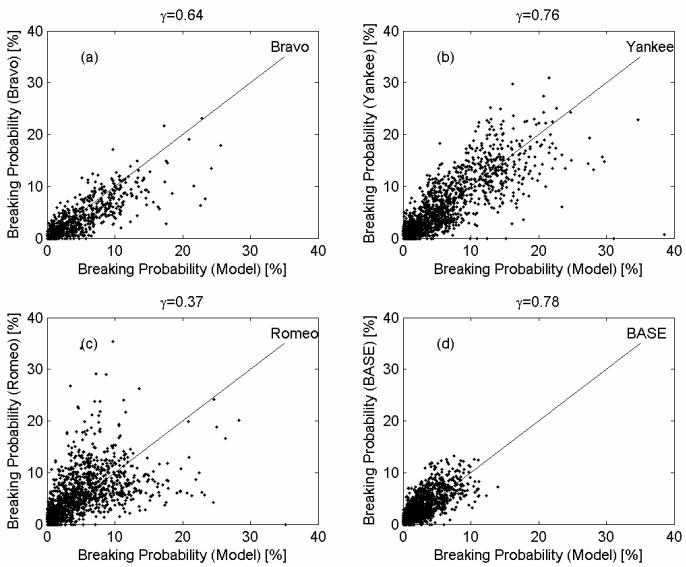

Figure 5.5. Modeled breaking probability from Katsaros and Atakturk (1992) versus observed breaking probability using kinematic breaking criterion. Data shown are from (a) Bravo, (b)Yankee, (c) Romeo in SHOWEX experiment. (d) is the data from BASE experiment. The titles indicate the correlation coefficient.

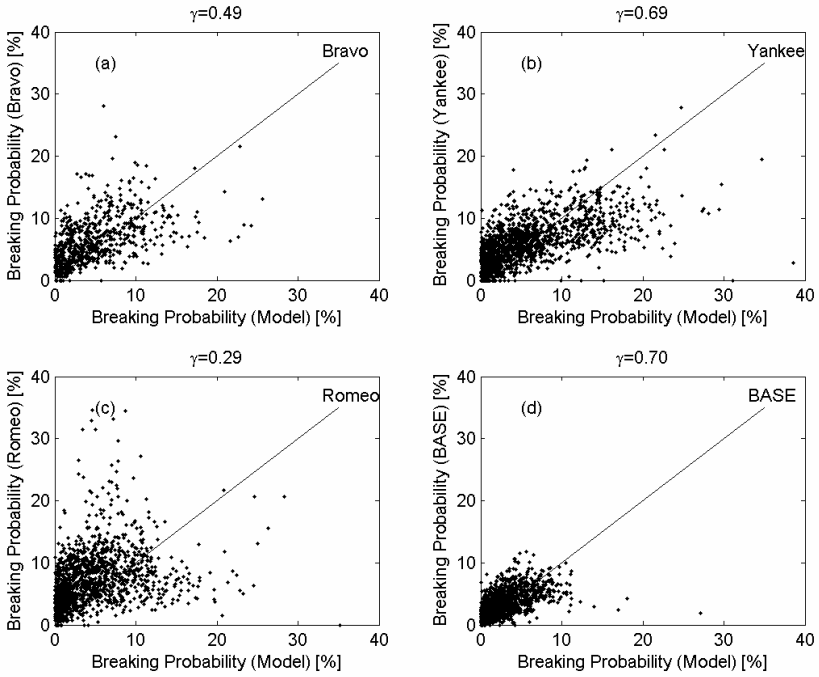

Figure 5.6. Modeled breaking probability from Katsaros and Atakturk (1992) versus Observed breaking probability using dynamic breaking criterion. Data shown are from (a) Bravo, (b)Yankee, (c) Romeo in SHOWEX experiment. (d) BASE experiment. The titles indicate the correlation coefficient.

dependence of the breaking probability on the significant wave steepness was observed. Furthermore, the inclusion of parameters representing the secondary influence of inverse wave age ($\upsilon = U_{10} f_p / g$) and background current shear ($\Delta = \frac{u_s}{u_0} = \frac{0.01 U_{10}}{\beta c_p}$ where u_s is the estimated wind-induced current at surface $u_s \sim 0.01 U_{10}$; u_0 is the maximum orbital velocity of a linear surface gravity wave with amplitude equal the significant wave height) improve the correlation marginally from 0.75 to 0.79 compared with the significant wave steepness. We expect the linear fits from Banner et al. (2000) and Babanin et al. (2001) to apply to our results too.

In Figure 5.7, all the pure wind sea data from BASE and SHOWEX are used to test the results from Banner et al. (2000) and Babanin et al. (2001), here the exclusion of swell data is in order to avoid the error associated with the double-peak wave spectra. The comparisons indicate that the breaking probability for dominant waves using kinematic breaking criterion agrees well with results from Banner et al. (2000) and Babanin et al. (2001). The correlation between our data and the regression relation from Banner et al. (2000) is 0.75 and 0.79 for the modified wave steepness and composite parameter respectively. These compare with coefficient of 0.78 and 0.81 found in the original Banner et al. (2000) and Babanin et al. (2001) data. Although they draw the conclusions that the mean wind speed is not the primary factor for the breaking of dominant waves, Our analysis cannot offer further support of this. In fact, the modified wave steepness, the inverse wave age, the wind-induced current and the maximum orbital velocity may be dependent on the mean wind speed at least for pure wind sea. The following analyses will still assume mean wind speed is the primary factor for dominant wave breaking; the

scatter under this relation may also be correlated to other parameters such as upper ocean shear.

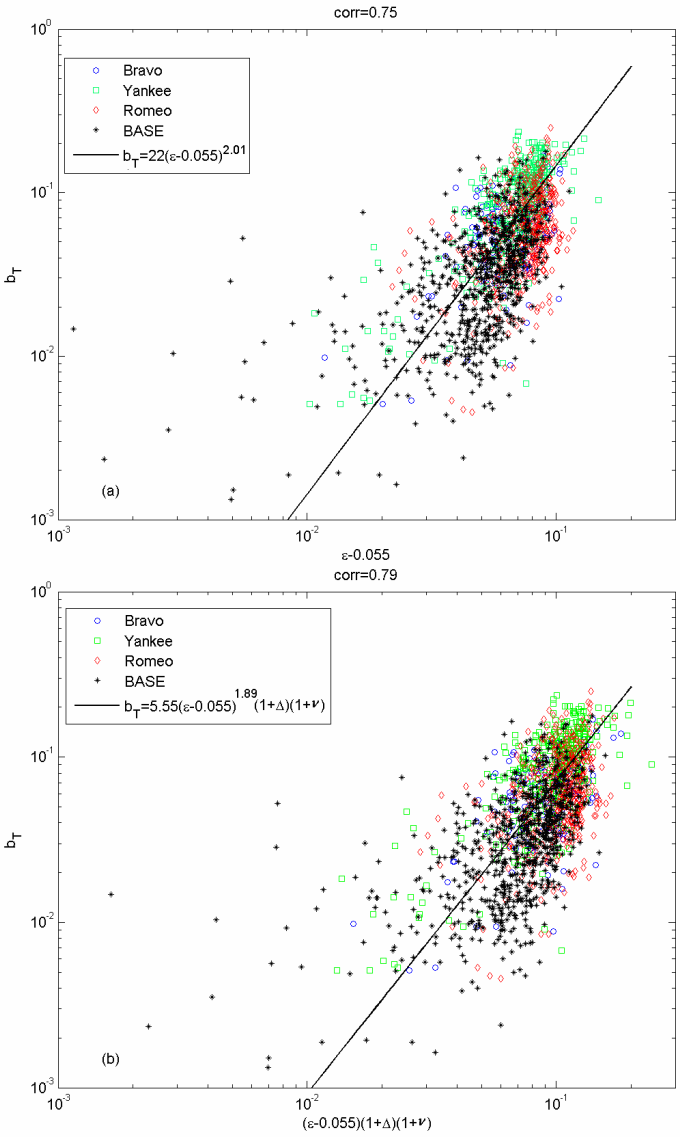

Figure 5.7. (a). Composite log-log plot of the observed dominant wave breaking probability b_T vs the modified dominant wave steepness (ε -0.055). The offset level of 0.055 is the mean peak steepness threshold below which negligible breaking was observed. The symbols shows the pure wind sea data from Bravo, Yankee and Romeo in the SHOWEX experiment; and ASIS buoy during BASE experiment. The title shows the correlation coefficient based on the linear best fit (the black line) in the log-log domain from Banner et al. (1999). (b). same as panel (a) but plotted against the composite parameter ($(\varepsilon - 0.055)(1+\Delta)(1+\gamma)$. Δ is background current shear; γ is inverse wave age. See text for details.

In Figure 5.8, the breaking probability determined from the kinematic breaking criterion using ASIS data is presented as a function of U_{10N}. The data show a clear increasing tendency of breaking probability with U_{10N}. Similar correlations have been found in several previous articles (Mitsuyasu, 1985; Melville and Rapp, 1985; Lionello et al., 1998).

From the Figures, the breaking probability is zero if U_{10N} is around less than 5 m/s. Zakharov (1992) calculated the threshold for the onset of breaking to be 6 m/s, which is in excellent accordance with data (Boundur and Sharkov, 1982; Banner et al., 1989). Our results support their theoretical and experimental analysis about the threshold wind speed to generate the wave breaking. The good agreement also enhances the reliability of the breaking criteria used here.

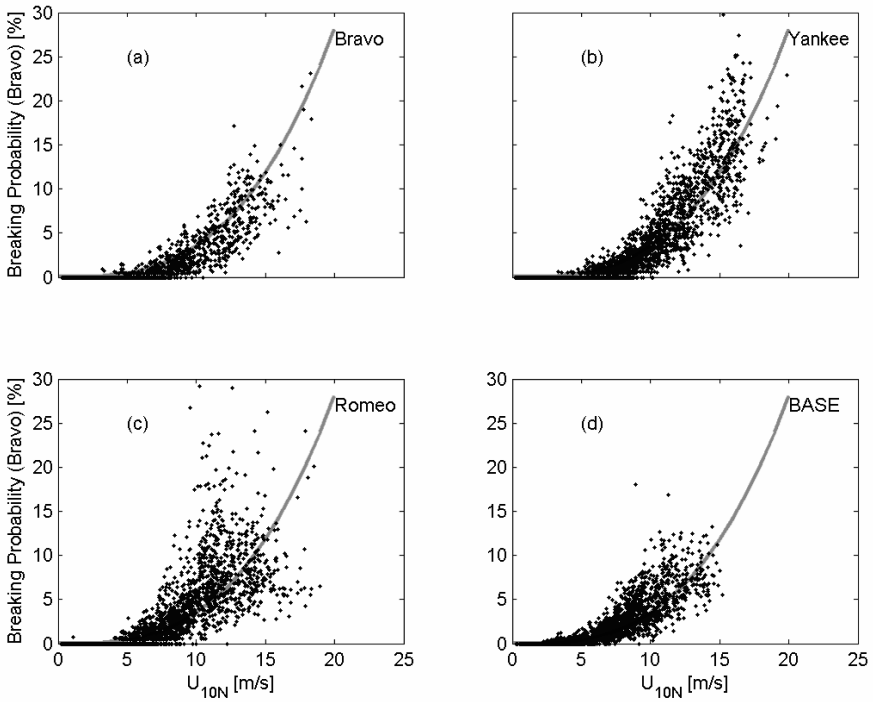

Figure 5.8. The breaking probability for dominant waves by kinematic breaking criterion as a function of mean wind speed data from (a) Bravo, (b)Yankee, (c) Romeo in SHOWEX experiment. (d) is the data from BASE experiment. The line in each panel is the relation $P = 0.0035 \times U^3{}_{10N}$.

Boundur and Sharkov (1982) subdivided the whitecap coverage W into two parts: (1) breaking crest (W_c) (2) residual foam (W_f) which is left by breaking crests. For the active breaking crests, they found

$W_c = 0$ $\qquad U_{10} < 5m/s$

$W_c = 0.015 \times [1 + 2.2 \times 10^{-2} (U_{10} - 5)^3]$ $\qquad U_{10} \geq 5m/s$

If we assume $W_a = aP$ (a is a coefficient of wave breaking scale) then Boundur and Sharkov (1982)'s results show an very good accordance with ours: (1) the threshold wind speed for wave breaking is about 5 m/s (2) the power law for the correlation between P and U_{10N} for $U_{10} \geq 5m/s$ is $P_k \sim U_{10N}^3$.

5.3 Breaking Enhancement

The scatter of breaking probability versus wind speed shows different characteristics under various conditions. For Bravo and Yankee, the wind forcing has the first order effect on the breaking of dominant waves. The correlation coefficients are 0.64 and 0.76 for the two buoys. The breaking probability still increases with U_{10N} for Romeo, but the scatter is much higher than for Bravo, Yankee and the buoy from BASE (Figure 5.5). Since Romeo did not report any instrument problem which could have affected the detection of wave breaking, we need extend our attention to other factors which may influence the onset of breaking of dominant waves. The factors include wave

development and upper ocean shear. In Figure 5.9, we again show the breaking probability ± 3 standard errors around the best fit line. In Figure 5.9, above the +3 standard error curve are enhanced breaking cases; those cases lower than the -3 line are suppressed breaking cases. The scatter points at low wind speed are insignificant and very possibly related to the noise of the detection method. Therefore, we focus on the data with $U_{10N} > 10 m/s$. As discussed earlier, wave breaking probability has been shown to have the primary dependence on the wind speed. However previous research has shown that there is always significant scatter between breaking probability and mean wind speed. Even the models of Katsaros and Atakturk (1992), Banner et al. (2000) or Babanin et al. (2001) which include second order parameters show high scatter.

An interesting question is why the enhanced breaking cases are found mainly at Romeo, with very few enhanced breaking cases seen at Bravo or Yankee. The appreciable difference among the three buoys is likely related to the differing sea states associated with the buoy locations. By studying the difference in the breaking probability at the three buoys, we can further understand the effect of sea state on the breaking of dominant waves.

Figure 5.10 shows the histogram of enhanced breaking cases for three buoys. The enhanced breaking cases take place mainly with two wind directions. When the wind is off shore, wave breaking enhancement is mainly due to the interaction of young wind sea waves (short fetch) with on-shore swell. Enhanced breaking also occurs during some along-shore wind events. In this direction, the wave fetch is long, and wind waves at all three buoys were fully developed. In the following, we will study the reasons for enhanced breaking for these cases.

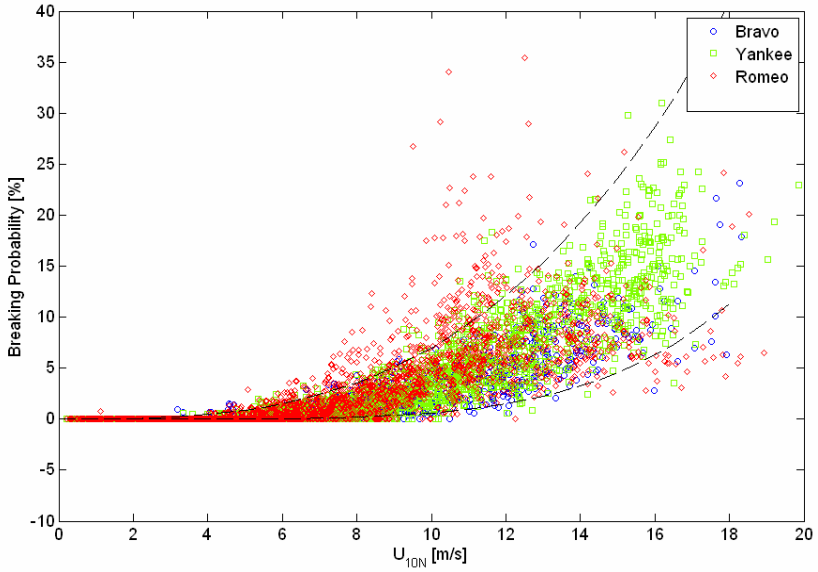

Figure 5.9. Breaking probability as a function of mean wind speed. The symbols represent the data from ASIS buoys in SHOWEX experiment. The dash lines show the ± 3 standard errors for the three buoys data. The points above the upper line indicate the breaking enhanced cases, and those below the lower line show the breaking suppressed cases.

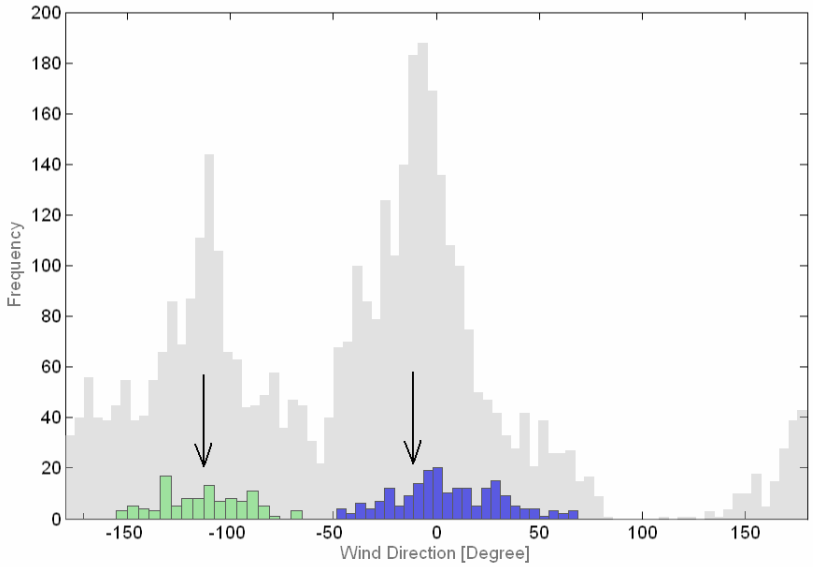

Figure 5.10. Wind direction distributions of the enhanced breaking cases in Figure 5.9. The gray shows the wind direction distributions for all cases with $U_{10} > 6m/s$. The green bars represent off-shore winds; the blue bars indicate along-shore wind (from north to south). The two arrows point to the direction normal to the coast line (left) and parallel to the coast line.

Figure 5.11 shows the time series of salinity measured at 5m depth at each buoy. Time periods with enhanced breaking are identified on the plot. Note that breaking is often

enhanced when the local salinity is decreasing. We focus on four time periods A, B, C and D, when enhanced breaking is particularly clear. Figure 5.12 indicates the detailed salinity information at Yankee and Romeo for the four periods, along with the averaged OSCR current maps for the four periods. During the periods, the wind generally blew southward along the coastline, with a strong current forced by the wind in the along-shore direction. Consistent with the sudden salinity decrease for these time periods, and location of Chesapeake Bay to the north of the experiment site, we can infer that wind forces the fresh water from Chesapeake Bay to the experiment site. The drop in salinity at the buoys is due to the strong buoyancy current intruding into the experiment site. However there is no evidence that a salinity change itself can cause the enhanced breaking. There must be another reason for that.

Figure 5.13b and 5.13c present daily temperature and salinity profiles measured at the end of the Duck pier. The data indicate the Middle Atlantic Bight Shelf water (with 32-34 psi practical salinity) mixing with a significant percentage of fresher and colder surface water from the north during events A and B. These cool lower salinity water plumes are associated with the southward winds. Figure 5.12 (A2 and B2) show the current vector maps from OSCR radar at the experiment site during A and B. At these times, we observe strong southward current ($U_s \sim 0.5 m/s$) from Chesapeake Bay. The events are buoyancy current (Rennie et al., 1999; Haus et al. 2003), which are reported to occur every 3 to 8 days, with the timing related to wind patterns. The southward winds may narrow and deepen the water plume, whereas upwelling winds cause it to be thin and spread offshore.

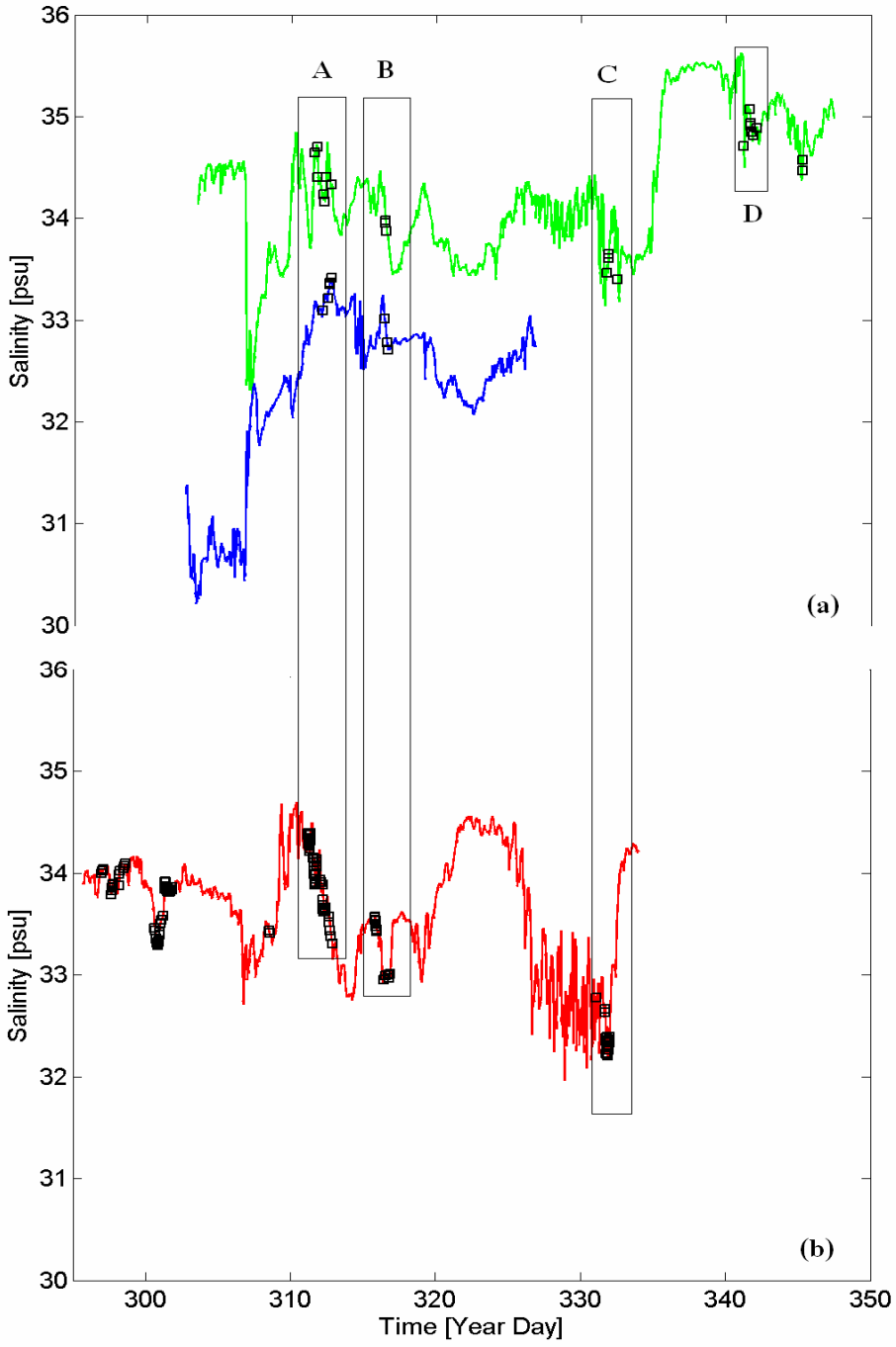

Figure 5.11. The time series of salinity measured at three buoys. The blue one in panel (a) is for Bravo; the green one in panel (a) is for Yankee. The red one in panel (b) is for Romeo. The black squares show the cases of breaking enhanced cases with wind along shore. (A), (B),(C) and (D) are four periods with frequent breaking enhanced cases.

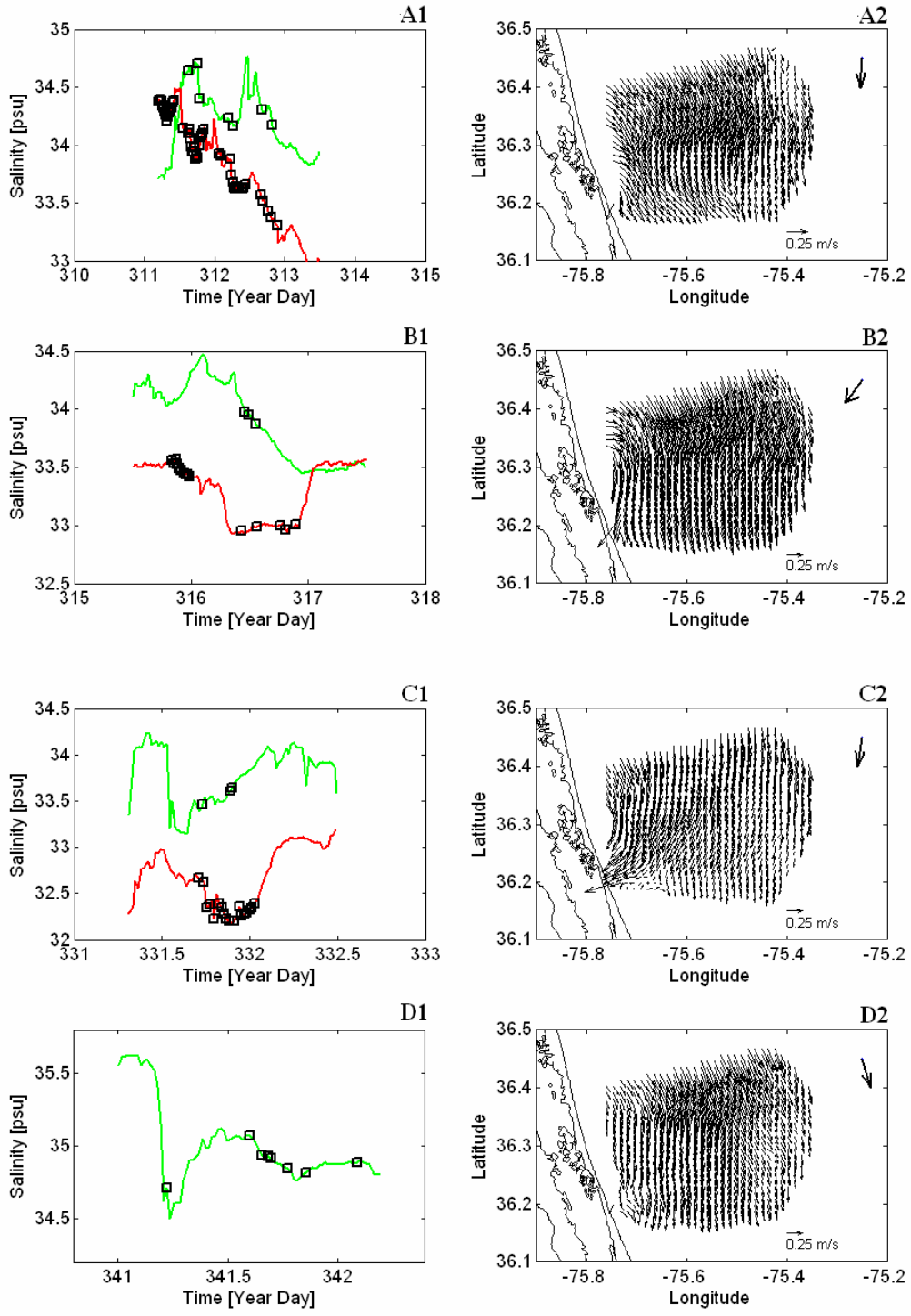

Figure 5.12. A1-D1: Salinity conditions as noted in Figure 5.11 at Yankee (green) and Romeo (red) with breaking enhanced cases for periods (A),(B),(C) and (D) denoted by square. A2-D2 are current maps corresponding to the periods A-D. The arrow at the top right indicate the wind direction.

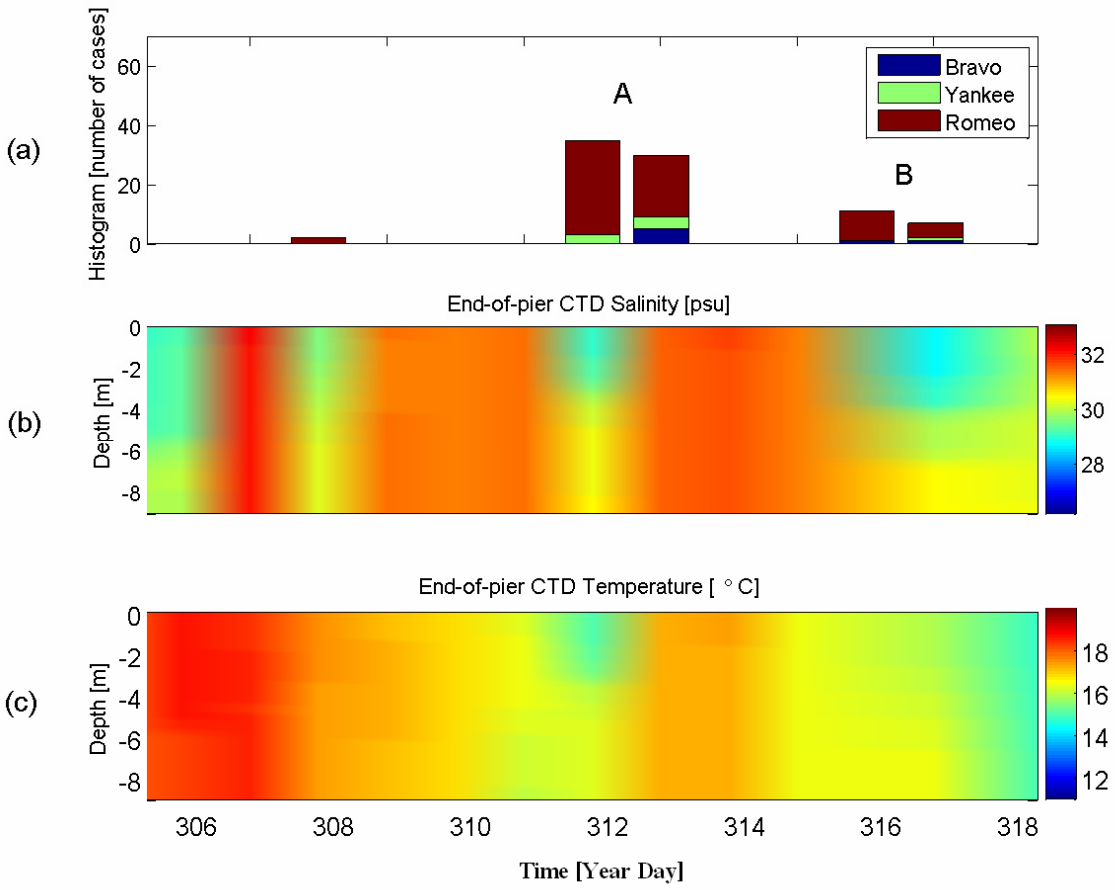

Figure 5.13. Time series of (a) histograms of breaking enhancement cases for three ASIS buoys in SHOWEX, (b) salinity profiles from end-of-pier CTD ,(c) SST profiles from end-of-pier CTD, (d) 5-meter-depth salinity at Yankee and Romeo, (e) 5-meter-depth SST at Yankee and Romeo. (f) and (g) are the current vector maps from OSCR radar for event A and B in panel (a).

We focus on why these low salinity, cool and southward flows can affect the dominant wave breaking. The southward along coast buoyancy current causes stratification in the near-surface of the ocean (Rennie et al., 1999; Haus et al. 2003). The surface water, drifted by wind, has the maximum speed. The sea water at some depth, mixing with deepwater, may have the minimum amplitude (Lentz and Largier, 2006). The density difference between the near surface and deeper ocean stabilize the near surface, and reduces the efficiency of mixing. Although we don't have detailed current profile

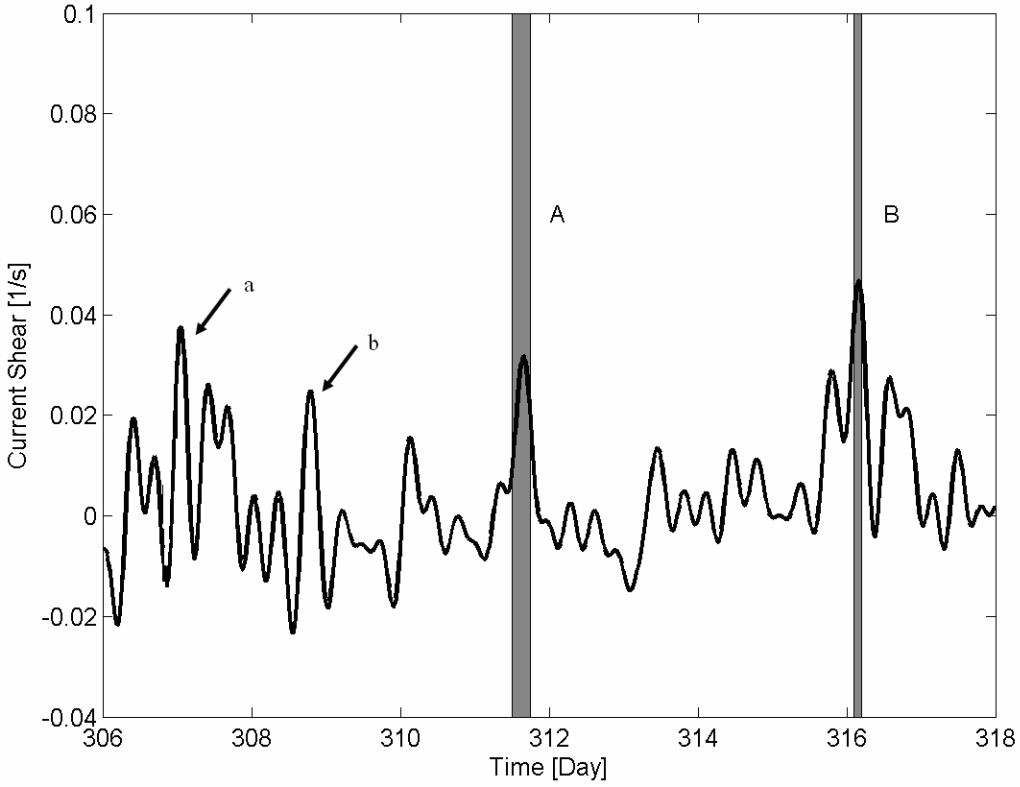

Figure 5.14. Current shear at the location of Yankee during SHOWEX experiment. The results are calculated by the current data from OSCR radar at the sea surface and current meter data at 5 meter depth. The original current data are processed by a low frequency filter to remove the fluctuations of more than 0.2 day. A and B are the periods during which breaking enhancement cases took place. (a) and (b) are two cases with strong vertical current shear without breaking enhancement.

measurements, the amplitudes of surface current (~1 m depth) from OSCR and the current meter at 5 m depth on ASIS show that the near-surface shear is high. Figure 5.14 shows that enhanced breaking events A and B are associated with the strong upper level shear conditions at the location of Yankee.

From Graber et al. (1996), the Ekman Drift Current is the cause for the upper ocean shear under wind stress. The expected vertical shear from 1m to 5m due to Ekman Drift is about 0.02 s^{-1} for $U_{10N} = 10m/s$ and 0.03 s^{-1} for $U_{10N} = 15m/s$. For events A ($U_{10N} \sim 10m/s$) and event B ($U_{10N} \sim 15m/s$), the measured upper ocean shear at

Yankee was almost double that caused Ekman Drift Current. Also during event A and B, the energy-containing waves propagated in the current direction, so the strong vertical shear can work on the dominant waves resulting in significantly enhanced breaking. Events (a) and (b) are also the periods of strong vertical current shear (Fig. 5.14), but the analysis does not indicate breaking enhancement during those times. For event (a), the wind was quickly turning (turning 100° clockwise in 4 hours), so the wind forcing on the dominant waves was reduced suddenly. Also the wind direction is perpendicular to the dominant current direction, so strong vertical current shear has little effect on the breaking of dominant waves. For event (b) the wind speed $U_{10N} \sim 3m/s$. No matter how strong the current shear, wave breaking does not occur at these light winds.

During SHOWEX, the upper ocean current profile was not measured, so our analysis here is not precise enough to separate the wind drift shear from total upper ocean shear. However, the experimental data support the hypothesis that upper ocean vertical shear enhances wave breaking. This was found previously by both theory and laboratory experiments, but has never been observed in field experiments. Banner and Phillips (1974) and Phillips and Banner (1974) first discussed the effect of such a thin shear layer and illustrated how in theory it greatly increased the likelihood of wave breaking. Teles da Silva and Peregrine (1988) using numerical models, showed that a background linear current may increase wave breaking by their numerical model results. The experimental results by Millinazo and Saffman (1990) partly proved the enhancement of microbreaking under wind driven vertical shear. However, the small waves are likely responding only to vertical shear very near the surface, not in the top 5 m. Our

observation of wave breaking enhancement associated with upper ocean shear presents new evidence to support the original theoretical work by Banner and Phillips.

Chapter 6

Conclusion

6.1 Current-Wave-Wind Interactions

Case studies of current-wave-wind interaction are presented for data from the SHOWEX experiment. During SHOWEX, near-surface currents were measured by HF radar; wind velocity, wind stress and high-resolution directional wave spectra are measured by instruments on ASIS buoys; sea surface roughness information over the domain was collected from the SeaWind radar on QuikSCAT. We focused on two cases. In the first, the ASIS buoys were located at the edge of a strong current gradient. In the second, ASIS buoys were in strong uniform current with the wind blowing across the current. From the analysis of these cases, we find the following conclusions:

(1) When a surface current is not aligning with the wind, there is a crosswind wind stress corresponds to the off-wind current component.

(2) Under the strong currents, the retrieved wind direction from QuikSCAT lies between the true wind direction and current direction, close to the wind stress direction. Neglecting the effect of current for the scatterometer radar causes errors in the retrieved wind direction by scatterometer

(3) The directional wave spectra from the ASIS buoys show that short gravity waves are steered towards the current direction when the wind is crossing a uniform current field; while the energy-contained waves remain in the same direction as the wind. Wind wave spectra from the SWAN model reproduced this steering. For the horizontally-sheared current case, long wind sea waves may be steered after passing the horizontal current gradient. Since wind stress near the surface corresponds to the waves in all frequency bands, this results in a steering of the wind stress away form horizontal direction.

(4) The relaxation time of surface waves can partly explain the observations of current-wave interaction, especially for the horizontally-sheared current case. This has been confirmed by recent numerical model results. However, the wave refraction under uniform current conflicts with the wave action conservation, and no existing theories or numerical model result can explain the high frequency wave refraction under uniform current completely.

Wave-current interaction remains as one of the least tested theories in the study of wave dynamics, and the extension to the current-wave-stress interaction has only recently been studied. The observational data presented in this in this dissertation provide first direct evidence that current can affect wind stress through waves, and waves play a key role in the current-wave-stress interaction. We do not have sufficient data to fully quantify the process; moreover the physics governing the interaction need to be further investigated. Over the global ocean, strong boundary currents can certainly change the wave field as discussed above. This change can cause errors in the presently used scatterometer model functions used for wind retrieval. Therefore, in order to monitor the

wind stress over current systems, a further understanding of the processes of wave-current-stress interaction is necessary.

6.2 Dominant Wave Breaking By ASIS Buoy

The Hilbert Transform is used to derive several local parameters needed for breaking wave detections. They indicated local parameters include local angular frequency, local surface velocity components and local phase speed from a single –point measurement of surface elevations. This method on the basis of the Hilbert Transform was successfully applied to several laboratory measurements of breaking waves with simultaneous visual observation or other methods to detect breaking waves. We applied the same technique to the surface elevation data from ASIS buoys during two field experiments. ASIS buoys, unlike other buoys that measure surface elevation by surface following, uses 5~8 wave wires to collect high resolution sea surface elevations. The precision of the data is high enough to use modified a Hilbert Transform technique to calculate the local wave properties. We apply two breaking criteria: a breaking kinematic criterion ($\frac{u(t)}{c(t)} \geq \varepsilon_w$) and a breaking geometric criterion ($\frac{1}{c(t)}\frac{\partial \zeta(t)}{\partial t} > \varepsilon_w \tan 30.37°$) developed in previous laboratory applications. Accounting for the sampling rate in the field experiment to the laboratory, we find $\varepsilon_w = 0.5$, provided the best agreement in breaking probability coupled with results from previous research

The breaking probability has a very clear threshold value for wind speed

at $U_{10N} \approx 5m/s$. This wind speed threshold not only confirms the theory investigation by (Zakharov, 1992), it is also very close to several field observations. Above the threshold value, the breaking probability versus wind speed has a power relation as $P \sim U_{10N}^3$. Although this result is different from laboratory conclusions, it is the same as the power relation between the active whitecap coverage and wind speed by assuming the active whitecap area has a linear relation with the number of dominant breaking waves.

At times, the breaking probability versus wind speed shows large deviation from the cubic relation with wind speed, highlighting that the unknown factors are also important. In particular, vertical shear in the upper ocean was found to strongly enhance breaking during studied events.

Overall, our analysis results of breaking probability show agreement with previous research. On the basis of this, we believe Hilbert Transform can be applied to the field data to detect dominant wave breaking. Using this technique on ASIS buoy may provide a reliable low cost and long duration method to detect breaking waves compared with previous wave breaking detection. The results from this dissertation supplement the limited wave breaking data available to date, and increase our understanding of the effect of the wave breaking on the surface layer for both sides of air-sea interface.

References

Anctil, F., M.A. Donelan, W.M. Drennan and H.C. Graber, (1994), Eddy correlation measurements of air-sea fluxes from a Discus buoy. *J. Atmos. Oceanic Tech. 11*, 1144-1150.

Ardhuin F., and T.H.C. Herbers (2005), Numerical and physical diffusion: Can wave prediction models resolve directional spread? *J. Atmos. Oceanic Technol.*, 22**,** 883–892.

Ardhuin, F., T.H.C. Herbers, G.P. van Vledder, K.P. Watts, R. Jensen, and H.C. Graber (2007), Swell and slanting-fetch effects on wind wave growth , *J. Phys. Oceanogr.*, 37, 908–931.

Alpers,W., and I. Hennings (1984), A theory of the imaging mechanism of underwater bottom topography by real and synthetic aperture radar, *J. Geophys. Res.*, 89(C6), 10,529-10,546.

Babanin, A.V., I.R Young, and M.L. Banner (2001), Breaking probabilities for dominant surface waves. on water of finite constant depth. *J. Geophys. Res.,* 106(C6) , 11659–11676.

Banner, M.L. and O.M. Phillips (1974), On the Incipient Breaking of Small Scale Waves, *J. Fluid Mech.,* Vol. 65, 1974, pp. 647–656.

Banner,M.L. and Melville,W.K. (1976), On the separation of air flow over water waves, *J. Fluid Mech.,* 77, 825-842.

Banner, M.L., Jones, I.S.F., Trinder, J.C., (1989), "Wavenumber spectra of short gravity waves", *J. of Fluid Mech.*, vol. 198, pp. 321-344.

Banner, M.L., (1990), The influence of wave breaking on the surface pressure distribution in. wind-wave interactions. *J. of Fluid Mech*., 211, 463-495.

Banner M. L., A. V. Babanin, and I. R. Young, (2000), Breaking probability for dominant waves on the sea surface. *J. Phys. Oceanogr.*, 30, 3145–3160.

Bentamy, A., P. Queffeulou, Y. Quilfen and K. Katsaros (1999), Ocean surface wind fields estimated from satellite active and passive microwave instruments. *IEEE Trans Geosci. Remote Sens. 37*, 2469-2486

Bondur, V.G., and E.A. Sharkov, (1982), Statistical properties of whitecaps on a rough sea, *Oceanology,* 1, 274-279.

Booij, N., R. C. Ris, and L. H. Holthuijsen, (1999), A third-generation wave model for coastal regions, 1, Model description and validation, *J. Geophys. Res*., 211, 463-495.

Brethertom, F. P. and C. J. R. Garrett (1968), Wavetrains in inhomogeneous moving media, *Proc. Roy. Soc.* (A) *302*, 529–554.

Businger, J.A., Wyngaard, J.C., Izumi, Y. and Bradley, E.F., (1971), Flux-profile relationships in the atmospheric surface layer, *J. Atmos. Sci,* **28**, 181-189.

Busch, N. E., (1977), Fluxes in the surface boundary layer over the sea. *Modeling and Prediction of the Upper Layers of the Ocean*, E.B. Kraus, Ed., Pergamon Press, PP 72-91.

Capon, J., (1969), High-resolution frequency-wavenumber spectrum analysis. *Proc. IEEE* 57, 1408-1418.

Chang, K. A., and P. L. F. Liu, (1998), Velocity, acceleration and vorticity under a breaking wave, *Phys. Fluids*, *10*(1), 327–329.

Chelton, D.B., M.G. Schlax, M.H. Freilich, R.F. Milliff, (2003), Satellite Measurements Reveal Persistent Small-Scale Features in Ocean Winds, *Science* DOI: 10.1126/science.1091901

Chen, S. S., J. F. Price, W. Zhao, M. A. Donelan, and E. J. Walsh, (2007), The CBLAST-Hurricane Program and the next-generation fully coupled atmosphere-wave-ocean models for hurricane research and prediction. *Bull. Amer. Meteor. Soc*, 88, 311-317.

Cornillon, P., and Park, K.-A. (2001), Warm core ring velocities inferred from NSCAT, *Geophys. Res. Lett. 28*, 575-578.

Davidson, K.L. and A.J. Frank, (1973), Wave-Related Fluctuations in the Airflow Above Natural Waves. *J. Phys. Oceanogr.* 3, 102-119.

Dickinson, S., K. A. Kelly, M. J. Caruso, and M.J. McPhaden, (2001), A note on comparisons between the TAO and NASA scatterometer wind vectors, *J. Oceanic Atmos. Techno., 18*,799-806.

Dobson, F. and B. Toulany, in Directional Ocean Wave Spectra, (1991)*, Johns Hopkins University Press*, Baltimore, 22–33

Donelan M. A., M. S. Longuet-Higgins, and J. S. Turner, (1972), Whitecaps. *Nature*, 239, 449–451.

Donelan, M.A., J. Hamilton and W.H. Hui (1985), Directional Spectra of wind generated waves. *Phil. Trans. R. Soc. London A315*, pp. 509-562.

Donelan, M.A., Air-Sea Interaction, (1990), *The Sea: Ocean Engineering Science 9, (B. LeMéhauté and D. Hanes, Eds.), John Wiley and Sons, Inc.*, New York, pp. 239-292.

Donelan, M. A., B. K. Haus, N. Reul, W. J. Plant, M. Stiassnie, H. C. Graber, O. B. Brown, and E. S. Saltzman, (2004), On the limiting aerodynamic roughness of the ocean in very strong winds, *Geophys. Res. Lett.,* 31, L18306.

Drennan, W.M., K.K. Kahma, E.A. Terray, M.A. Donelan and S.A. Kitaigorodskii, (1992) Observations of the enhancement of kinetic energy dissipation beneath breaking wind waves. In: *Breaking waves*, Banner, M.L and R.H.J. Grimshaw, Eds., Springer, 95-101.

Drennan, W.M., M.A. Donelan, N. Madsen, K.B. Katsaros, E.A. Terray and C.N. Flagg, (1994), Directional wave spectra from a Swath ship at sea. *J. Atmos. Oceanic Tech. 11*, 1109-1116.

Drennan, W.M., H.C. Graber, D. Hauser, and C. Quentin (2003), On the wave age dependence of wind stress over pure wind seas, *J. Geophys. Res., 108(C3),* 8062.

Drennan, W.M. and L. K. Shay., (2006) On the variability of the fluxes of momentum and sensible heat, *Bound. Layer Meteor., 119(1)*, 81,107.

Dyer, A.J., (1974), A review of the flux-profile relationships, *Boundary-Layer Meteorol.*, 42, 9-17.

Dupuis, H., P.K. Taylor, A. Weill and K. Katsaros, 1997: Inertial dissipation method applied to derive turbulent fluxes over the ocean during the Surface of the Ocean, Fluxes and Interactions with the Atmosphere/ Atlantic Stratocumulus Transition Experiment (SOFIA/ASTEX) and Structure des Echanges Mer-Atmosphere, Proprietes des Heterogeneites Oceaniques: Recherche Experimentale (SEMAPHORE) experiments with low to moderate wind speeds. *J. Geophys. Res.* 102, 21115-21129.

Edson, J.B., and C.W. Fairall, (1998), Similarity relationships in the marine atmospheric surface layer for terms in the TKE and scalar variance budgets. *J. Atmos. Sci.* 55, 2311-2328.

Geernaert, G. L., K.B. Katsaros and K. Richter, (1986), Variations of the drag coefficient and its dependence on sea state. *J. Geophys. Res*. 91, 7667-7679.

Geernaert, G. L., (1988) Measurements of the angle between the wind vector and stress vector in the surface layer over the North Sea. *J. Geophys. Res. 93*, 8215-8220.

Gerling, T. W. (1992), Partitioning sequences and arrays of directional ocean wave spectra into component wave systems, *J. Atmos. Oceanic Technol., 9*, 444-458.

Geernaert, G. L., F. Hansen, M. Courtney and T. Herbers, (1993), Directional attributes of the ocean surface wind stress vector. *J. Geophys. Res. 98*, 16571-16582.

Graber, H. C., B. K. Haus, L. K. Shay, and R. D. Chapman, (1997), HF radar comparisons with moored estimates of current speed and direction: Expected differences and implications, *J. Geophys. Res.*, *102*, 18,749–18,766

Graber, H. C., E. A. Terray, M. A. Donelan, W.M. Drennan, J. Van Leer and D.B. Peters, (2000), ASIS -- A new air-sea interaction spar buoy: design and performance at sea. *J. Atmos. Oceanic Tech. 17*, 708-720.

Grachev, A. A., C. W. Fairall, J. E. Hare, J. B. Edson, and S.D. Miller, (2003), Wind stress vector over ocean waves. *J. Phys. Oceanogr., 33*, 2408-2429.

Griffin, O. M., R. D. Peltzer, and H. T. Wong, Kinematic and dynamic evolution of deep water breaking waves, (1996), *J. Geophys. Res.*, *101*(C7), 16,515–16,531.

Hare, J.E., T. Hara, J.B. Edson and J.M. Wilczak, (1997), A similarity analysis of the structure of airflow over surface waves. *J. Phys. Oceanogr.* 27, 1018-1037.

Haus, B. K., H. C. Graber, L. K. Shay and T.M. Cook, (2004), Alongshelf variability of a coastal buoyancy current during the relaxation of downwelling favorable winds. *J. Coastal Res.*, *19*, 409-420.

Haus B. K., Surface current effects on the fetch-limited growth of wave energy (2007), *J. Geophys. Res*., 112, C03003, doi:10.1029/2006JC003924.

Hayes,W. D., *Proceedings of the Royal Society of London. Series A, Mathematical and Physical Sciences*, Vol. 320, No. 1541. (Dec. 15, 1970), 187-208.

Hellerman S., and M. Rosenstein (1983), Normal monthly wind stress over the world ocean with error estimates, *J. Phys. Oceanogr.*, 13, 1093-1104.

Högström, U.: (1996), 'Review of some basic characteristics of the atmospherics of the atmospheric surface layer', *Boundary-Layer Meteorol.,* **78,** 215-246.

Holthuijsen, L. H., T. H. Herbers, (1985), Statistics of breaking waves observed as whitecaps in the open sea, *J. Phys. Oceanogr., 16* 290-297.

Huang et al., N.E. Huang, D.T. Chen, C.C. Tung and J.R. Smith, (1972), Interactions between steady non-uniform currents and gravity waves with application for current instruments, *J. Phys. Oceanogr.* 2 pp. 420–431

Hwang, P. A., D. Xu, J. Wu, (1989), Breaking of wind-generated waves: Measurements and characteristics, *J. Fluid Mech., 202* 177-200.

Janssen, P.A., (1989), Wave-Induced Stress and the Drag of Air Flow over Sea Waves. *J. Phys. Oceanogr.*, 19, 745–754.

Kawai, S., (1981), Visualization of airflow separation over wind wave crests under moderate wind. *Boundary Layer Met.*, 21, 93-104.

Kawai, S., (1981), Structure of the air flow over wind wave crests revealed by flow visualization techniques. *Boundary Layer Met.*, 23, 503-521.

Katsaros, K.B. and S.S. Ataktürk, (1992), Dependence of Wave Breaking Statistics on Wind Stress and Wave Development. In *Breaking Waves*, M. L. Banner and R.H.J. Grimshaw, eds., IUTAM Symposium Sydney, Australia , 119-132.

Kelly, K.A., S. Dickinson, M.J. McPhaden, G.C. Johnson, (2001), Ocean currents evident in satellite wind data, *Geophys. Res. Lett.* 12, 2469-2472.

Kelly, K.A., S. Dickinson, and G.C. Johnson, (2005), Comparisons of scatterometer and TAO winds reveal time-varying surface currents for the tropical Pacific Ocean, *J. Atmos. and Ocean. Tech.*, 22, 735-745.

Kenyon, K. ,(1971), Wave refraction in ocean currents, *Deep Sea Res.*, *18*, 1023–1034.

Kitaigordskii,S.A., V.P. Krasitskii, and M.M. Zaslavskii, (1983), On Phillips' Theory of Equilibrium Range in the Spectra of Wind-Generated Gravity Waves, *J. of Phys. Oceanogr.,* **5**, 410-420

Kitaigorodskii, S. A., (1973), The Physics of Air–Sea Interactions. *Israel Program for Scientific Translation Jerusalem*, pp. 237.

Kitaigorodskii, S.A., Krasitskii, V.P., and Zaslavskii, M.M.,(1975), On Phillips' equilibrium range in the spectra of wind generated gravity waves, *J. Phys. Oceanogr*., 5, pp. 410-420.

Kudryavtsev, V., D. Hauser, G. Caudal, and B. Chapron, (2003), A semiempirical model of the normalized radar cross-section of the sea surface 1. Background model. *J. Geophys. Res.* 108 (C3), 8054-8074.

Kudryavtsev, V., D. Akimov, J. Johannessen, G. Caudal, and B. Chapron ,(2005), On radar imaging of current features: 1. Model and comparison with observation, *J. Geophys. Res. 110*, C07016

Large, W.G. and S. Pond, (1981), Open ocean momentum flux measurements in moderate to strong winds. *J. Phys. Oceanogr.* 11, 324-336.

Lafon, C., J. Piazzola, P. Forget, O. Lecalve et S. Despiau, 2004: Analysis of the variations of the whitecap fraction as measured in coastal zone during the FETCH experiment, *Boundary Layer Meteorology*., 111, 339-360

Lentz, S.J., Largier, J., (2006), The Influence of Wind Forcing on the Chesapeake Bay Buoyant Coastal Current. *J. Phys. Oceanography* 36(7): 1305-1334.

Lionello, O., P. Malguzzi, and A. Buzzi, (1998), Couping between the atmospheric circulation and ocean wave field: An idealized case. *J. Phys. Oceanogr.*, 28, 161-177.

Longuet-Higgins, M. S., On wave breaking and equilibrium spectrum of wind,(1969), *Proc. R. Soc. London, Ser. A*, *310*, 151–159, 1969.

Longuet-Higgins, M. S., M. J. H. Fox, (1977), Theory of the almost-highest wave: The inner solution, *J. Fluid Mech., 80* 721-741.

Longuet-Higgins, M. S., N. D. Smith, (1983), Measurement of breaking waves by a surface meter, *J. Geophys. Res., 88* 9823-9831.

Masson, D., (1996), A case study of wave-current interaction in a strong tidal current. *J. Phys. Oceanogr.* 26, 359-372.

Melville, W. K., (1983), Wave modulation and breakdown, *J. Fluid Mech.,* 128 489-506.

Melville, W. K. and Rapp R. J., (1985), Momentum flux in breaking waves. *Nature*, 317.

Melville W. K., (1996), The role of surface-wave breaking in air–sea interaction. *Annu. Rev. Fluid Mech.*, 26, 279–321

Miles, J. W., On the Generation of Surface Waves by Turbulent Shear Flows, (1960), *J. Fluid Mech. 7*, 469–478.

Millinazzo, F. A., and P. G. Saffman, (1990), Effect of surface shear stress layer on gravity and gravity–capillary waves of permanent form. *J. Fluid Mech.,* 216, 93–101.

Mitsuyasu, H. (1985), A note on the momentum transfer from wind to waves. *J. Geophys. Res.* 90 C2, 3343-3345.

Monahan, E. C., Oceanic whitecaps,(1971), *J. Phys. Oceanogr., 1* 139-144.

Monahan, E. C., and I., O' Muircheartaigh, (1980),Optimal power-low description of oceanic whitecap coverage dependent on wind speed, *J. Phys. Oceanogr., 10* 2094-2099.

Moon, I., I. Ginis, and T. Hara, B. Thomas, (2007), Physics-based parameterization of air-sea momentum flux at high wind speeds and its impact on hurricane intensity predictions. *Mon. Wea. Rev.* 135, 2869-2878.

Monin, A.S., and A.M. Obukhov, (1954), Basic laws of turbulent mixing in the ground layer of the atmosphere. *Akad. Nauk. SSSR Geofiz.Inst. Tr.* 151, 163-187.

Monin, A. S., and A. M. Yaglom, (1971) *Statistical Fluid Mechanics: Mechanisms of Turbulence.* Vol. 1. The MIT Press, 769-781

Norden E. Huang, Davidson T. Chen, Chi-Chao Tung, and James R. Smith, (1972),Interactions between Steady Won-Uniform Currents and Gravity Waves with Applications for Current Measurements, *J. of Phys. Oceanogr.,* Volume 2, Issue 4 420–431

Oh, S.H., Mizutani, N., Suh, K.-D., and Hashimoto, N. (2005), Experimental investigation of breaking criteria of deepwater wind waves under strong wind action. *Applied Ocean Research*, 27, 235-250.

Perlin, M., J. He, and L. P. Bernal, An experimental study of plunging breakers, *Phys. Fluids*, *8*(9), 2365–2374, 1996.

Phillips, O.M. (1957), On the generation of waves by turbulent wind. *J. Fluid Mech*. 2, 417-445.

Phillips, O.M., (1958), The equilibrium range in the spectrum of wind-generated waves. *J. Fluid Mech.,* 4, 426-434.

Phillips, O.M and Banner, M.L. , (1974), Wave breaking in the presence of wind drift and swell. *J. Fluid Mech.* 66: 625-640.

Pond, S., G. T. Phelps, J. E. Paquin, G. McBean, and R. W. Stewart, (1971), Measurements of the turbulent fluxes of momentum, moisture and sensible heat over the ocean. J. *Atmos. Sci.*, 28, 901-917.

Powell, M.D., P.J. Vickery, and T.A. Reinhold., (2003),Reduced drag coefficient for high wind speeds in tropical cyclones. *Nature*, 422:279-283

Pettersson, H., H.C. Graber, D. Hauser, C. Quentin, K.K. Kahma, W.M. Drennan, and M.A. Donelan, (2003), Directional wave measurements from three wave sensors during the FETCH experiment, *J. Geophys. Res., 108(C3)*, 8061.

Phillips, O. M., (1966), *The Dynamics of the Upper Ocean*, Cambridge University Press.

Polito, P., J. P. Ryan, W. t. Liu, and F. P. Chavez, (2001), Oceanic and Atmospheric Anomalies of Tropical instality Waves, *Geophys. Res. Lett., 28*, 2233-2236

Prandle, D., (1987), The fine-structure of nearshore tidal and residual circulation revealed by HF radar surface current measurements. *J. Phys. Oceanogr* 17, 231-245.

Qiao, H., and J. H. Duncan, Gentle spilling breakers, (2001), Crest flow-field evolution, *J. Fluid Mech.*, *439*, 57–85.

Rennie, S. E., J. L. Largier, S. J. Lentz, Observations of a pulsed buoyancy current downstream of Chesapeake Bay, *J. Geophys. Res., 104(C8)*, 18227-18280

Richardson, L. F. (1920), The supply of enery from and to atmospheric eddues. *Proc. Roy. Soc.* A97, 354-373

Richardson, P.L. and T.K. McKee (1984), Average seasonal variation of the Atlantic equatorial currents from historical ship drifts. *J. Phys. Oceanogr.*, **14**, 1226-1238.

Rieder, K.F., J. A. Smith and R. A. Weller, (1994), Observed directional characteristics of the wind, wind stress and surface waves on the open ocean. *J. Geophys. Res. 99*(C11), 22589-22596.

Shay, L. K., P. C. Zhang, H. C. Graber, and E. J. Walsh, (1996), Simulated surface wave current interactions during SWADE, *Global Atmos. Ocean Syst.*, *5*, 125–150.

Smedman, A.S., U. Högström, H. Bergström, A. Rutgersson, K.K. Kahma and H. Pettersson, 1999: A case study of air-sea interaction during swell conditions. *J. Geophys. Res*. 104 , 25833-25852.

Smith, S.D., (1980) Wind stress and heat flux over the ocean in gale force winds. *J. Phys. Oceanogr. 10*, 709-726.

She K., C. A. Greated, and W. J. Easson, (1997), Experimental study of three-dimensional breaking kinematics. *Appl. Ocean Res.*, 19, 329–343.

Sreenivasan, K., (1995), On the universality of the Kolmogorov constant. *Phys. Fluids,* 7, 2788-2784.

Stansell, P., and C. MacFarlane, Experimental investigation of wave breaking criteria based on wave phase speeds, *J. Phys. Oceanogr.*, *32*(5), 1269–1283, 2002.

Steven R. Long and Norden E. Huang, (1976), Observations of Wind-Generated Waves on Variable Current, *J. Phys. Oceanogr.* 6,962-968

Steward, (1974), The air-sea momentum exchange, *Boundary-Layer Meteorol.***,** 6**,**151-167.

Stewart, R. H., and J. W. Joy, (1974), HF radar measurement of surface current ,*Deep Sea Res.*, 21, 1039-1049.

Teles Da Silva, A. F., and D. H. Peregrine, (1988), Steep, steady surface waves on water of finite depth with constant vorticity. *J. Fluid Mech.,* 195, 281–302.

Terray, E.A., M.A. Donelan, Y.C. Agrawal, W.M. Drennan, K.K. Kahma, A.J. Williams III, P.A Hwang and S.A. Kitaigorodskii, (1996), Estimates of kinetic energy dissipation under breaking waves. *J. Phys. Ocean.* 26, 792-807.

Thorpe, S. A. and P. N. Humphries, Bubbles and breaking waves, *Nature, 283* 463-465 1980.

Toba, Y., H. Kunishi, K. Nishi, S. Kawai, Y. Shimada and N. Shibata, (1971), Study on air-sea boundary processes at the Shirahama Oceanigraphic Tower Station. Disaster Prevention Research Institute . *Kyoto University Annals*, 148, 519-531.

Toba, Y., M. Chaen, (1974), Quantitative expression of the breaking of wind waves on the sea surface, *Rec. Oceanogr. Works Jpn., 12* 1-11.

Tulin M. P., and J. Li, (1992), On the breaking of energetic waves. *Int. J. Offshore Polar Eng.*, 2, 46–53

Weisberg R. H., (1984), Seasonal adjustment in the equatorial Atlantic during 1983 as seen by surface moorings. *Geophys. Res. Lett. 11*, 733-735.

Wieringa, J., (1980), A revaluation of the Kansas mast influence on measurements of stress and cup anemometer overspeeding. *Bound. Layer Meteorol* 18, 411-430.

Weissmann, M. A., S. S. Atakturk, K. B. Katsaros, (1984),Detection of breaking evens in a wind-generated wave field, *J. Phys. Oceanogr., 14* 1608-1619.

Wentz, F.J., and D.K. Smith, (1999), A model function for the ocean-normalized radar cross section at 14 GHz derived from NSCAT observations, *J. Geophys. Res., 104*, 11499-11514.

Wu, J., (1975), Wind-induced drift currents. *J. Fluid Mech., 68*, 49-70.

Wu, J., (1979), Oceanic whitecaps and sea state, *J. Phys. Oceanogr., 9* 1064-1068.

Wyatt L. R., G. Liakhovetski, H. C. Graber, B. Haus (2005), Factors affecting the accuracy of SHOWEX HF radar wave measurements. *J. Atmos. Oceanic Technol*. 22,847-859

Wyngaard, J. C., (1981), The effects of probe-induced flow distortion on atmospheric turbulence measurements. J. Appl. Meteor., 20, 784-794.

Xu, D., P. A. Hwang, J. Wu, (1986), Breaking of wind-generated waves, *J. Phys. Oceanogr., 16* 2172-2178.

Zakhrov, V.E., (1992), Inverse and Direct Cascade in the Wind-Driven Surface Wave Turbulence and Wave Breaking. In *Breaking Waves*, M. L. Banner and R.H.J. Grim ' eds., IUTAM Symposium Sydney, Australia, 1991, 69-94.

Zemba, J., and C.A. Friehe, (1987), The marine atmospheric boundary layer jet in the Coastal Ocean Dynamics Experiment. *J. Geophys. Res., 92*, 1489-1496.